Multiscale Spectral Element - Boundary Integral Method for Linear and Nonlinear Nano Optical Computation

by

Jun Niu

Department of Electrical and Computer Engineering
Duke University

Date: ____________________

Approved:

____
Qing Huo Liu, Supervisor

____
William T. Joines

____
Jungsang Kim

____
Adrienne Stiff-Roberts

____
Loren W. Nolte

Dissertation submitted in partial fulfillment of the requirements for the degree of Doctor of Philosophy in the Department of Electrical and Computer Engineering in the Graduate School of Duke University
2017

Abstract

Multiscale Spectral Element - Boundary Integral Method for Linear and Nonlinear Nano Optical Computation

by

Jun Niu

Department of Electrical and Computer Engineering
Duke University

Date: ____________________
Approved:

____
Qing Huo Liu, Supervisor

____
William T. Joines

____
Jungsang Kim

____
Adrienne Stiff-Roberts

____
Loren W. Nolte

An abstract of a dissertation submitted in partial fulfillment of the requirements for the degree of Doctor of Philosophy in the Department of Electrical and Computer Engineering
in the Graduate School of Duke University
2017

Abstract

In this work, a hybrid mixed order numerical framework is proposed for multiscale linear/ nonlinear nano optical computation. Starting from the principle of the spectral element boundary integral (SEBI) method, the mixed-order SEBI solver with homogeneous Green's function is first developed for the nano-scale linear and nonlinear electromagnetic scattering analyses. The SEBI realizes the exact radiation boundary condition with a set of surface integral equations (SIE's), and discretize the whole computation domain with the fast convergent Gauss-Lobatto-Legendre (GLL) basis function. The Bloch periodic boundary condition is applied for efficient simulation of structures with periodicities in one or two directions.

For nonlinear optical simulation, full-wave solver is developed self-consistently by iteratively solving the vector Helmholtz equations at each harmonic frequency. To further address the multiscale scattering analysis in nano optics, a hybrid framework is developed by combing the SEBI solver with the dyadic periodic layered medium Green's function (PLMGF) and the domain decomposition method (DDM). Formulating the SIE's with the dyadic PLMGF, all unknowns in the background layered medium are pushed to the radiation boundaries. Thus, the whole planar layered background can be truncated from the computation domain. Considering its highly singular analytical properties, the PLMGF is carefully and systematically formulated under matrix representation. A feasible and effective technique is proposed for the on-interface PLMGF singularity extractions. By extracting the primary and sec-

ondary terms' singularities separately, all PLMGF-related SIE components can be efficiently evaluated. The DDM further reduces the memory cost for electrically large problems and enhances the framework's flexibility. Finally, a scattered field perfectly matched layer - surface integral equation (PML-SIE) radiation boundary condition is proposed to enable the non-periodic modeling. With the hybrid radiation boundary condition, the periodic and non-periodic solvers are maximumly integrated together with the minimum maintenance cost.

Benefiting from the exponential convergence and flexibility of the SEBI, computationally challenging problem can be solved with considerably reduced number of samplings. As a typical application, the multilayer defects analysis in extreme ultraviolet (EUV) lithography is studied for both 2-D and 3-D models. The light absorption engineering of graphene is also investigated around the visible spectra. Benefiting from the accuracy of the full-wave nonlinear solver, couplings between the fundamental frequency (FF) field and the higher harmonic (HH) field ignored my most previous studies can also be self-consistently analyzed in nonlinear optical simulation. With this tool, the investigation is extended to the engineering of graphene's visible spectra absorption tuning and third harmonic generation (THG) enhancement. Graphene's Kerr effects are also studied under strong surface plasmonic resonance. The hybrid higher order method's efficiency and accuracy are further validated through various multiscale nano-optical cases.

Contents

List of Tables

List of Figures

List of Abbreviations and Symbols

Abbreviations

Abbreviations in the text are listed here.

BI-SEM	Boundary-integral spectral element method
DDM	Domain decomposition method
DoF	Degree of freedom
EUV	Extreme ultra violet
FDTD	Finite-difference time-domain
FEBI	Finite element boundary integral
FEM	Finite element method
FF	Fundamental frequency
GLL	Gauss-Lobatto-Legendre
HH	Higher harmonic
LMGF	Layered medium dyadic Green's function
LSPR	Localized surface plasmon resonance
MoM	Method of Moments
NP	Nanoparticle
PLMGF	Periodic layered medium dyadic Green's function
RCWA	Rigorous coupled-wave analysis
SIE	Surface integral equation

SEBI-PLMGF	Spectral element boundary integral - periodic layered medium Green's function
SEM	Spectral element method
SHG	Second harmonic generation
TH	Third harmonic
THG	Third harmonic generation

Acknowledgements

I would like to express my deep gratitude to my advisor Prof. Qing Huo Liu for offering the invaluable guidance during the past five years, for introducing me to the fascinating area of computational electromagnetics in nano optical applications, and for providing useful and constructive critiques for this research work. His academic attainment and highly motivated attitude sets me a good model. I am very grateful to Prof. William T. Joines, Prof. Jungsang Kim, Prof. Adrienne Stiff-Roberts and Prof. Loren W. Nolte for being my committee members and giving me constructive suggestions.

I would also like to deliver my particular gratitude to Dr. Ma Luo, for his irreplaceable advice and insights in nano optical computation; to Dr. Yi Ren from Chongqing University of Posts and Telecommunication, for sharing his impressive knowledge in finite element method and layered medium Green's function. I appreciate the help from Yiqian Mao, the collaboration with him is happy and instructive. Thanks Dr. Mengqing Yuan from Wave Computation Technology, for his generous help and invaluable suggestions.

My special thanks are extended to a lot of colleagues at Duke: Dr. Luis Tobon, Dr. Wenji Zhang, Dr. Xueshi Li, Dr. Junwen Dai, Dr. Yu Jia, Dr. Qingtao Sun, Dr. Tianye Ma, Dr. Yi Liao, Dr. Yuanguo Zhou, Weifeng Huang, Yuan Fang, Yunyun Hu, Dezhi Wang, Runren Zhang and all members in Dr. Liu's group for their countless help and invaluable friendship.

I acknowledge the numerous supports and fantastic opportunities provided by the Duke University. It is a lifetime treasure for being a Duke community member.

Last but not least, I would liked to express my deepest gratitude for my parents, my grandmother-in-law, my grandfather, and my elder sister, for their endless care, support, and love.

1

Introduction

High efficiency numerical simulation technique in electromagnetic and optical problems has been a fundamental tool for the design and study of complex nano-scale opto-electronic structures. The past decades witnessed the rapid developments in nano-optics, where the various complex nano-scale designs and technologies evolve from laboratory prototypes to practical engineerings. Extreme ultraviolet (EUV) lithography, nano antennas and plasmonic metamaterials are the representatives of this large category of nano-scale technologies highlighted in the industrials [Wu and Kumar (2007); Vakil and Engheta (2011)]. Accompanying the engineering level applications, their design and fabrication increasingly address the importance of quantified analyses [Pomplun et al. (2007a); Lin et al. (2012); Ahmed et al. (2013)]. Considering the expensive cost of repeating experiment-based investigation, in many circumstances, the feasibility of a design largely depends on the accuracy and efficiency of the numerical solver.

Various computational methods have been proposed for the analysis of nano optics problems. Conventional high frequency approximation methods have been widely used in analyzing optical wave's propagation and scattering. However, for delicate modern nano-scale designs and fabrications, both the optical field's magnitude and phase information need to be obtained with high accuracy. The full-wave computational methods thus triumph the high frequency approximations and are focused with increasing interest in this area. However, at optical spectrum, the targeted problems are usually electrically large, especially for 3-dimensional (3-D) full-wave study. The versatile structure of the lithography pattern, optical connection and the background masks and substrate further constitute a multiscale problem. Conventional computational methods, such as finite element method (FEM) and the finite-difference time-domain (FDTD) method, have been under intensive study for their potential in nano optical computations [Saitoh and Koshiba (2001)]. Unfortunately, these approaches can hardly handle the multiscale problems. Their slow convergence also enforces a particular high sampling density inside the computation domain. Solving the final linear equation system usually consumes giant computational resources [Niu et al. (2014)]. This costly requirement in computational resources may be even increased by orders in repeated systematic simulation.

In this work, a mixed-order hybrid numerical framework is proposed for the multi-scale computation of linear and nonlinear nano optical scatterings. Starting from the principle of the spectral element boundary integral (SEBI) method, the mixed-order SEBI solver is first developed for the nano-scale linear and nonlinear electromagnetic scattering analyses in homogeneous background. The SEBI realizes the exact radiation boundary condition with a set of surface integral equations (SIE's), while discretizing the whole computation domain with the fast convergent Gauss-Lobatto-Legendre (GLL) basis function. In nonlinear optical simulations, full-wave results can be obtained self-consistently by iteratively solving the vector Helmholtz equations at each harmonic frequency. For the curve-boundary geometries, a high order Jacobian matrix can be utilized to generate the curve-edge boundary, so that the error caused by the preprocessing process can be minimized. Moreover, considering the periodic nature of many large scale optical frequency applications, the Bloch periodic boundary condition is further applied to largely reduce the number of unknowns in the final equation system. As another improvement, the block-Thomas method is used to further enhance the efficiency of the direct solver.

To further address the multiscale scattering analysis in nano optics, a hybrid framework is developed by combing the SEBI solver with periodic layered medium dyadic Green's function (PLMGF) and the domain decomposition method (DDM).

The formulation and implementation of the PLMGF is systematically discussed in both regular wave function formulation and matrix-friendly formulation. The dyadic PLMGF is highly singular in general. The hyper singularities occur when both the source and the observation points are on the same layered medium interface. To fully address the sampling capability in this situation, a feasible and effective singularity extraction technique is proposed under the matrix-friendly formulation.

By formulating the SIE's with the PLMGF, all unknowns in the background layered medium are pushed to the radiation boundaries. Thus, the whole planar layered background can be truncated from the computation domain. Considering its highly singular analytical properties, the PLMGF is carefully and systematically formulated under matrix representation within the SEBI context. All PLMGF-related SIE components can be efficiently evaluated through extracting the primary and secondary terms' singularities separately,

The Riemann solver based DDM is developed for splitting the SEBI computation domain into multiple volume subdomains together with another boundary surface integral subdomain. Through this endeavor, a large scale problem can be divided into multiple smaller problems less demanding in computational resources. Moreover, a scattered field hybrid radiation boundary condition is proposed to fully address the necessity of non-periodic simulations. By first formulating both the wave equation and the SIEs with scattered field unknowns, and then combining the perfectly matched layer (PML) with the surface integral equations (SIEs), the SEBI solver is able to switch between periodic and non-periodic modeling with the minimum cost.

The rest of this thesis is organized as follows.

Chapter 2 provides a fundamental scheme of the mix-order SEBI method in frequency domain, especially with respect to its application in nano optical simulations. Starting from the field-source relation in electromagnetic/ optical problems, the theory and discretization rule of the BI-SEM is systematically introduced. Interpolating both the interior volume domain and the radiation surfaces with the GLL basis functions, the exponential convergence is expected to be obtained throughout the computation domain. Focusing on the nano optical computation applications, the periodic homogeneous Green's function and the Bloch periodic boundary condition is rigorously applied. The PLMGF capability will be integrated into the proposed numerical framework in the continuing chapters. Following the same philosophy, a fast convergent full-wave solver for nonlinear optical process is further proposed.

With the advantage of the developed numerical solver, several nano-scale engineering investigations are conducted in Chapter 3 - 5. As a typical application of the multiscale SEBI solver in linear nano optics, the multilayer defects analysis in extreme ultraviolet (EUV) lithography is provided in Chapter 3. The multilayer distortion caused by the mask defects is regarded as one of the critical challenges of EUV lithography. Here the developed BI-SEM solver is used to simulate the influence of the defected nano-scale structures with high accuracy and efficiency. Through comparing the performance of this method with the conventional finite element method, it is shown that the proposed BI-SEM can greatly decrease both the memory cost and computation time. For typical 2-dimensional (2-D) problems, we show that the BI-SEM is 11 and 1.25 times more efficient than the FEM in terms of memory and CPU time, respectively, while for 3-D problems, these factors are over 14 and 2, respectively, for smaller problems; realistic 3-D problems that cannot be solved by the conventional FEM can be accurately simulated by the BI-SEM.

In Chapter 4, graphene's light absorption engineering around the visible spectra is investigated using the nonlinear SEBI solver with homogenous Green's function. The strategy of combing various types of nanoparticle cluster arrays with a special Bragg reflector is systematically studied to stimulate a particularly strong localized surface plasmonic resonance (LSPR). In the spectra of 300 nm to 1000 nm, a maximum light absorption of 67.54% is observed for the graphene layer with optimal parameters of the photodetector model.

Starting from this outstanding photo-responsivity, Chapter 5 extends the research into quantitative third harmonic generation (THG) analysis, especially graphene's third harmonic characteristics under strong surface plasmonic resonances. Both the enhancement strategy of THG with strong LSPR and graphene's optical and electro-optic Kerr effects are investigated in this chapter. In the concerned spectra, graphene's THG conversion rate is enhanced by 4.4×10^5 times. Simultaneously applying electro-optic Kerr process can further boost the THG emission. However, its contribution is only secondary compared with LSPR. This study briefly discusses the THG conversion efficiency of the bilayer and trilayer graphene models under strong LSPR.

Delicate nano patterns and optical connections embedded in electrically large multi-layer structures consists of the most common multiscale model in nano optics. A critical step in the solution is to incorporate the PLMGF in the hybrid numerical solver. Chapter 6 systematically formulates the PLMGF under both wave function formulation and matrix-friendly formulation, which serves as the foundation of the endeavors in Chapter 7. The hyper singularity of the PLMGF limits its application under certain prerequisites. To enable the sampling feasibility under general conditions, a novel and feasible singularity extraction technique is proposed under the matrix-friendly formulation.

Chapter 7 extends the mixed-order SEBI solver proposed in Chapter 2 to a hybrid framework for multiscale simulations. First, the SEBI is re-formulated with dyadic Green's function for the background region. The PLMGF is then combined with the original SEBI solver. Within the proposed SEBI-PLMGF framework, the minimum discretization region only contains the principal cell of the periodic scatterer, while the whole layered medium background is truncated from the computation domain. Noticing the PLMGF's hyper-singular analytical properties, the matrix representation is systematically derived for the primary terms and secondary terms separately. The strong singularity issue is thus considerably relieved. Several numerical cases are presented to validate the formulation.

Chapter 8 theoretically investigates the DDM to the SEBI and proposes an integrated periodic/ non-periodic solver framework. Based on the Riemann solver transmission boundary condition, the DDM is applied to both the SEM subdomain and the MoM subdomain. To fully address both periodic and non-periodic modelings in nano optics, a novel framework is proposed for integrated analysis of periodic and non-periodic structures in piecewise homogeneous background. The proposed numerical scheme hybridizes the perfectly matched layer and the surface integral equations (SIE's) for lateral and top/bottom boundaries, respectively. With this hybrid absorbing boundary condition, the integrated solver can switch between periodic simulation and non-periodic simulation with minimum cost. These endeavors equips the multiscale SEBI method with the capabilities for more versatile nano optical computations.

Chapter 9 summarized the primary contribution of this work. The key steps and the critical components of the proposed multiscale higher order method is revisited. Through the theoretical analysis and the various numerical examples in this work, it is concluded that the multiscale SEBI framework serves as a competitive solution for nano optical computations. Applicable further research topics are also proposed in this chapter.

2

Fundamental Scheme of the Spectral Element - Boundary Integral Method

2.1 Maxwell's equations and wave equations

The source-field relation in electromagnetic theory is governed by the Maxwell's equations, which are

$$\nabla \times \mathbf{E} = -\mathbf{M}_i - j\omega\mathbf{B} \tag{2.1}$$

$$\nabla \times \mathbf{H} = \mathbf{J}_i + \mathbf{J}_c + j\omega\mathbf{D} \tag{2.2}$$

$$\nabla \cdot \mathbf{D} = q_{ev} \tag{2.3}$$

$$\nabla \cdot \mathbf{B} = q_{mv} \tag{2.4}$$

where $\mathbf{E}$ is the electric field intensity; $\mathbf{H}$ is the magnetic field intensity; $\mathbf{D}$ is the electric flux density; $\mathbf{B}$ is the magnetic flux density; $\mathbf{M}_i$ is the impressed magnetic current source density; $\mathbf{J}_i$ is the impressed electric current source density; $\mathbf{J}_c$ is the conduction electric current density; q_{ev} and q_{mv} are the volume electric and magnetic charge density, respectively.

Starting from the differential form Maxwell's equations, the electric field Helmholtz wave equation can be obtained by taking the derivative of Eq. (2.2), with Eq. (2.1) inserted:

$$\nabla \times [\mu_r^{-1}(\nabla \times \mathbf{E})] - k_0^2 \epsilon_r \mathbf{E} + j\omega\mu_0 \mathbf{J} + \nabla \times \mu_r^{-1} \cdot \mathbf{M} = \mathbf{0} \tag{2.5}$$

where $k_0 = \frac{\omega}{c}$ is the wave number in vacuum; ϵ_r and μ_r are the relative permittivity and relative permeability of the medium. Equation (2.5) sufficiently describes the time harmonic field-source relation in frequency domain electromagnetic problems, and serves as the foundation of the frequency domain modeling of the interaction between electromagnetic field and physical objects in this work.

A major category of large-scale systems in nano optical applications employs periodic structures. The periodicity can be utilized to simplify the complexity of the computational modeling. For instance, for each unit of the periodic structure, both the electric field and the magnetic field on the periodic boundaries satisfy the Floquet theorem. In other words, the electric field and the magnetic field should be continuous at the interfaces between adjacent periodic units, and relate to those on the opposite periodic surface with a constant phase shift. This relation contributes to a significant reduction in the computational system's degree of freedom. More details about the principle and implementation of the Bloch periodic boundary condition will be discussed in detail in Section 2.3.

2.2 Principle of the boundary integral - spectral element method

The boundary integral - spectral element (SEBI) method in principle combines the mixed-order spectral element method (SEM) with the surface integral equations (SIE's) as a solution to the vector Helmholtz equation. The SEM has been proposed as a fast convergent method for both 2-D and 3-D computational electromagnetic problems. Using a special category of interpolation basis functions, the exponential convergence can be obtained for the models without field singularities. On the other hand, although the SEM exhibits good performance within the discretized domain, in most electromagnetic modelings the physical objects are placed in penetrable background. A radiation boundary condition is thus necessary to be enforced.

The SEBI method includes a set of surface integral equations as the exact radiation boundary condition, with only a minor increase of the number of unknowns. Under the SEBI framework, the interior region with complex inhomogeneities is solved by the SEM. Different from the SEM domain, the radiation boundary surfaces are treated with the method of moments (MoM). Discretizing both the interior volume and the boundary surfaces with the higher order basis function, fast convergence can be expected throughout the computation domain [Luo and Liu (2009); Hu (1995); Niu et al. (2015)].

The interpolation principle of the SEBI is similar to that of the finite element - boundary integral (FEBI) method, but with difference choice of vector basis functions to improve the accuracy and efficiency. In FEBI method, the field is interpolated by the low order polynomials, which only has second order accuracy. However, by interpolating with the Gauss-Lobatto-Legendre (GLL) polynomials, a spectral accuracy can be achieved in both SEM and MoM domain in two-dimensional (2-D) and three-dimensional (3-D) simulations [Luo and Liu (2009); Hu (1995)]. In other words, with the increase of the basis function's order, the numerical error decreases exponentially instead of quadratically.

Apply the Galerkin's method to Eq. (2.5), the weak form of the Helmholtz equation can be obtained as

$$\begin{aligned} &\int_V [(\nabla \times \mathbf{\Phi_i})^T \cdot \mu_r^{-1} \cdot (\nabla \times \mathbf{E}) - k_0^2 \cdot (\epsilon_r \mathbf{\Phi_i})^T \cdot \mathbf{E}] dV \\ &\qquad - j k_0 \int_S \mathbf{\Phi}_i^T \cdot (\hat{n} \times \bar{\mathbf{H}}) dS = \mathbf{0}. \end{aligned} \tag{2.6}$$

Here the normalized magnetic field is employed in Eq. (2.6), which is defined as $\bar{\mathbf{H}} = \sqrt{\frac{\mu_0}{\epsilon_0}}\mathbf{H}$, and $\mathbf{\Phi}$ denotes the basis function in the physical domain.

The arbitrary shape target is simulated within a finite computation domain in general. As a result, when implementing the numerical simulation method for a target in the open space, an outer boundary condition needs to be applied to truncate the unbounded surface [Vouvakis et al. (2004)]. Here the electric field integral equation (EFIE) and the magnetic field integral equation (MFIE) are used to describe the electric field and magnetic field on the truncation boundary

$$\mu_r \mathscr{L}(\tilde{\mathbf{J}}_s) - \frac{1}{2}\mathbf{M}_s + \mathscr{K}(\mathbf{M}_s) = \hat{n} \times \mathbf{E}_p^{inc} \quad \text{(EFIE)} \tag{2.7}$$

$$\epsilon_r \mathscr{L}(\mathbf{M}_s) + \frac{1}{2}\tilde{\mathbf{J}}_s - \mathscr{K}(\tilde{\mathbf{J}}_s) = \hat{n} \times \tilde{\mathbf{H}}_p^{inc} \quad \text{(MFIE)} \tag{2.8}$$

where $\hat{n}$ is the outward normal direction, $\tilde{\mathbf{J}}_s = \hat{n} \times \bar{\mathbf{H}}$ is the equivalent surface electric current density, and $\mathbf{M}_s = -\hat{n} \times \mathbf{E}$ is the equivalent surface magnetic current densities; the subscript p is used to denote the medium at the truncation surface (top surface or bottom surface) of the computation domain. Note that the top and bottom media can be different and thus their Green's function can be different. In addition, the integral operators in the EFIE and the MFIE for the top and bottom boundaries are defined as below

$$\begin{aligned} \mathscr{L}(\mathbf{X}(\mathbf{r}')) = jk_0\hat{n} \times (&\int_S g_p(\mathbf{r},\mathbf{r}')\mathbf{X}(\mathbf{r}')dS' \\ &+\frac{\nabla}{k_p^2}\int_S g_p(\mathbf{r},\mathbf{r}')\nabla_s' \cdot \mathbf{X}(\mathbf{r}')dS'), \end{aligned} \tag{2.9}$$

$$\mathscr{K}(\mathbf{X}(\mathbf{r}')) = \hat{n} \times \fint_S \nabla g_p(\mathbf{r},\mathbf{r}') \times \mathbf{X}(\mathbf{r}')dS', \tag{2.10}$$

where $g_p(\mathbf{r},\mathbf{r}')$ is the scalar Green's function in the homogeneous background medium, and k_p is the wavenumber at the background medium; $\mathscr{K}$ is the Cauchy principal integral operator with the singular point at $\mathbf{r} = \mathbf{r}'$ removed. Furthermore, if the problem is Bloch periodic in the lateral directions, g_p is the corresponding periodic Green's function.

Inserting the MFIE into the weak-form wave equation while simultaneously applying the Galerkin's method to the EFIE, we can obtain the weak-form SEBI equations for the scattering problem. The combined weak form of Helmholtz equation and that of the EFIE are given as

$$\begin{aligned}\int_V [(\nabla \times \mathbf{\Phi_i})^T \cdot \mu_r^{-1} \cdot (\nabla \times \mathbf{E}) - k_0^2 \cdot (\epsilon_r \mathbf{\Phi_i})^T \cdot \mathbf{E}]dV \\ -2jk_0 \int_S \mathbf{\Phi}_i^T \cdot [\mathscr{K}(\tilde{\mathbf{J}}_s) - \epsilon_r \cdot \mathscr{L}(\mathbf{M}_s)]dS \\ = 2jk_0 \int_S \mathbf{\Phi}_i^T \cdot (\hat{n} \times \tilde{\mathbf{H}}_p^{inc})dS,\end{aligned} \tag{2.11}$$

$$\begin{aligned}jk_0 \int_S \mathbf{\Phi}_i^T \cdot [\mu_r \mathscr{L}(\tilde{\mathbf{J}}_s) + \frac{1}{2}\hat{n} \times \mathbf{E} + \mathscr{K}(\mathbf{M}_s)]dS \\ = jk_0 \int_S \mathbf{\Phi}_i^T \cdot (\hat{n} \times \mathbf{E}_p^{inc})dS.\end{aligned} \tag{2.12}$$

To achieve the spectral accuracy, the mixed-order GLL element discretization is used in both the interior domain and the boundary surfaces [Luo et al. (2010); Lee and Liu (2005); Luo and Liu (2011); Luo et al. (2013); Niu et al. (2015)]. For each mesh element, the fields are expanded by a set of mixed order GLL basis functions. Meanwhile, the coordinates in each element can be mapped to a reference domain defined as $(\xi, \eta, \zeta) \in [-1, 1] \times [-1, 1] \times [-1, 1]$.

In one dimension, the N-th order GLL basis function can be expressed in the reference domain by

$$\phi_j^{(N)} = \frac{-1}{N(N+1)L_N(\xi_j)} \frac{(1-\xi^2)L_N'(\xi)}{\xi - \xi_j}, \tag{2.13}$$

where $L_N(\xi)$ is the N-th order Legendre polynomial and the nodal points ξ_j for $j = 0, 1, ...N$ are chosen as the roots of $(1 - \xi_j^2)L_N'(\xi_j) = 0$.

Based on the above formulas, the 3-D mixed-order vector basis functions can be written as [Lee et al. (2006)]

$$\tilde{\mathbf{\Phi}}^{\xi}_{rst} = \hat{\xi}\phi_r^{(N_\xi-1)}(\xi)\phi_s^{(N_\eta)}(\eta)\phi_t^{(N_\zeta)}(\zeta) \tag{2.14}$$

$$\tilde{\mathbf{\Phi}}^{\eta}_{rst} = \hat{\eta}\phi_r^{(N_\xi)}(\xi)\phi_s^{(N_\eta-1)}(\eta)\phi_t^{(N_\zeta)}(\zeta) \tag{2.15}$$

$$\tilde{\mathbf{\Phi}}^{\zeta}_{rst} = \hat{\zeta}\phi_r^{(N_\xi)}(\xi)\phi_s^{(N_\eta)}(\eta)\phi_t^{(N_\zeta-1)}(\zeta) \tag{2.16}$$

where $(\phi_r^{(N_\xi)}, \phi_s^{(N_\eta)}\phi_t^{(N_\zeta)})$ are the scalar basis functions with (N_ξ, N_η, N_ζ) interpolation orders along $(\hat{\xi}, \hat{\eta}, \hat{\zeta})$ directions, respectively. As a result, the electric field and the magnetic field can be expanded by the vector GLL basis functions as

$$\mathbf{E}(\xi,\eta,\zeta) = \sum_{i=1}^{N} E_i \tilde{\mathbf{\Phi}}_i \tag{2.17}$$

$$\mathbf{H}(\xi,\eta,\zeta) = \sum_{j=1}^{N_S} H_j \tilde{\mathbf{\Phi}}_j \tag{2.18}$$

where N and N_S are the total number of the basis functions in the whole computation domain and on the boundary surface, respectively; $\tilde{\mathbf{\Phi}}$ denotes the GLL vector basis function in the reference domain; $\{E_i\}$ and $\{H_j\}$ are the set of field unknowns we are solving for.

Inserting the vector basis expansion of the electric field and the magnetic field to Eq. (2.11) and Eq. (2.12), the weak-form equations can be discretized with the spectral element. In order to keep the tangential components of the fields continuous, the covariant mapping and contravariant mapping between the reference domain and the physical domain are given by

$$\mathbf{\Phi} = \mathbf{J}^{-1}\tilde{\mathbf{\Phi}} \tag{2.19}$$

$$\nabla \times \mathbf{\Phi} = \frac{1}{|\mathbf{J}|}\mathbf{J}^T \nabla \times \tilde{\mathbf{\Phi}} \tag{2.20}$$

for the basis functions and curl operation, respectively, where $\mathbf{J}$ is the Jacobian matrix, defined as

$$\mathbf{J} = \begin{bmatrix} \frac{\partial x}{\partial \xi} & \frac{\partial y}{\partial \xi} & \frac{\partial z}{\partial \xi} \\ \frac{\partial x}{\partial \eta} & \frac{\partial y}{\partial \eta} & \frac{\partial z}{\partial \eta} \\ \frac{\partial x}{\partial \zeta} & \frac{\partial y}{\partial \zeta} & \frac{\partial z}{\partial \zeta} \end{bmatrix}. \tag{2.21}$$

It is worth noting that even though the high order spectral element greatly decreases the numerical error at a modest additional cost, this improvement still can be offset by the errors in modeling the geometry structure. When analyzing the multi-layer defected model, the fine structure and the curved boundaries make this issue increasingly non-negligible.

Fortunately, with the covariant mapping given in Eq. (2.19) and Eq. (2.20), further improvements can be achieved by using the basis function defined on elements with curved surfaces. For a general curved hexahedron, given appropriate control points, the high order scalar basis functions can be utilized to map the coordinates from the reference domain to the physical domain :

$$x = \sum_{i=1}^{I} \sum_{j=1}^{J} \sum_{k=1}^{K} x_{ijk} B_{ijk} \tag{2.22}$$

$$y = \sum_{i=1}^{I} \sum_{j=1}^{J} \sum_{k=1}^{K} y_{ijk} B_{ijk} \tag{2.23}$$

$$z = \sum_{i=1}^{I} \sum_{j=1}^{J} \sum_{k=1}^{K} z_{ijk} B_{ijk} \tag{2.24}$$

where $(x_{ijk}, y_{ijk}, z_{ijk})$ are the coordinates of the given control points; (I, J, K) are the number of interpolation points in (ξ, η, ζ) directions, respectively; B_{ijk} is the set of high order scalar basis functions defined throughout the reference domain. Compared with the cuboid element, the curved-side elements are capable of significantly reducing the error occurring in the geometry modeling process.

2.3 Enforcement of the Bloch Periodic Boundary Condition

Different from the philosophy of realizing the radiation boundary condition in the SEBI framework, the enforcement of the periodic boundary condition is derived under the spectral element method framework for boundary value problems. Before enforcing the Bloch boundary conditions to the lateral surfaces of the computation domain, we first discretize the unknowns in the weak-form wave equations and the SIE's.

One of the major advantages of the SEBI or SEM originates from the GLL interpolation basis function. Compared with the linear convergence of the conventional finite element method, the SEM exhibits exponential convergence with respect to the increase of the order of interpolation polynomials. Discretizing both the SEM and MoM domain with the GLL basis function, Eq. (2.11) - (2.12) arrive at the linear equation system:

$$\begin{bmatrix} \mathbf{K}_{II} & \mathbf{K}_{IS} & \mathbf{0} \\ \mathbf{K}_{SI} & \mathbf{K}_{SS} + \mathbf{U}^H & \mathbf{V}^H \\ \mathbf{0} & \mathbf{V}^E & \mathbf{U}^E \end{bmatrix} \cdot \begin{bmatrix} \mathbf{E}_I \\ \mathbf{E}_S \\ \tilde{\mathbf{H}}_S \end{bmatrix} = \begin{bmatrix} \mathbf{0} \\ \tilde{\mathbf{H}}^{inc} \\ \mathbf{E}^{inc} \end{bmatrix}, \tag{2.25}$$

where $\mathbf{K}$ block matrices are the combination of the mass matrix and the stiffness matrix from the SEM formulation. Their first and second subscripts denote the subdomain of the testing and basis functions, respectively. The subscript I denotes the interior computation domain; S denotes the radiation boundary surfaces domain. $\mathbf{U}, \mathbf{V}$ represent the block impedance matrices corresponding to the integral operators $\mathscr{L}$, $\mathscr{K}$, respectively. The superscripts above $\mathbf{U}, \mathbf{V}$ denote the corresponding integral operator is applied to electric field unknowns or magnetic field unknows. Through the above linear sparse equation system, the exponential convergence is expected for both the SEM domain and the MoM boundary surfaces.

Without loss of generality, assume the periodicity in along x and y directions. Thus, under the proposed SEBI framework for periodic scatterers, the top and bottom radiation boundaries have been realized by the surface integral equations with the periodic homogeneous Green's function. The lateral boundaries of the computation domain are truncated with the Bloch periodic boundary condition:

$$\mathbf{E}(\mathbf{r}+\mathbf{a}) = \mathbf{E}(\mathbf{r})e^{-j\mathbf{k}\cdot\mathbf{a}} \tag{2.26}$$

$$\mathbf{H}(\mathbf{r}+\mathbf{a}) = \mathbf{H}(\mathbf{r})e^{-j\mathbf{k}\cdot\mathbf{a}} \tag{2.27}$$

where $\mathbf{k} = \hat{x}k_x^i + \hat{y}k_y^i$ is the Bloch wave vector; $\mathbf{a} = \hat{x}L_x + \hat{y}L_y$ is the lattice vector; $\mathbf{r}$ and $\mathbf{r}+\mathbf{a}$ are the position vectors of the two corresponding points located at two opposite periodic boundary surfaces. Noticing that the SEBI utilized localized GLL basis functions for discretization, Eq. (2.26) - (2.27) are only enforced on $\mathbf{E}$'s tangential components on the periodic boundary surfaces of the whole computation domain, and $\mathbf{H}$'s tangential components on the boundary edges of the top and bottom surfaces.

Equation (2.25) can be more compactly written as

$$\mathbf{A}\cdot\mathbf{u} = \mathbf{b}. \tag{2.28}$$

To apply the Bloch boundary condition to the linear equation system, we first classify vector $\mathbf{u}$ according to each unknown's location:

$$\mathbf{u} = [\mathbf{u}_{in}, \mathbf{u}_{x1}, \mathbf{u}_{x2}, \mathbf{u}_{y1}, \mathbf{u}_{y2}, \mathbf{u}_{xy1}, \mathbf{u}_{xy2}, \mathbf{u}_{xy3}, \mathbf{u}_{xy4}]^T \tag{2.29}$$

where $\mathbf{u}_{x1}$ and $\mathbf{u}_{x2}$ are the corresponding unknown pair with x-periodicity; $\mathbf{u}_{y1}$ and $\mathbf{u}_{y2}$ are the corresponding unknown pair with y-periodicity; $\mathbf{u}_{xy1}$, $\mathbf{u}_{xy2}$, $\mathbf{u}_{xy3}$ and $\mathbf{u}_{xy4}$ are with dual periodicity in x and y directions.

The Floquet theorem implies that

$$\mathbf{u}_{x2} = \mathbf{u}_{x1}\cdot e^{-jk_xL_x} \tag{2.30}$$

$$\mathbf{u}_{y2} = \mathbf{u}_{y1}\cdot e^{-jk_yL_y} \tag{2.31}$$

$$\mathbf{u}_{xy2} = \mathbf{u}_{xy1} \cdot e^{-jk_x L_x} \tag{2.32}$$

$$\mathbf{u}_{xy3} = \mathbf{u}_{xy1} \cdot e^{-jk_y L_y} \tag{2.33}$$

$$\mathbf{u}_{xy4} = \mathbf{u}_{xy1} \cdot e^{-jk_x L_x} e^{-jk_y L_y}. \tag{2.34}$$

Equations (2.30) - (2.34) relates the corresponding unknown pairs on the PBC boundaries, so that the number of degree of freedom (DoF) can be reduced. The enforcement of Eq. (2.30) - (2.34) consists of two steps: (a) remove the dependent testing functions in the weak-form equations (b) reduce the dimension of unknowns [Nicolet et al. (2004)]. This process can be elegantly formulated by introducing the Bloch phase matrix

$$\mathbf{P} = \begin{bmatrix} \mathbf{I} & \mathbf{0} & \mathbf{0} & \mathbf{0} \\ \mathbf{0} & \mathbf{I} & \mathbf{0} & \mathbf{0} \\ \mathbf{0} & \mathbf{I} \cdot e^{-jk_x L_x} & \mathbf{0} & \mathbf{0} \\ \mathbf{0} & \mathbf{0} & \mathbf{I} & \mathbf{0} \\ \mathbf{0} & \mathbf{0} & \mathbf{I} \cdot e^{-jk_y L_y} & \mathbf{0} \\ \mathbf{0} & \mathbf{0} & \mathbf{0} & \mathbf{I} \\ \mathbf{0} & \mathbf{0} & \mathbf{0} & \mathbf{I} \cdot e^{-jk_x L_x} \\ \mathbf{0} & \mathbf{0} & \mathbf{0} & \mathbf{I} \cdot e^{-jk_y L_y} \\ \mathbf{0} & \mathbf{0} & \mathbf{0} & \mathbf{I} \cdot e^{-jk_x L_x} e^{-jk_y L_y} \end{bmatrix}, \tag{2.35}$$

where $\mathbf{0}$ and $\mathbf{I}$ are zero and identity block matrices with the appropriate dimensions, respectively.

The final linear equation system can be obtained as

$$\mathbf{P}^\dagger \mathbf{A} \mathbf{P} \cdot \tilde{\mathbf{u}} = \mathbf{P}^\dagger \mathbf{b} \tag{2.36}$$

where

$$\tilde{\mathbf{u}} = [\mathbf{u}_{in}, \mathbf{u}_{x1}, \mathbf{u}_{y1}, \mathbf{u}_{xy1}]^T \tag{2.37}$$

and the superscript † denotes Hermitian transpose.

All unknowns of the computation domain can be obtained by solving Eq. (2.36) with the knowledge of Eq. (2.30) - (2.34).

Combining the Bloch periodic boundary condition with the mixed-order GLL discretization, both 3-D and 2-D periodic models can be solved with the same version of computer software. With the application of mixed order basis function and periodic boundary condition, the numerical solver for 3-D models can be easily transformed to that of the 2-D models only with a change of the input parameter. For instance, for a 2-D model uniform in the y direction, we can directly apply the 3-D periodic scheme to a mesh with one element uniform in the y direction. By further applying the first order interpolation in the y direction, i.e. $N_\eta = 1$, the 2-D model can be simulated efficiently.

2.4 The higher harmonic generation solver based on SEBI

The principle of the SEBI method can be further extended as a solution of the nonlinear optical computation, such as the higher harmonic (HH) generation problems. During the HH process, the time harmonic optical source-field relation at all harmonic frequencies can be sufficiently described by the vector Helmholtz equation, with the dielectric polarization serves as a secondary source for the fields at all frequencies. In other words, Eq. (2.11) - (2.12) can be used to solve the optical field at various harmonic frequencies with self-consistent coupling. Conventionally, due to the difficulty in solving the nonlinear vector partial differential equations, the nonlinear optical analyzes usually ignore the influence of the mutual coupling between FF field and HH field. For instance, by ignoring the coupling between the FF field and HH field, one can only solve for the FF field without nonlinear dielectric polarization, and then apply $\chi^{(n)}$ to FF field to obtain the HH field pattern. However, this approach is not accurate in general. Although the solution can be largely simplified for many engineering background, with the increase of the field intensity, the error becomes more and more unacceptable. A typical example is the analysis of nano-structure's nonlinear performance under strong localized surface plasmonic resonance (LSPR). For this reason, a self-consistent nonlinear numerical solver is of considerable importance in both theory and application.

Instead of applying the independency approximations to simplify the partial differential equation system, here we focus on accurately solving the nonlinear optical field directly from the coupled vector wave equations. To achieve this goal, we need to update the FF field, nonlinear dielectric polarization, and the HH field iteratively. As is well known, the dielectric polarization serves as a source for nonlinear optical fields. In the proposed numerical scheme, we initially calculate the FF field induced by the incident light via the linear process. With this obtained FF field, the initial value of the HH dielectric polarization is first calculated, from which the initial value of the HH field can be solved from the vector wave equation. After all these initial values obtained, we can iteratively solve for the field unknowns at FF and HH frequency to arrive at the self-consistent solution.

Written as a block matrix equation, the FF and HH fields in each set of Eq. (2.11) - (2.12) can be described as

$$\begin{bmatrix} \mathbf{K}_{II}(k_0) & \mathbf{K}_{IS}(k_0) & \mathbf{0} \\ \mathbf{K}_{SI}(k_0) & \mathbf{K}_{SS}(k_0) + \mathbf{U}^{M}(k_0) & \mathbf{V}^{M}(k_0) \\ \mathbf{0} & \mathbf{V}^{E}(k_0) & \mathbf{U}^{E}(k_0) \end{bmatrix} \cdot \begin{bmatrix} \mathbf{E}_I(k_0) \\ \mathbf{E}_S(k_0) \\ \tilde{\mathbf{H}}_S(k_0) \end{bmatrix} = \begin{bmatrix} \mathbf{P}_i^{HHG}(k_0) \\ \tilde{\mathbf{H}}^{inc} \\ \mathbf{E}^{inc} \end{bmatrix} \tag{2.38}$$

$$\begin{bmatrix} \mathbf{K}_{II}(2k_0) & \mathbf{K}_{IS}(2k_0) & \mathbf{0} \\ \mathbf{K}_{SI}(2k_0) & \mathbf{K}_{SS}(2k_0) + \mathbf{U}^{M}(2k_0) & \mathbf{V}^{M}(2k_0) \\ \mathbf{0} & \mathbf{V}^{E}(2k_0) & \mathbf{U}^{E}(2k_0) \end{bmatrix} \cdot \begin{bmatrix} \mathbf{E}_I(2k_0) \\ \mathbf{E}_S(2k_0) \\ \tilde{\mathbf{H}}_S(2k_0) \end{bmatrix} = \begin{bmatrix} \mathbf{P}_i^{HHG}(2k_0) \\ \mathbf{0} \\ \mathbf{0} \end{bmatrix} \tag{2.39}$$

$$\vdots$$

$$\begin{bmatrix} \mathbf{K}_{II}(nk_0) & \mathbf{K}_{IS}(nk_0) & \mathbf{0} \\ \mathbf{K}_{SI}(nk_0) & \mathbf{K}_{SS}(nk_0) + \mathbf{U}^M(nk_0) & \mathbf{V}^M(nk_0) \\ \mathbf{0} & \mathbf{V}^E(nk_0) & \mathbf{U}^E(nk_0) \end{bmatrix} \cdot \begin{bmatrix} \mathbf{E}_I(nk_0) \\ \mathbf{E}_S(nk_0) \\ \tilde{\mathbf{H}}_S(nk_0) \end{bmatrix} = \begin{bmatrix} \mathbf{P}_i^{HHG}(nk_0) \\ \mathbf{0} \\ \mathbf{0} \end{bmatrix} \tag{2.40}$$

The above equations are coupled together via the secondary source terms:

$$\mathbf{P}_i^{HHG}(k_0) = \frac{1}{\epsilon_0} \int_\Omega dV \boldsymbol{\Phi}_i \cdot \mathbf{P}(k_0) \tag{2.41}$$

$$\mathbf{P}_i^{HHG}(2k_0) = \frac{1}{\epsilon_0} \int_\Omega dV \boldsymbol{\Phi}_i \cdot \mathbf{P}(2k_0) \tag{2.42}$$

$$\vdots$$

$$\mathbf{P}_i^{HHG}(nk_0) = \frac{1}{\epsilon_0} \int_\Omega dV \boldsymbol{\Phi}_i \cdot \mathbf{P}(nk_0) \tag{2.43}$$

where $\boldsymbol{\Phi}_i$ denotes the corresponding GLL basis function; $\mathbf{P}(k_0), \mathbf{P}(2k_0), ..., \mathbf{P}(nk_0)$ denote the nonlinear dielectric polarizations for the FF and each HH fields, respectively. By solving Eq. (2.38) - (2.40) iteratively, the field distribution at each harmonic frequency can be obtained self-consistently.

3

Mixed-Order SEBI for Irregular Scatterers: EUV Multilayer Defects Analysis

3.1 A Linear Nano Optics Benchmark Case with Irregular Geometry

The periodic SEBI method proposed in Chapter 2 serves as an effective solver for various applications in nano optics. The SEBI's advantages not only are demonstrated by the fast convergence compared with the conventional methods, but also reflected in its strong flexibility with mixed-order element. In this chapter, a typical extreme ultraviolet (EUV) lithography project with large and complex structures is studied with the linear SEBI solver. To demonstrate its advantage over the conventional numerical approaches, numerical accuracy and computational resource costs are compared for the benchmark case.

EUV lithography is considered as one of the most promising next-generation lithography technologies, benefiting from its feasibility with currently available exposure tools [Urbanski et al. (2012); Kwon et al. (2012); Wu and Kumar (2007); Amano et al. (2012); Badger et al. (2012); Peng et al. (2012); Li et al. (2012b)]. However, the availability of defect-free masks is one of the critical concerns before its full commercialization. More commonly, mask defects are known as a major source of the multilayer defects for the EUV lithography [Urbanski et al. (2012); Kwon et al. (2012); Amano et al. (2012); Badger et al. (2012); Feigl et al. (2006)]. A typical scenario of mask defects is that a particle originates on the lithography mask as defect core. All the multilayer materials deposited over the mask will thus be distorted, and both the phase and magnitude of light at a given position will be influenced to an unexpected degree.

A high-accuracy analysis of the influence of buried defects usually serves as the foundation for further compensation strategies. This relies heavily on a high-accuracy numerical technique for modeling and simulation. Unfortunately, given the finite computational resources, such numerical solutions are usually hard to obtain. The wavelength of the EUV laser source is currently expected to be 13.5 nm [Feigl et al. (2006)], significantly smaller than the dimensions of the practical lithography model. Even after applying the periodic boundary conditions in the lateral directions to reduce the model size, the computational domain of the whole structure is usually electrically large, thus very challenging to solve, especially in three dimensions. Currently, the mainstream numerical simulations for this problem are based on the finite-difference time-domain (FDTD) method, the conventional finite element method (FEM) [Krautschik and Nishiyama (2003); Evanschitzky et al. (2003); Pomplun et al. (2007b, 2006); Botha and Jin (2004)], and rigorous coupled-wave analysis (RCWA) [Schiavone et al. (2001); Smaali et al. (2006)]. However, these methods have a significant drawback of slow convergence because of the lower-order approximations utilized in these methods. Typically, a high sampling density of over 20 points per wavelength (PPW) is required to guarantee relatively satisfying accuracy. Because of these drawbacks, for practical applications, the computation time and the memory cost often become unacceptable. The RCWA method is computationally efficient, but it does have difficulty modeling curved defects that are common in

EUV lithography.

In this study, the developed linear SEBI solver is used to simulate the defects in both 2-D and 3-D EUV lithography structures. Compared with the conventional methods, the SEBI method can efficiently analyze the influence of the multilayer defects with high accuracy while at the same time significantly reducing the cost on both memory and computation time. We also show that the proposed SEBI method can solve a realistic 3-D EUV problem that is still very difficult to solve using the conventional FEM.

3.2 Key Formulations

Following the framework of the SEBI, the combined weak-form Helmholtz equation and the surface integral equations are given as

$$\begin{aligned} &\int_V [(\mu_r^{-1}\nabla \times \mathbf{\Phi_i})^T \cdot (\nabla \times \mathbf{E}) - k_0^2 \cdot (\epsilon_r \mathbf{\Phi_i})^T \cdot \mathbf{E}]dV \\ &\qquad -2jk_0 \int_S \mathbf{\Phi}_i^T \cdot [\mathscr{K}(\tilde{\mathbf{J}}_s) - \epsilon_r \cdot \mathscr{L}(\mathbf{M}_s)]dS \\ &\qquad\qquad = 2jk_0 \int_S \mathbf{\Phi}_i^T \cdot (\hat{n} \times \tilde{\mathbf{H}}_p^{inc})dS \end{aligned} \tag{3.1}$$

$$\begin{aligned} &jk_0 \int_S \mathbf{\Phi}_i^T \cdot [\mu_r \mathscr{L}(\tilde{\mathbf{J}}_s) + \frac{1}{2}\hat{n} \times \mathbf{E} + \mathscr{K}(\mathbf{M}_s)]dS \\ &\qquad = jk_0 \int_S \mathbf{\Phi}_i^T \cdot (\hat{n} \times \mathbf{E}_p^{inc})dS \end{aligned} \tag{3.2}$$

By inserting the vector basis expansion of the electric field and the magnetic field to Eq. (3.1) and Eq. (3.2), the weak-form equations can be discretized with the spectral element.

It is worth noting that even though the high order spectral element greatly decreases the numerical error at a modest additional cost, this improvement still can be offset by the errors in modeling the geometry structure. When analyzing the multi-layer defected model, the fine structure and the curved boundaries make this issue increasingly non-negligible. Lower order methods, such as the FEM and the FDTD, conventionally relieve this issue by discretizing the curved-shape region with dense meshes. Given the slow convergence of these method, this strategy is acceptable though it not only dramatically increases the number of unknowns, but also rapidly boots the condition number of the final equation system. However, if one keeps the same strategy for the SEBI, the power of the higher order interpolation would mostly go unrewarded.

On the contrary, the curved structure here is addressed through the higher order mapping between the physical domain and the reference domain, instead of a denser fitting of simplexes. At the step of using the covariant mapping given in Eq. (2.19) and Eq. (2.20), further improvements can be achieved by using the basis function defined on elements with curved surfaces. For regular shapes, such as the spheres, the analytical relation between x, y, z and (ξ, η, ζ) can be obtained without much effort.

For arbitrary geometries, the relation between x, y, z and (ξ, η, ζ) can be alternatively built through a nested interpolation with Eq. (2.22) - (2.24). As an example, the coordinates at the physical domain can be interpolated with the secondary order scalar basis functions defined in the reference domain:

$$x = \sum_{i}^{3} \sum_{j}^{3} \sum_{k}^{3} x_{ijk} B_{ijk}(\xi, \eta, \zeta) \tag{3.3}$$

$$y = \sum_{i}^{3} \sum_{j}^{3} \sum_{k}^{3} y_{ijk} B_{ijk}(\xi, \eta, \zeta) \tag{3.4}$$

$$z = \sum_{i}^{3} \sum_{j}^{3} \sum_{k}^{3} z_{ijk} B_{ijk}(\xi, \eta, \zeta) \tag{3.5}$$

where $\{B_{ijk}(\xi, \eta, \zeta)\} = \{\phi_i(\xi) \cdot \phi_j(\eta) \cdot \phi_k(\zeta)\}$ are the set of secondary order basis functions in the reference domain. For each dimension, we have

$$\phi_1(\alpha) = \frac{\alpha(\alpha-1)}{2} \tag{3.6}$$

$$\phi_2(\alpha) = (1+\alpha)(1-\alpha) \tag{3.7}$$

$$\phi_3(\alpha) = \frac{\alpha(\alpha+1)}{2} \tag{3.8}$$

with $\alpha = \xi, \eta, \zeta$.

Substituting these expressions into Eq. (2.21), and then each sampling point can be mapped between arbitrary shape physical domain and the cubic reference domain. Compared with the cuboid element, the curved-surface elements are capable of significantly reducing the error occurring in the geometry modeling process.

3.3 Numerical Results

In this section, we provide a series of cases to validate the method proposed above. In all the shown cases, the block-Thomas algorithm is utilized to further improve the efficiency [Meurant (1992)]. Moreover, considering the conventional finite element method is widely used as the current solution for EUV multilayer analysis in periodic structures, we further compared the performance of the SEBI method with the classical FEM.

3.3.1 2-D multilayer structure

The perfect 2-D multilayer periodic structure

To validate the proposed method for the EUV lithography model, we first consider a perfect 2-D periodic EUV mask with one-dimensional periodicity. In this case no multilayer defect exists in the model. As is shown in Fig. 3.1., the mask is periodic in the x direction, finite in the z direction, and invariant in the y dimension. Moreover, the top region is filled with air and the bottom region is the substrate, and both boundaries in y direction is open. From top going downward, the sequence of the materials is given as

(a) Absorbing capping (thickness: 12 nm, $n = 0.957 - j0.023$);

(b) Absorber layer (thickness: 75 nm, $n = 0.926 - j0.0436$);

(c) Multilayer capping (thickness: 2.5 nm, $n = 0.866 - j0.0171$);

(d) Silicon-Molybdenum bilayer: repeat 40 times (Si layer thickness: 4.17 nm with $n = 0.999 - j0.00182$, Mo layer thickness: 2.78 nm with $n = 0.924 - j0.00644$);

(e) Substrate (thickness: infinity, $n = 0.979$).

In addition, the width of the absorbing capping and the gap between each capping are both 88 nm. The top truncating boundary is at 27 nm above the absorber capping,

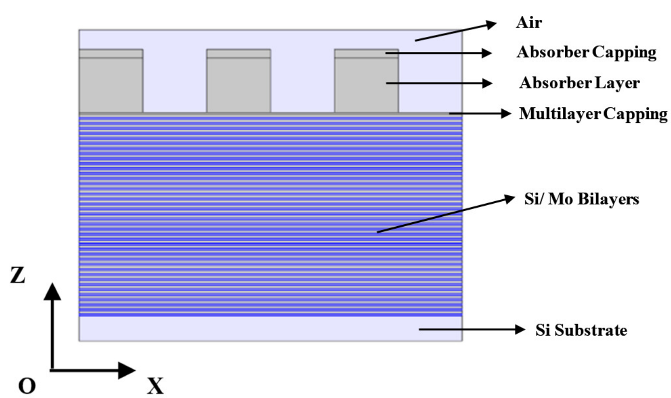

FIGURE 3.1: The structure of an EUV lithography model.

while the bottom truncating boundary is at 6.75 nm below the top substrate surface.

A TM_y wave with a wavelength of 13.5 nm is normally impinging from the top surface. Moreover, the scattered field is observed at one wavelength above the absorbing capping. Under above simulation conditions, the magnitude and the phase of the scattering field are shown in Fig. 3.2 and Fig. 3.3, respectively. From Fig.

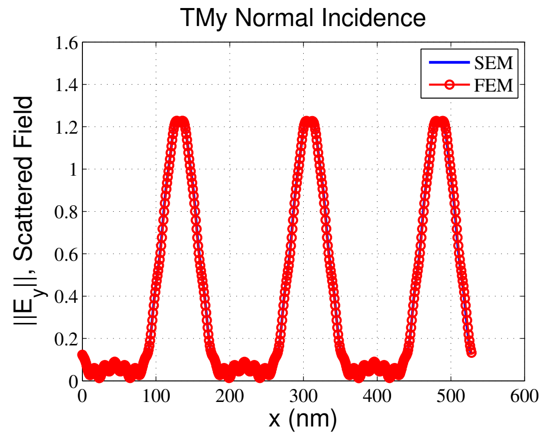

FIGURE 3.2: The magnitude of the scattered electric field E_y for the TM_y wave at normal incidence in the model in Fig. 3.1.

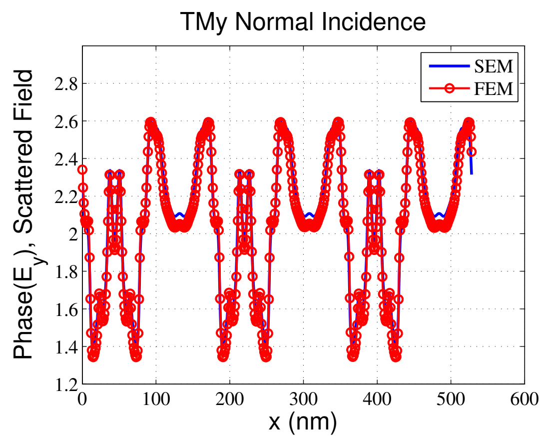

FIGURE 3.3: The phase of the scattered electric field E_y for the TM_y wave at normal incidence in the model in Fig. 3.1.

3.2 and Fig. 3.3 we can see that the SEBI results agree well with that obtained from the conventional finite element method. Further convergence tests show that the SEBI results are more accurate than the FEM results, and the discrepancy in the phase between them was due to FEM error.

The 2-D EUV lithography model with multilayer defects

Next, a 2-D EUV lithography model with multilayer defects is studied as the second example. Based on the same model in Section 3.3.1, we further study the defects generated by a core on the substrate. Therefore, all the bilayers and the capping deposed on the substrate are distorted to some degree. Since the printability of the final defect depends on the distortion of the phase and the magnitude of the light, we also focus on the phase and the magnitude of the scattered field in this defected model.

As is shown in Fig. 3.4, the model is also periodic in the x direction but invariant in the y direction. The defect core is located at the center of the gap between the 2nd and the 3rd cappings in the x direction, and affect all the bilayers. Moreover, a Gaussian function is used to describe the distortion of the Si-Mo bilayers, with the FWHM (full width at half height) being 50 nm. The height of the distortion is chosen as 3 nm for all Si-Mo bilayers.

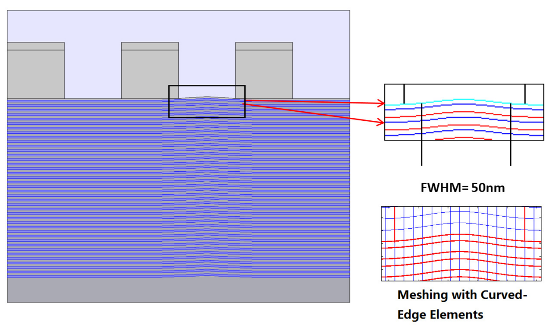

FIGURE 3.4: The Gaussian defects with an FWHM value of 50 nm and a height of 3 nm in the EUV lithography model. The right panels show the geometry of the defects and their meshing.

A TE_y plane wave is obliquely incident to this model with an incident angle of 6 degrees. Fig. 3.5 and Fig. 3.6 present the magnitude and the phase of the scattered field E_x observed one wavelength above the absorbing capping, respectively.

To achieve a comparable accuracy, a sampling density of 8 points per wavelength (PPW) is used in the SEBI scheme. Meanwhile, the sampling density is over 30 PPW for the classic FEM. However, even with such a high sampling density, the accuracy of the FEM phase result is still lower than that of the SEBI. For the model shown in Fig. 3.4, where the non-perfect periodic Si-Mo multilayer is together with

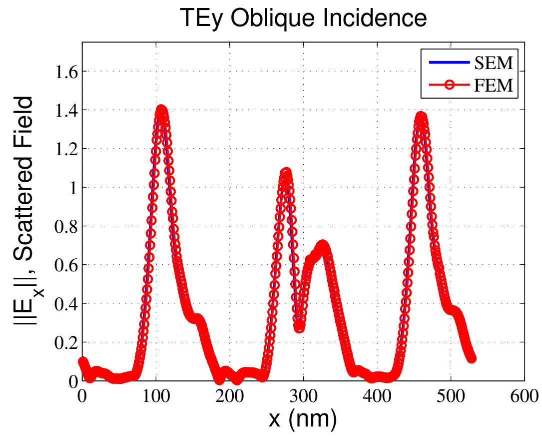

FIGURE 3.5: The magnitude of the scattered electric field E_x for the TE_y wave at 6^o oblique incidence in the defect model in Fig. 3.4.

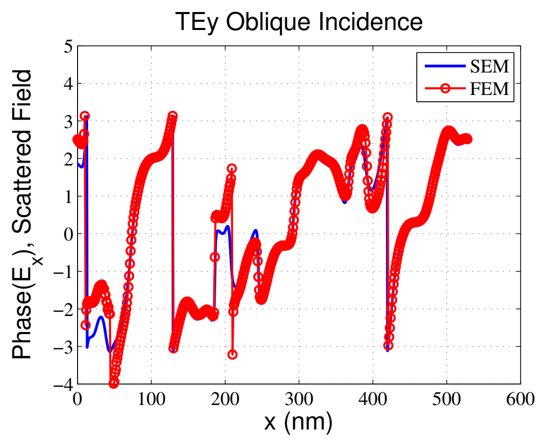

FIGURE 3.6: The phase of the scattered electric field E_x for the TE_y wave at 6^o oblique incidence in the defect model in Fig. 3.4.

defect, the SEBI has a significantly faster convergence compared with FEM. This is not only because of the spectral accuracy of the algorithm, but also is attributed to the curve-edge elements utilized in mesh generations, which largely eliminate the geometrical approximation error. Compared with the conventional method, even for the 2-D simulation cases, the SEBI employs a significant advantage in efficiency.

In practical mask inspections, measuring the far fields is usually more applicable for EUV lithography. In this study the proposed SEBI as well as the conventional FEM is dedicated to solve the near-field distribution. However, according to the near-

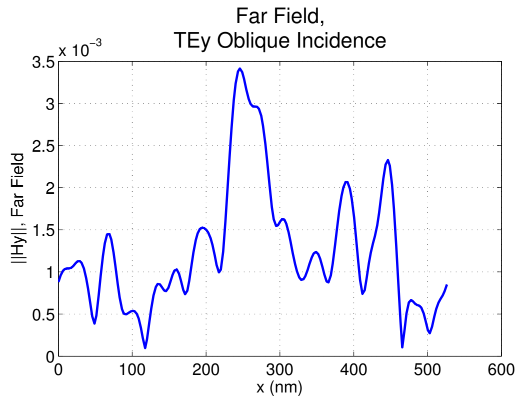

FIGURE 3.7: The far field pattern of the magnetic field for the TE_y wave at 6^o oblique incidence in the defect model in Fig. 3.4.

to-far transformation in electromagnetic theory, once we obtained the near field, the far field scattering distribution can be directly obtained through the near field information. This is a post-processing step. As a typical instance, under the oblique TE_y incidence, the far zone magnetic field at 10,000 wavelengths above the lithography object is shown in Fig. 3.7.

3.3.2 3-D multilayer periodic structures

Benefiting from the efficiency of the SEBI, the 3-D lithography model at EUV frequency can be simulated. As the first 3-D simulation case, a model without the multilayer defects is investigated. As is shown in Fig. 3.8, the model employs the same materials as that of the 2-D case, while it is also periodic in the y direction. Fig. 3.9 gives the scattered electric field $||\mathbf{E}^{sc}||$ pattern for TE_y normal incidence.

The multilayer 3-D defected model is further investigated by the SEBI method. We suppose the defects exist in each gap between the absorbing capping along the x direction. The electric field $||\mathbf{E}^{sc}||$ pattern of TE_y normal incident is given in Fig. 3.10 Through the comparison of Fig. 3.9 and Fig. 3.10, we can see that the field distribution has been greatly changed by the buried defects. Through the comparison between the perfect lithography and the defected model, an evaluation of the final

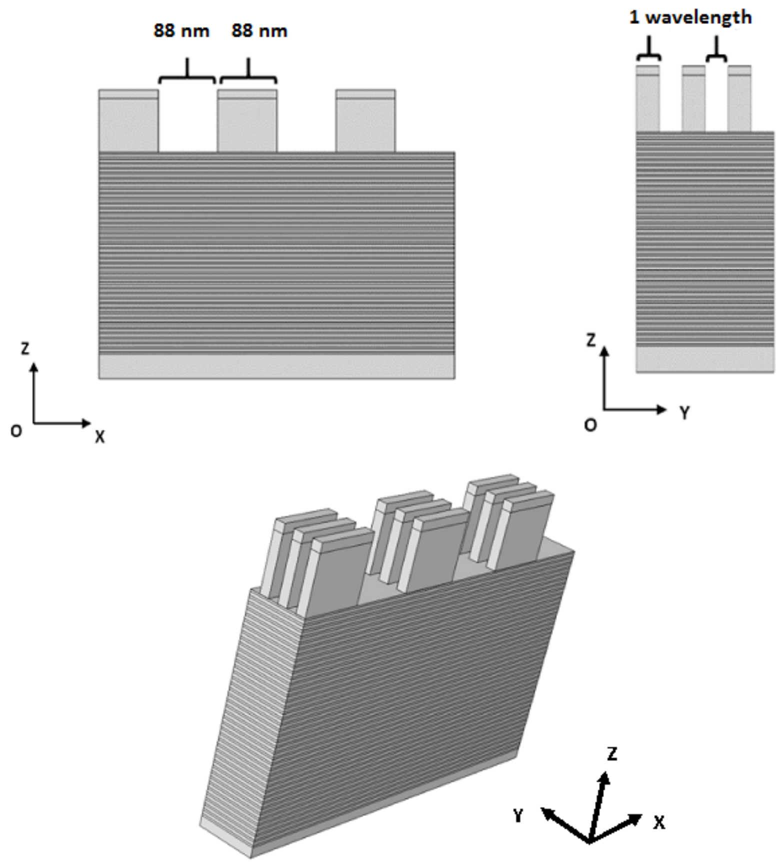

FIGURE 3.8: The 3-D EUV lithography model without defects.

printability could be achieved. Additionally, the numerical results can serve as the basis for the further lithography repair strategies.

3.3.3 The comparison of the performance between the SEBI and the classic FEM

In this section, the performance of the SEBI method and the classical FEM is compared. For the 2-D scheme, the defected model in Section 3.3.1 is simulated by SEBI and FEM separately. However, considering the complexity and the size of the defected 3-D model in Section 3.3.2, the time and memory cost of the conventional FEM will be unnecessarily large. Thus, as an alternative, a smaller size non-defect model is used for comparison in 3D. We shrink the model in the x direction by half, and remove the multilayer defects. In addition, the estimated computation cost for

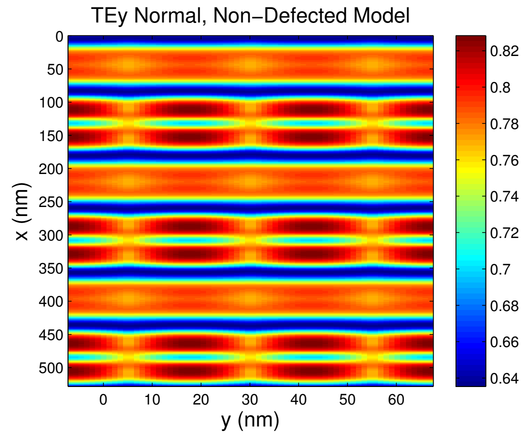

FIGURE 3.9: Scattered Electric field pattern for the TE_y wave at normal incidence in the no-defect model in Fig. 3.8.

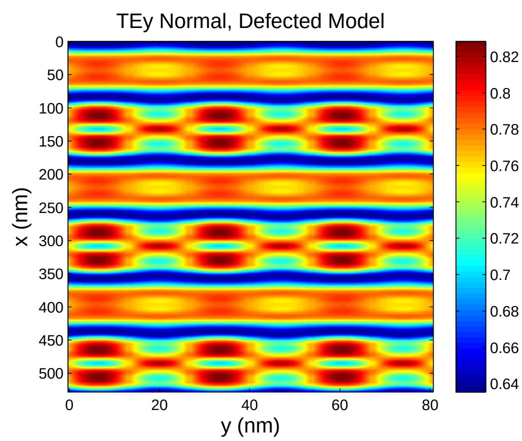

FIGURE 3.10: Scattered Electric field pattern for the TE_y wave at normal incidence with the defect added to the model in Fig. 3.8.

the original 3-D model by the FEM is also provided, which can be used as a reference for that of the SEBI.

Here the numerical errors were obtained by comparing the results with reference results when the fields are well converged. Numerically, both the SEBI method and the FEM converge to the same value with sufficient refinement. However, it is worthwhile to clarify here that the electrically large problems makes the FEM highly memory and time consuming to achieve extraordinarily accurate results. When doing a convergence test for both the SEBI and the FEM, it is shown that the SEBI converges dramatically faster with a significantly reduced requirement on computation cost. As a result, throughout this section, the well converged results obtained SEBI serve as the benchmark for calculating the receiver error.

Table 3.1: The Computation Cost – EUV Lithography

Model/Method	Time Cost	Memory Cost	Relative Error
2-D, defected / FEM	10 min	16.3 GB	3.90 %
2-D, defected / SEM	8 min	1.5 GB	0.42 %
3-D, shrunk / FEM	14 min	21.4 GB	1.08 %
3-D, shrunk / SEM	7 min	1.5 GB	0.93 %
3-D, defected / FEM	> 15 hours (estimated)	> 120 GB (estimated)	—
3-D, defected / SEM	3.6 hours	12 GB	1.61 %

The simulation is performed on a computer server with an Intel i7 CPU. To achieve the similar accuracy in the electric field pattern, the memory and time costs are shown in Table 1. For both 2-D and 3-D simulations, the SEM is more efficient than the FEM. This advantage would be even more significant with the increasing of the size and the complexity of the model, which makes the SEBI promising for many practical applications.

3.4 Conclusion

The SEBI method that combines the boundary integral equations with the spectral element method is used to simulate the extreme ultraviolet lithography multilayer defects in both 2-D and 3-D problems. Benefiting from the high accuracy of the SEM and the surface integral method used to truncate the open boundary, the hybrid scheme provides excellent efficiency and accuracy. A set of 2-D results are first provided to validate the SEBI method by comparing the numerical results of the finite element method, which serves as one of the mainstream approaches for the EUV simulation. The method is then used to investigate the 3-D EUV lithography multilayer defects. Compared with the classical finite element method, the SEBI shows significant advantages in both computation time and the memory cost.

4

The SEBI in Sub-wavelength modeling: Graphene's Absorption Enhancement via Surface Plasmonic Resonances Engineering

4.1 A Sub-Wavelength Plasmonic Engineering Case

After demonstrating the efficiency and flexibility of the linear SEBI solver, we apply it as an effective tool for graphene's linear response engineering under localized surface plasmon resonance (LSPR). Strong LSPR modelings commonly include subwavelength structures and highly focused electromagnetic fields. A fast convergence numerical tool thus can shrink the systematic simulation period considerably.

Graphene has drawn a surge of interest in both academia and industry due to its unique properties. Because of its exceptional electromagnetic and mechanical properties, such as the extremely high quantum efficiency for light-matter interactions, controllable inter-band transition and saturable nonlinear absorption, graphene is considered as a promising alternative for silicon in the next generation advanced optoelectronic devices [Wang et al. (2008); Vasko (2010)]. Meanwhile, over the past few years, a considerable number of graphene-based optoelectronic devices have been demonstrated and studied. One representative device is the graphene-based photodetector [Li et al. (2012a); Zhu et al. (2013a)]. However, despite the outstanding properties of graphene including fast carrier mobility and high quantum efficiency, some fundamental limitations still need to be overcome. Typically, the optical absorption of floated single atom layer graphene is essentially poor for a satisfying photo-responsivity. Another limitation is that graphene also shows a considerably flat absorption in the visible to near-infrared spectra, i.e., in this spectra, graphene does not provide a frequency selectivity.

One promising approach to overcome these two drawbacks is to utilize the LSPR of periodically patterned noble metal nanoparticless (NPs). With a properly designed plasmonic antenna, the photo-responsivity can be dramatically improved with significant enhancement of optical response, while simultaneously generating a frequency selectivity for the device [Zhu et al. (2013a); Echtermeyer et al. (2011); Liu et al. (2011)]. In addition, the optimal operation frequency of the device can be effectively tuned by varying plasmonic antenna's parameters. Previous research reports that gold NP arrays have been demonstrated as a promising plasmonic nano-antenna for graphene-based photodetectors with effective near field excitation and hot electron contribution [Fang et al. (2012)]. With gold plasmonic antennae, we are able to induce strong photovoltage and photocurrent in graphene-based photodetectors through enhanced light absorption in visible and near-infrared spectra.

Another critical aspect of graphene-based nano-scale photonic device design is the accuracy and efficiency of numerical techniques. Despite the promising role of graphene-based photodetectors with plasmonic antennae, its specific design is very challenging without a powerful numerical simulation technique. Currently, the prevailing numerical approaches in this area are concentrated on the finite-domain time-difference (FDTD) method and the classic finite element method (FEM). Despite the flexibility of the FDTD and the FEM, these methods suffer from a slow convergence because of their lower-order approximations. In order to guarantee satisfying accuracy, these methods usually require a sampling density of over 20 points per wavelength (PPW). Meanwhile, even though the time domain method can theoretically simulate a relatively wide spectral band, this strategy may be time- and resource-consuming in specific nano-photonic cases. For instance, when the concerned spectra is very large, the electromagnetic simulation covers both the electrically large and electrically small problems according specific frequency components. A corresponding challenge is that for electrically small problems, a large number of time steps is required to obtain the steady state results; while for electrically large problems, the computation resources required by the classical time domain methods may be prohibitively large due to the required high sampling density. In addition, under some circumstances, the frequency-dependent refractive index of various materials in the visible and near-infrared spectra cannot be described or accurately approximated as functions of frequency in analytical forms. In nano-photonic simulations, an accurate wide bandwidth solution is hence difficult to be obtained.

This section focuses on light absorption engineering of graphene around visible spectrum by LSPR of gold NPs with the spectral element boundary integral (SEBI) method. In previous studies, graphene's strong light absorption is mainly achieved in the infrared spectrum [Thongrattanasiri et al. (2012)]. However, its performance around the visible spectrum is of great significance in practical engineering designs. The research by J. Zhu et al. [Zhu et al. (2013a)] theoretically explores the performance and discipline of uniformly placed cuboid Au NPs by the FDTD method, and reaches an optimal light absorption of 30.3 %. Here, with the proposed SEBI, we further study the absorption enhancement of graphene with boosted plasmonic effects. Under the objective of improving the performance of graphene-based photodetectors, the advanced light absorption enhancement of graphene is theoretically explored with SEBI, which shows an outstanding accuracy and excellent efficiency.

Our study shows that with the light concentration by the LSPR and the electromagnetic coupling of gold nano-antennae, the tunable selective optical absorption enhancement of graphene can be achieved in the simulated spectra of 300 nm to 1000 nm. By adjusting the gold plasmonic antennae, a peak graphene absorption rate of 67.54% is obtained in the simulation frequency band. This absorption is enhanced by 30 times compared with that of the floating graphene layer, and 2.2 times with the optimal value of the research by reference [Zhu et al. (2013a)]. To our knowledge, it is also the highest reported absorption rate achieved inside graphene layer in the concerned spectra.

It is worth noting that the efficient analysis of the optical absorption largely depends on the high performance of the SEBI. Compared with the classical FEM and the FDTD, the SEBI can efficiently analyze the electromagnetic scattering problem with spectral accuracy, thus enabling fast numerical analysis of large scale graphene-based photodetectors. Considering the possible large number of unknowns when solving the assembled linear equation, an iterative solver can show a poor convergence while a direct solver can be prohibitively expensive. Thus, throughout all the simulation cases, the block Thomas algorithm is utilized to further boost the computational efficiency [Chen et al. (2011a)].

4.2 Simulation of the localized surface plasmon resonance

4.2.1 Graphene's refractive index and optical absorption

Based on the Fresnel coefficients approach [Bruna and Borini (2009)], the complex refractive index of single atom layer graphene can be described by the following equations

$$\tilde{n}(\omega) = n(\omega) + jk(\omega) \tag{4.1}$$

$$n(\omega) = 3.0, \quad k(\omega) = -\frac{c}{2\omega dn}\ln(1 - \pi\alpha) \tag{4.2}$$

where $\alpha = 1/137$ is the fine structure constant and c is the speed of light in vacuum; ω is the angular frequency; d is the thickness of the graphene layer; $n(\omega)$ is real part of the complex-value refractive index, and $k(\omega)$ is the extinction coefficient which determines the optical absorption in graphene.

The ultrathin graphene is modeled as a 2-dimensional surface characterized by the appropriate boundary conditions in many researches. However, in this research, the key for graphene's optical absorption engineering is to confine the majority of the incident energy inside the graphene layer with the LSPR. To emphasis this physical process, the single layer graphene is considered as an electromagnetic dielectric medium with a thickness of 0.34 nm in the following study. With SEBI numerical analyses, the 3-dimensional bulk description of graphene becomes even more rewarding when the researchers aims to further calculate the amount of energy confined inside the graphene or to analysis the corresponding optical field distribution.

The optical absorption of the graphene layer at an angular frequency is calculated as the ratio between the absorbed power in the graphene and the incident power, as is defined by

$$A(\omega) = \frac{P_d}{P_{inc}} = \frac{\iiint_V \omega n k \epsilon_0 |\mathbf{E}|^2 dV}{\iint_S \mathbf{S}_{inc} \cdot d\mathbf{S}} \tag{4.3}$$

where $\mathbf{S}_{inc}$ denotes the Poynting vector of the incident field impinging upon the entire structure; V is the volume of the graphene layer, and the surface integral area S is the upper intersection area of the graphene layer.

Based on above equations, the absorption engineering of the single layer graphene can be analyzed with numerical electromagnetic simulations. Theoretically, the optical absorption of a floating single layer graphene is 2.3% with an optical transmission of about 97.7% [Li et al. (2012b); Bonaccorso et al. (2010)]. In this research, our goal is to design nano-structures with a high-efficiency frequency domain computational electromagnetic technique, so that plasmonic effects can be utilized for tunable graphene absorption enhancement.

4.2.2 Computation method

In this work, the frequency domain SEBI with block-Thomas acceleration is used to efficiently analyze the absorption engineering of graphene. Under the scheme of SEBI, the interior simulation domain is computed by the spectral element method (SEM), while the radiation boundary is modeled by a set of boundary integral equations. For periodic nanostructures simulations, the Bloch periodic boundary conditions are applied to the lateral boundaries, while the top and bottom open boundaries are truncated by the boundary integral solved by method of moments (MoM) [Niu et al. (2014)].

Under the scheme of SEBI, the scattering problems reduce to solving the following equations, which combines the weak-form vector Helmholtz, the electric field integral equation, and the magnetic field integral equation:

$$\begin{aligned} &\int_V [(\mu_r^{-1}\nabla \times \boldsymbol{\Phi}_i)^T \cdot (\nabla \times \boldsymbol{E}) - k_0^2 \cdot (\epsilon_r \boldsymbol{\Phi}_i)^T \cdot \boldsymbol{E}] dV \\ -2jk_0 \int_S \boldsymbol{\Phi}_i^T \cdot [\mathcal{K}(\tilde{\boldsymbol{J}}_s) - \epsilon_r \cdot \mathcal{L}(\boldsymbol{M}_s)] dS' &= 2jk_0 \int_S \boldsymbol{\Phi}_i^T \cdot (\hat{n} \times \bar{\boldsymbol{H}}^{inc}) dS' \end{aligned} \tag{4.4}$$

$$jk_0 \int_S \boldsymbol{\Phi}_i^T \cdot [\mu_r \mathcal{L}(\tilde{\boldsymbol{J}}_s) + \frac{1}{2}\hat{n} \times \boldsymbol{E} + \mathcal{K}(\boldsymbol{M}_s)] dS' = jk_0 \int_S \boldsymbol{\Phi}_i^T \cdot (\hat{n} \times \boldsymbol{E}^{inc}) dS' \tag{4.5}$$

After obtaining the linear equation system discretized from Eq. (4.4)-(4.5), the block-Thomas algorithm is used to accelerate the solving process. The block Thomas method is designed for block tridiagonal linear systems. For our problem, the block Thomas algorithm can be used level by level for partial acceleration. Readers can refer to the reference by Chen et al. [Chen et al. (2011a)], Luo et al. [Luo et al. (2013)], Meurant et al. [Meurant (1992))]and references therein for detailed discussions and pseudo codes about this algorithm.

When simulating the cylindrical or ring geometry with conventional FEM or FDTD method, a very dense mesh must be required around the curve boundary. This is because when using the 1st order geometrical element, such as tetrahedron or rectilinear hexahedron, an especially high sampling density is needed to reduce the meshing error around the curve boundaries. If this requirement is not met, the error generated in the meshing process will inevitably compromise the overall simulation accuracy. Meanwhile, if high-order geometrical elements (curve-edge elements) are used in the mesh process for conventional FEM, it is not appropriate to expect an improvement in either the efficiency of the numerical technique or the final accuracy. This is because even though high-order geometrical elements can precisely model the complex geometry, the covariant and contravariant mapping between its physical domain and reference domain requires extra computation, which is not negligible for a relative large number of elements. Furthermore, when applying high-order geometrical elements, the associated numerical quadratures all require a higher sampling density to achieve a reasonable accuracy. For instance, the accurate result of Gauss-Lobatto-Legendre (GLL) quadrature can no longer be obtained under this circumstance. Instead, the number of sampling points must be increased according to specific cases. This requirement, in fact, brings considerable extra computation cost, and severely raises the time cost. The most common attempt to reduce the overall computing load is using higher order but larger geometrical element in the meshing process. When the high-order geometrical elements are utilized in combination with a high-order method, an acceptable improvement of the overall numerical scheme can be achieved.

Fortunately, SEBI shows a spectral accuracy inside the computation domain, by which the advantage of high-order geometrical discretization can be realized. With GLL approximation, p-refinement is much more efficient than h-refinement. Based on above facts, the relatively sparse high-order geometrical discretization becomes meaningful for SEBI. When simulating the curved edge (such as arches) structures, the mapping of the coordinates between the reference domain and the physical domain is accomplished with the interpolation of second order scalar basis functions. By decreasing the number of unknowns, the computation cost of this mapping becomes secondary and fully acceptable. With this strategy, not only the meshing error can be minimized, but also the performance of the overall numerical scheme can be boosted.

4.3 Enhancement structures and numerical results

The SEBI's high efficiency makes it an effective tool for practical designs and optimizations. With this method, a set of localized surface plasmon resonance enhancement gold nano antennae with the design of Bragg reflector are studied for graphene's optical response improvement within the spectra of 300 nm to 1000 nm. A geometrical parameters are determined in combination of systematic numerical simulations and reference researches. Additionally, the dispersive parameters of the materials are carefully taken into consideration in the numerical simulations to guarantee trustworthy results. In all the shown cases, the numerical technique is accelerated by a five-level block Thomas solver. Compared with previous study, our research shows that the optical absorption of graphene can be further enhanced with frequency selectivities.

4.3.1 Floating single layer graphene

A simple case is first studied in order to validate the proposed numerical analysis method. As is well known, theoretically and experimentally, the floating single layer graphene has a spectral non-selective optical absorption of 2.3% with almost zero reflection in the concerned spectral range of 300 nm to 1000 nm. Here the SEBI with block-Thomas acceleration is first used to calculate the optical absorption of the floating single layer graphene model.

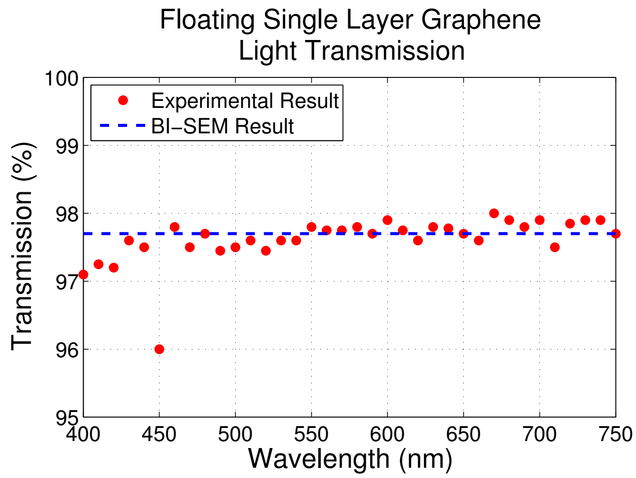

FIGURE 4.1: Light Transmission for Floating Single Layer Graphene

The numerical results as well as the experimental data from reference [Nair et al. (2008)] are given in Fig. 4.1. The result is in excellent agreement with the theoretical value, and also reasonably matches the experimental data.

4.3.2 Light absorption engineering with nanoparticles

Considering the thickness of a single layer graphene is only about 0.34 nm, the 2.3% optical absorption of the floating single layer graphene is already very impressive. However, when designing graphene-based nano-scale photonic devices, such as the graphene-based photodetectors, this light absorption is still too poor to guarantee a satisfying photoresponsivity. In this section, we propose a set of design dedicated to confine spectral selective energy inside the graphene layer by appropriate plasmon resonance excitation.

The key for effectively shaping the light absorption capability of graphene as well as the corresponding spectra is to effectively engineer the plasmon resonance generated by plasmon nano-antennae. The plasmon resonance is largely determined by the parameters of each single particle as well as the inter-particle electromagnetic coupling.

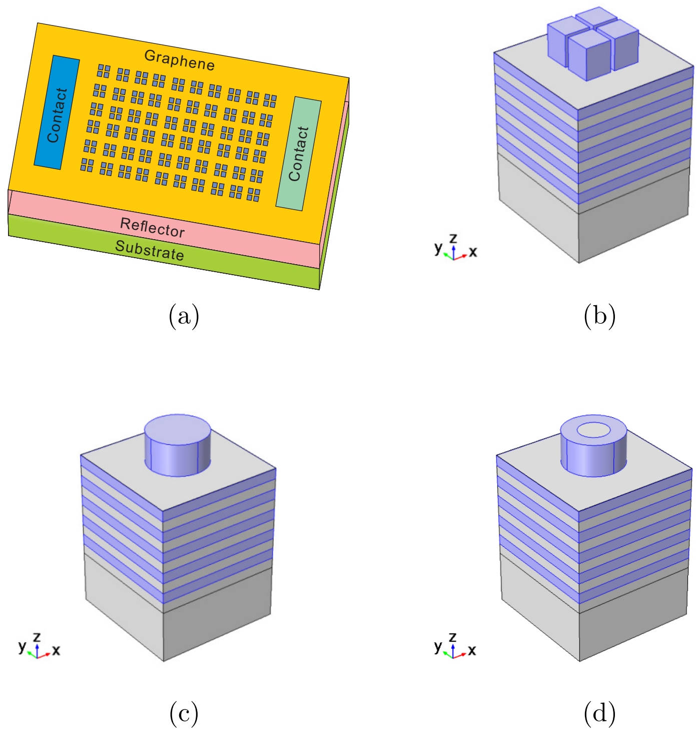

FIGURE 4.2: Sketch of (a) the schematic graphene-based photodetector; (b) cuboid cluster NP with Bragg reflector; (c) cylindrical NP with Bragg reflector; (d) ring NP with Bragg reflector.

The reference by Zhu et al. [Zhu et al. (2013a)] theoretically explores the optical absorption enhancement with uniformly placed square gold NPs, which shows that with appropriate choice of the parameters, graphene can achieve an optimal absorption of 30.3%. Here we further study the possibility of further boosting the optical absorption of graphene with plasmonic phenomena.

A schematic drawing of a graphene-based photodetector is given in Fig. 4.2a. The reflector layer generates a phase shift of the wave reflected by the substrate. By changing the thickness and structure of the reflector layer, we are able to tune the phase difference between reflective optical wave from graphene and that from the substrate. This phase difference, in fact, directly contributes to the interferometric property of the photodetector. Additionally, the noble metal NPs can act as plasmonic antennae which generate certain degree of plasmon resonance. In order to achieve optimally enhanced absorption, both the effects of optical interferences and plasmon resonances should be taken into consideration. When the intrinsic interferometric absorption peak coincides with the plasmon resonant frequency, it is expected that the enhanced near field has a good contribution to the optical loss in graphene.

4.3.3 Cuboid Au NP cluster with Bragg reflector

We first study the performance of cuboid shape Au NP clusters in comparison with the conventional uniformly distributed NPs. As mentioned above, both the parameter of single NP and the inter-particle electromagnetic coupling contribute to the graphene layer's final behavior. Here the influences of Au NP clusters inner gap, their interval, and the contribution of a specially designed Bragg reflector are all studied comprehensively.

This category of plasmonic enhancement strategy is shown in Fig. 4.2b. The periodic Au NP clusters are incorporated into the photodetectors directly above the graphene layer. Keeping the total area of the top noble metal surface as 2500 nm^2, each NP cluster consists of 4 identical cuboid Au NPs with the side length of 25 nm. In addition to the Au antenna cluster, the classical silica reflector is replaced by a specially designed Bragg reflector, which is placed below graphene. In this model, the Bragg reflector consists of 6 Si/SiO_2 bilayers, where the thickness of each bilayer is 100 nm+100 nm. Below the Bragg reflector is the silicon substrate. In numerical simulation, the substrate is appropriate to be considered as infinitely thick. Thus the substrate can be truncated by the EFIEs and MFIEs at its top surface, making the computation domain much smaller than the conventional FDTD method.

As another validation of SEBI code, a comparison of the numerical results calculated from SEBI and FEM are provided in Fig. 4.3. With a 4-th generation Intel

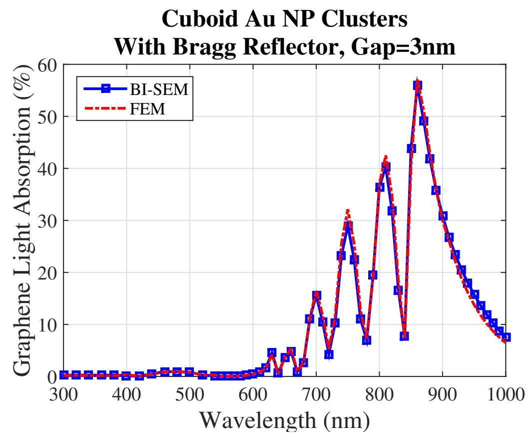

FIGURE 4.3: Simulation results from SEBI and FEM.

i-7 CPU, FEM requires 354 min and 9.8 GB memory to obtain the numerical results of one single design, while the computation cost of SEBI is 59 min and 3 GB, respectively.

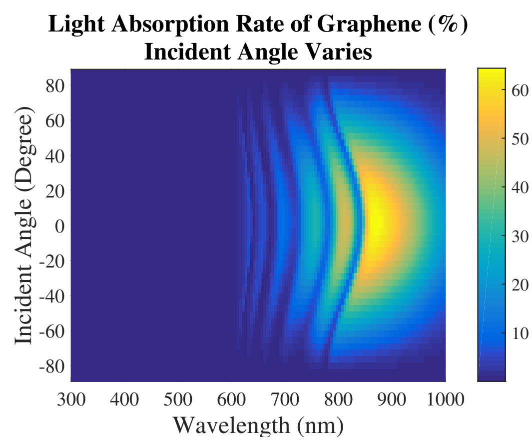

FIGURE 4.4: Cuboid NPs with Bragg reflector, incident polar angle varies.

In all the following systematic simulations, normal incident optical fields are applied to the graphene-based model, which is also the most common situations in practical engineering. However, considering the Bragg reflector behaves sensitively under oblique incidence, its contribution becomes an interesting and meaningful topic when coupling with the LSPR. Figure 4.4 provides the light absorption rate of graphene under various incident polar angles. In this model, the distance between adjacent

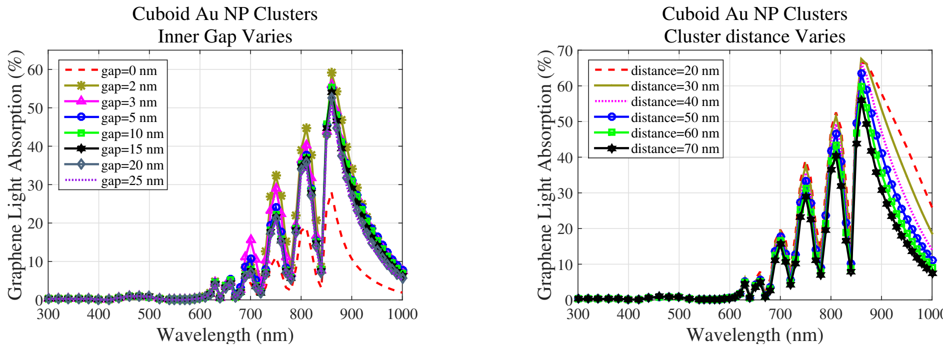

(a) (b)

FIGURE 4.5: Structure with Bragg reflector (a) cluster interval=70 nm, inner gap varies; (b) inner gap=3 nm, cluster interval varies.

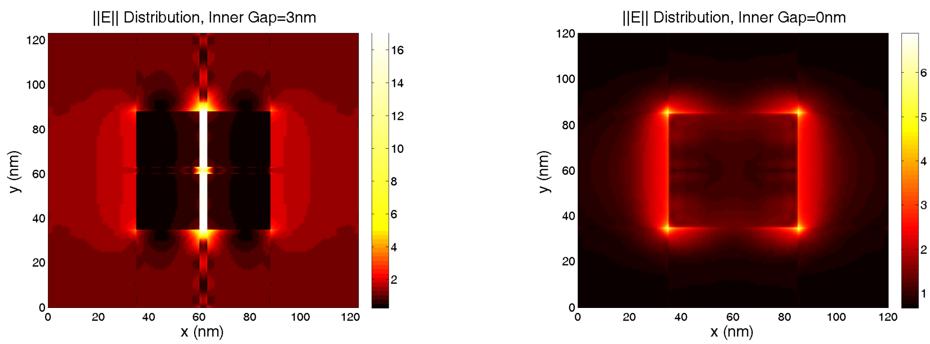

(a) (b)

FIGURE 4.6: Under 870nm TM_y normal incidence, electric field distribution for (a) inner gap=3 nm; (b) inner gap=0 nm.

cuboid Au NP clusters is chosen as 30 nm, and the inner gap is chosen as 2 nm. Despite the proposed structure's performance shows a strong correlation with the incident angle, it has a relatively large tolerance to the incident offset. Within the incident angle of -40 degree to +40 degree, a significant light absorption enhancement is observed in the graphene layer.

Both the gap inside each NP cluster and the interval between adjacent NP clusters are able to, and in fact are designed to, control the inter-particle electromagnetic coupling strength. Conventionally, the noble metal NPs are placed in a uniform pattern. However, even though this strategy is capable of achieving a strong surface plasmon resonance, the conflict of inter-particle coupling enhancement and effective plasmon surface area optimization always exists. Achieving a strong inter-particle electromagnetic coupling usually requires a close spatial interval between adjacent NPs; on the other hand, over-intensive metal coverages of the graphene inevitably weaken the utilization efficiency of plasmon resonance. In this section, we numerically study the strategy of split-NP clusters with SEBI. By keeping the percentage of gold-covered area unchanged, the contribution of the inner gap of each NP cluster is first studied. As a comparison, for a fixed inner gap value, the influence of distance between adjacent NP clusters is further systemically investigated.

Figure 4.5a shows the influence of the inner gap of each NP cluster, where the distance between adjacent clusters is supposed to be 70 nm. In Fig. 4.5b, we focus on the influence of the gap between adjacent clusters, where the gap in each cluster is typically chosen as 3 nm. Numerical results show that the split-NP cluster structure enhances the strength of the plasmonic phenomenon, and boost the maximum graphene absorption by 110% compared with the uniform NP array. As a typical instance, here the electric field distribution on the interface between graphene and the Au NPs are compared in Fig. 4.6 between conventional NP arrays and cluster NP arrays. It can be seen inside the gap, the electromagnetic near field distributes with more uniformly enhancement, which improves the plasmonic light concentration with higher energy efficiency. On the contrary, for non-split Au NP model (gap=0 nm), the near electric field mainly concentrates on the 4 singular corners, which not only produces unnecessary energy losses, but also generates a less efficient plasmon resonance.

The numerical study shows that the combination of NP cluster arrays and the Bragg reflector is able to boost the light absorption of graphene in the visible spectra and near infrared spectra. Compared with the conventional non-split NP arrays, an essentially stronger surface plasmon resonance are excited inside the gap of each

NP cluster, while the energy loss caused by NPs sharp corners are reduced to some degree. Due to this improved NP structure and well matched plasmon resonance frequency and intrinsic interferometirc peak, a peak absorption rate of 67.54% is observed at the wavelength 860 nm. This strong light absorption is achieved by choosing the gap inside each NP cluster as 3 nm, while separating adjacent clusters by 30 nm.

4.3.4 Cylindrical and ring NP with/ without Bragg reflector

Cylindrical and ring noble metal NPs are widely used in nano-scale photonic structures to generate effective resonances. The rectangular corners of cuboid metal NPs may become a drawback for nano-devices under certain circumstances. It is well known that these sharp corners can be singular points for electromagnetic fields and undesirably confine a large portion of energy, while at the same time negatively affect the surface plasmon resonance with the accompanying energy losses. With these concerns, it is reasonable to expect that the undesired power loss caused by the geometry can be reduced by removing the sharp corners of the cuboid Au NPs. In addition, since the strong near field in graphene is highly concentrated surrounding the bottom edges of gold NPs, appropriate improvement of the interface between gold NPs and graphene serves as an alternative strategy for each NP's plasmonic efficiency enhancement. In this section, we theoretically study the graphene light absorption contribution of a set of cylindrical and ring category Au NPs sketched in Fig. 4.2c - 4.2d. Without loss of generality, for all the ring NP models, the inner radius is typically chosen as half of its outer radius.

We first study the influence of solid cylindrical NPs with varying diameters and adjacent distance. Compared with the uniform metal NP pattern, this design does not explicitly improve the inter-particle coupling strength, but reduces the unnecessary energy loss and improves the plasmon resonance efficiency by removing the four

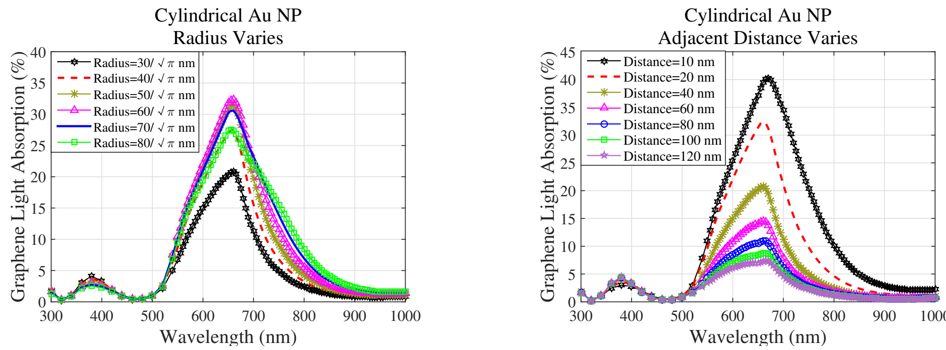

(a) (b)

FIGURE 4.7: Cylindrical NP with classic SiO_2 reflector (a) adjacent distance=40 nm, radius varies; (b) radius=$30/\sqrt{\pi}$ nm, adjacent distance varies.

singular corners. Next, to further boost the plasmonic efficiency of each noble metal NP, we consider a set of ring gold NPs for LSPR manipulation.

In previous studies, graphene's optimal light absorption in the visible spectrum is reported as 30.3% with classic silica reflector and cuboid NPs [Zhu et al. (2013a)]. Here we first investigate the performance of ring and cylindrical with the SiO_2 reflector. Referring to previous research reported by Zhu et al. [Zhu et al. (2013a)], a typically optimal thickness of 300 nm is chosen for the SiO_2 reflector. In order to make this structure comparable with the cuboid gold NP case, here the height of each NP is designed identical to that of the cuboid NP cluster. Similarly, we first try to find an appropriate diameter of the gold NP. Then, with this design of gold NP obtained, different distances between adjacent NPs are simulated. By varying the distance between adjacent cylindrical NPs, the inter-particle coupling strength can be controlled in a predicable way.

Numerical results in Fig. 4.7 - 4.8 show that even with classic silica reflectors, a peak graphene light absorption can be achieve as 41% by the ring NP structure at the incident wavelength of 690 nm. With this improvement on metal NP design, the optimal graphene absorption rate is over 35% higher than the maximum value reported by Zhu et al. [Zhu et al. (2013a)], where cuboid Au NPs are systemati-

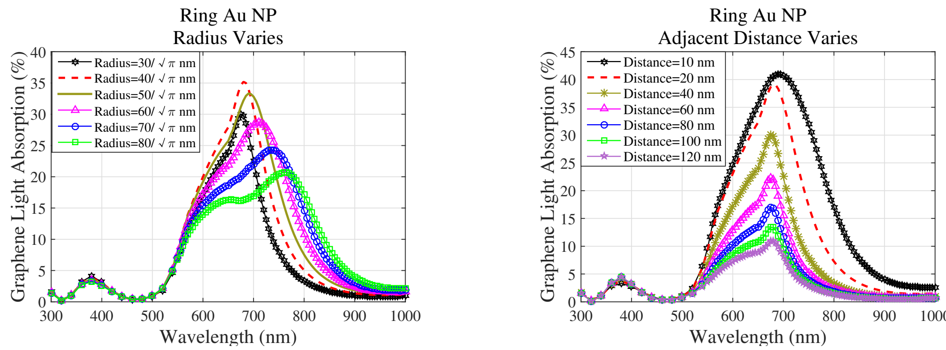

(a) (b)

FIGURE 4.8: Ring NP with classic SiO_2 reflector (a) adjacent distance=40 nm, radius varies; (b) radius= $30/\sqrt{\pi}$ nm, adjacent distance varies.

cally studied. Compared with cylindrical NPs, ring-NP-based models show a better frequency selectivity manipulation and a slightly higher graphene absorption. Moreover, by comparing Fig. 4.7b and 4.8b, the ring NP structure also shows a stronger and more sensitive inter-particle coupling, whose strength can be sharply tunned by changing the distance between adjacent gold NPs.

In general, by changing the outer radius of the ring NP, we can significantly change the local resonant frequency and consequently manipulate frequency selective absorption curve of graphene layer. Meanwhile, when varying the distance between adjacent NPs, the coupling strength of NPs are effectively controlled. This property can serve as a strategy to tune the strength of graphenes absorption without severely affecting the optimal absorption frequency.

As a comparable case with the cuboid cluster Au NP models, the same Bragg reflector design is built into the model for further graphene absorption enhancement. Fig. 4.9 - 4.10 provide the SEBI results for the cylindrical NP models and the ring NP models, respectively. Similar to the cuboid cluster NP case, the absorption of graphene can be enhanced dramatically in the simulated spectra. For cylindrical Au NPs, a peak graphene light absorption of 58.64% is observed under 860 nm incidence, while a peak graphene light absorption of 40.27% is observed under 850 nm incidence

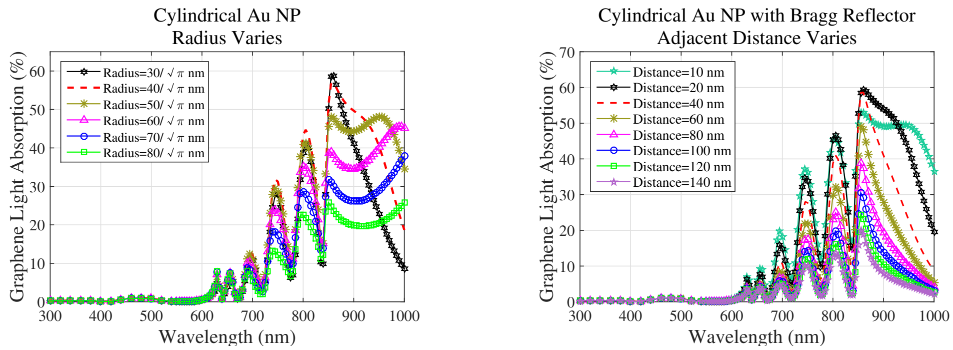

(a) (b)

FIGURE 4.9: Cylindrical NP with Bragg reflector (a) adjacent distance=40 nm, radius varies; (b) radius=$30/\sqrt{\pi}$ nm, distance between adjacent NPs varies.

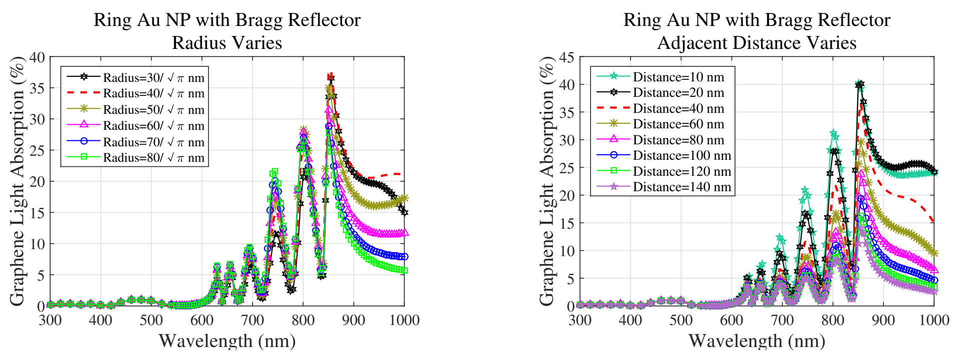

(a) (b)

FIGURE 4.10: Ring NP with Bragg reflector (a) distance=40 nm, radius varies; (b) radius=$30/\sqrt{\pi}$ nm, distance between adjacent NPs varies.

for ring Au NPs.

4.4 A Summary of Graphene's Plasmonic Engineering

In this work, the SEBI, which combines the boundary integral equations with the spectral element method, is utilized for numerical study of the light absorption of graphene. Benefiting from the spectral accuracy of the SEM and the efficiency of the surface integral equations used to truncate the open boundary, the proposed hybrid numerical technique shows excellent efficiency and accuracy.

Based on SEBI, the periodic cuboid Au NP clusters as well as the cylindrical/

ring clusters of Au NP are studied as the nano antenna for graphene light absorption engineering. Numerical results confirm that these designs are able to essentially boost the light absorption of graphene with a frequency selective property. To further enhance the plasmon resonance strength, a Bragg reflector is also designed for the proposed structures, which dramatically assists the enhancement and tuning of graphene light absorption.

Through plasmonic near-field engineering by controlling the type of reflector, the pitch and category of plasmonic antenna, the light absorption of graphene can be efficiently manipulated. A peak graphene light absorption rate of 41% is reported in the visible spectra, while 67.54% is reported in the whole spectra studied in this work.

5

The SEBI in Nonlinear Optics: Graphene's Third Harmonic Generation Engineering

5.1 Third Harmonic Generation of Graphene

In Chaper 4, a strategy of graphene's light absorption enhancement is systematically discussed. In this chapter, we employ the same strategy to stimulate strong LSPR, but extend the investigation into nonlinear optics. On one hand, the LSPR can largely improve graphene's photo-responsivity by confining a significant amount incident power around the graphene layer. Conversely, the strong near field is also expected to largely boost graphene's bulk nonlinear optical field generation. The nonlinear solver proposed in Chapter 2.4 serves as a general solution for the higher harmonic generation process. Section 5.2 further formulates the numerical method for the third harmonic generation (THG) problem. This third harmonic SEBI solver serves as the essential foundation for the efficient modeling, and the quantitative analysis of Kerr effects.

As a crucial property, graphene's nonlinear optical performance is an emerging topic in theoretical and experimental studies. Recent investigations show that the single-atom layer graphene's nonlinear optical response is particularly strong [Hong et al. (2013); Kumar et al. (2013); Hendry et al. (2010)], though its one-atom thickness requires further techniques to boost the relatively weak bulk nonlinear response. Due to its centrosymmetric structure, the ideal floating monolayer graphene forbids the second harmonic generation (SHG). Even though in practical designs this symmetric property may be broken by its adjacent materials, the induced SHG optical field is still expected to be weak. On the contrary, originated from the resonant nature of the light-graphene interaction, the third order nonlinear optical effects in graphene are remarkably strong [Mikhailov (2011); Vincenti et al. (2014)]. Previous four wave mixing experiment shows that graphene's effective third order susceptibility is on the order of $|\chi^{(3)}| \sim 10^{-15} m^2/V^2$ [Hendry et al. (2010); Kumar et al. (2013)]. This strong third order optical interaction generates a third harmonic signal with a significant contrast between graphene and the background material in most optoelectronic designs. Under the effect of strong LSPR, graphene's THG interaction analysis becomes even more interesting and meaningful.

Current studies in graphene's nonlinear performance are mainly based on experimental measurements and analytical studies [Hendry et al. (2010); Kumar et al. (2013); Mikhailov (2014)]. For relatively simple structures, such as a floating monolayer graphene or graphene deposed on flat substrate, these approaches are able to effectively analyze the nonlinear optical performance of graphene, and contribute to the determination of graphene's nonlinear material parameters. However, for more practical designs with more complex physics processes, theoretical analysis is not able to serve as an effective approach due to the model's complexity, while experiments usually require high costs. In addition, for most quantitative analyses of graphene's nonlinear performance, the nonlinear field is directly calculated from the field distribution at the fundamental frequency field without consideration of the Kerr effect. However, in many nonlinear optical applications, the magnitude of local optical field can be considerably large, thus renders the dielectric polarizations not negligible. Improper handling of the relation between materials' refractive pattern and the external electric field may finally jeopardize the reliability of the conclusions.

In this project, a self-consistent numerical solver is proposed for THG analysis. Based on the spectral element boundary integral (SEBI) method, the optical field at fundamental frequency (FF) and third harmonic (TH) frequency are solved iteratively and self-consistently. SEBI shows spectral accuracy, i.e. the relatively error decreases exponentially with increasing the order of Gauss-Lobatto-Legendre (GLL) basis functions. With this fast convergence method, the proposed numerical scheme is able to solve the FF field and the TH field accurately with a relatively high convergence rate. Meanwhile, the flexibility of spectral element method also makes this scheme suitable for the simulation of complex optoelectronic designs. Under this numerical scheme, the materials' response to the external optical fields is self-consistently included in the analyses at both FF and TH frequencies.

In Section 5.2, the self-consistent numerical solver is explained in detail, which can serve as a general solver for THG problems. In Section 5.3, this numerical solver is utilized for graphene's optical/ electro-optic THG enhancement analysis under strong LSPR. As a typical example, a prototype of grpahene-based photodetector are studied within the incident spectra of 400 nm to 1000 nm. Compared with the TH emission of a floating graphene layer, numerical simulations shows that under strong LSPR in our designed structure, graphene's THG is enhanced by over 4.4×10^5 times.

5.2 Self-Consistent THG Computation

5.2.1 Field-source relations

Under the SEBI scheme, the frequency domain electromagnetic scattering problem is described by the following weak form equations [Niu et al. (2014)]:

$$\begin{aligned}
&\int_V [(\mu_r^{-1}\nabla \times \mathbf{\Phi}_i)^T \cdot (\nabla \times \mathbf{E}) - k_0^2 \cdot (\epsilon_r \mathbf{\Phi}_i)^T \cdot \mathbf{E}]dV \\
&\qquad -2jk_0 \int_S \mathbf{\Phi}_i^T \cdot [\mathcal{K}(\tilde{\mathbf{J}}_s) - \epsilon_r \cdot \mathcal{L}(\mathbf{M}_s)]dS' \\
&\qquad = 2jk_0 \int_S \mathbf{\Phi}_i^T \cdot (\hat{n} \times \bar{\mathbf{H}}^{inc})dS'
\end{aligned} \tag{5.1}$$

$$\begin{aligned}
&jk_0 \int_S \mathbf{\Phi}_i^T \cdot [\mu_r \mathcal{L}(\tilde{\mathbf{J}}_s) + \frac{1}{2}\hat{n} \times \mathbf{E} + \mathcal{K}(\mathbf{M}_s)]dS' \\
&\qquad = jk_0 \int_S \mathbf{\Phi}_i^T \cdot (\hat{n} \times \mathbf{E}^{inc})dS'
\end{aligned} \tag{5.2}$$

where the operator $\mathcal{K}$ and $\mathcal{L}$ are defined in reference [Niu et al. (2014)].

After obtaining the linear equation discretized from Eq. 5.1-5.2, the block-Thomas method is used to accelerate the solving process. Conventionally, the block-Thomas method is designed for block tridiagonal linear systems. However, according to the properties of the linear equation derived from Eq. 5.1-5.2, the block-Thomas method can be used level by level for partial acceleration [Luo et al. (2013)]. For more detailed algorithm of SEBI as well as the partial acceleration of block-Thomas method, readers are referred to the references [Luo et al. (2013); Chen et al. (2011a)] and the references therein.

5.2.2 Full-wave solver for third harmonic generation

The optical source-field relation at both FF and TH frequency can be sufficiently described by vector wave equations, where the dielectric polarization serves as a secondary source for the fields at both frequencies. As a direct application, Eq. 5.1-

5.2 can be used to solve the optical fields at FF and TH frequency with self-consistent coupling. Conventionally, due to the difficulty in solving the nonlinear vector partial differential equation, the nonlinear optical analyzes usually ignore the influence of the mutual coupling between FF field and TH field. For instance, by ignoring the coupling between the FF field and TH field, one can only solve for the FF field without nonlinear dielectric polarization, and then apply $\chi^{(3)}$ to FF field to obtain the TH field pattern. However, this approach is not accurate in general. Although the solution can be largely simplified for many engineering background, with the increase of the field intensity, the error becomes more and more unacceptable. For the same reason, the analysis of nano-structure's THG performance under strong LSPR renders a particular need for a self-consistent numerical solver.

Here we focus on accurately solving the nonlinear optical field directly from the coupled vector wave equations. To achieve this goal, we need to update the FF field, nonlinear dielectric polarization, and the TH field iteratively. As is well known, the dielectric polarization serves as a source for nonlinear optical fields. In the proposed numerical scheme, we initially calculate the FF field induced by the incident light via the linear process. With this obtained FF field, the initial value of the TH dielectric polarization is first calculated, from which the initial value of the TH field can be solved from the vector wave equation. After all these initial values obtained, we can iteratively solve for the field unknowns at FF and TH frequency to arrive at the self-consistent solution.

Written as a block matrix equation, the FF and TH fields in Eq. 5.1-5.2 can be described as

$$\begin{bmatrix} K_{II}(k_0) & K_{IS}(k_0) & 0 \\ K_{SI}(k_0) & K_{SS}(k_0)+U^M(k_0) & V^M(k_0) \\ 0 & V^E(k_0) & U^E(k_0) \end{bmatrix} \cdot \begin{bmatrix} \mathbf{E}_I(k_0) \\ \mathbf{E}_S(k_0) \\ \mathbf{H}_S(k_0) \end{bmatrix} = \begin{bmatrix} \mathbf{P}^{THG}(k_0) \\ \mathbf{H}^{inc} \\ \mathbf{E}^{inc} \end{bmatrix} \tag{5.3}$$

$$\begin{bmatrix} K_{II}(3k_0) & K_{IS}(3k_0) & 0 \\ K_{SI}(3k_0) & K_{SS}(3k_0)+U^M(3k_0) & V^M(3k_0) \\ 0 & V^E(3k_0) & U^E(3k_0) \end{bmatrix} \cdot \begin{bmatrix} \mathbf{E}_I(3k_0) \\ \mathbf{E}_S(3k_0) \\ \mathbf{H}_S(3k_0) \end{bmatrix} = \begin{bmatrix} \mathbf{P}^{THG}(3k_0) \\ \mathbf{0} \\ \mathbf{0} \end{bmatrix} \tag{5.4}$$

Here we use $\mathbf{P}(k_0)$ and $\mathbf{P}(3k_0)$ to denote the nonlinear dielectric polarization for the FF and TH fields, respectively:

$$\begin{aligned} \mathbf{P}(k_0) = 3\epsilon_0\chi^{(3)}(k_0) &: \mathbf{E}(3k_0)\mathbf{E}(-k_0)\mathbf{E}(-k_0) \\ +3\epsilon_0\chi^{(3)}(k_0) &: \mathbf{E}(k_0)\mathbf{E}(k_0)\mathbf{E}(-k_0) \\ +3\epsilon_0\chi^{(3)}(k_0) &: \mathbf{E}(k_0)\mathbf{E}(0)\mathbf{E}(0) \end{aligned} \tag{5.5}$$

and

$$\mathbf{P}(3k_0) = \epsilon_0\chi^{(3)}(3k_0) : \mathbf{E}(k_0)\mathbf{E}(k_0)\mathbf{E}(k_0) \tag{5.6}$$

where $\chi^{(3)}$ is a rank-4 tensor instead of a scalar to guarantee the robustness under oblique incidence and for anisotropic media. After applying the procedure of Galerkin's method, the source terms in Eq. 5.3–5.4 are obtained as

$$\mathbf{P}_i^{THG}(k_0) = \frac{1}{\epsilon_0}\int_\Omega dV \mathbf{\Phi}_i \cdot \mathbf{P}(k_0) \tag{5.7}$$

and

$$\mathbf{P}_i^{THG}(3k_0) = \frac{1}{\epsilon_0}\int_\Omega dV \mathbf{\Phi}_i \cdot \mathbf{P}(3k_0) \tag{5.8}$$

where $\mathbf{\Phi}_i$ denotes the corresponding GLL basis function. The sub-matrices in Eq. 5.3 – 5.4 are given by the reference of Luo et. al. [Luo (2013)]

In order to quantitatively analyze graphene's THG behavior within given samples, the backward and forward TH exiting power rate are calculated at the top and bottom truncation boundaries.

$$R_{bwd/fwd} = \frac{\int_{top/bottom} dS(\pm\hat{z}) \cdot Re\{\frac{1}{2}\mathbf{E} \times \mathbf{H}^*\}}{\int_{top} dS(-\hat{z}) \cdot Re\{\frac{1}{2}\mathbf{E}^{inc} \times \mathbf{H}^{inc*}\}} \tag{5.9}$$

It is also important to notice that the solver is valid under the condition that the power series expression of nonlinear dielectric polarization is valid. It is important to keep this in mind because, when the incident optical power is particularly strong, the induced secondary source may be even larger than the primary source, which finally leads to an incorrect result. This limitation is purely caused by the physical description instead of the numerical solver.

5.3 Graphene's THG under strong LSPR

LSPRs are widely used in nano-scale optoelectronic designs for performance enhancement and tight packing. As a typical example, previous research demonstrates that with appropriate inter-particle coupling and light concentration by LSPRs, graphene's light absorption can be dramatically enhanced with frequency selectivity, which makes the design of graphene-based photodetector realistic [Zhu et al. (2013a); Niu et al. (2015)].

Under this engineering background, we extend our study to graphene's THG optical performance enhancement under the strategy of engineering strong LSPR. Similar to the application of LSPR in graphene's linear performance enhancement, under proper design, a strong optical field can be concentrated around the graphene layer, which in turn generates a strong secondary source for both TH and FF fields.

It is also important notice that, LSPR not only may serve as an effective tool for graphene's THG enhancement, but also is a typical example for the necessity of a full-wave numerical solver. During the THG process, the incident laser beam usually exhibits a particular large magnitude to guarantee a satisfying TH field generation. In the meantime, an satisfying LSPR can further boost the FF field's magnitude around graphene by over one order. So it should not be surprising that the nonlinear dielectric polarization is relatively strong at both FF and TH frequency even without applying external static electric field. Moreover, the LSPR stimulation heavily relies on the scattering characteristics of the nano-structure, and signifiant change to the field pattern may also impact the performance of THG. As a result, for this category of simulation, neglecting the influence of Kerr effect may induce a relatively large numerical error.

5.3.1 Solver validation

As the first numerical example, a comparison between the numerical results and the experimental data from the reference [Kumar et al. (2013)] is provided in Fig. 5.1. In this experiment, reported by Kumar et al. [Kumar et al. (2013)], a three-layer sample is made with flat monolayer graphene, silicon dioxide layer (300 nm), and Si substrate (500 μm), and $\chi^{(3)}$ is taken as a scalar. To be fully comparable with the experimental conditions and settings, when simulating this model, $\chi^{(3)}$ is set to be an isotropic tensor in our code for this example. In addition, we must emphasize here that, graphene's $|\chi^{(3)}|$ measured from this experiment is believed to have not been corrected for the multiple reflections caused by the three layers. Although its influence might be within the experimental uncertainty, this difference may cause non-negligible effects in self-consistent simulation. Theoretically, if the multi-reflection is not taken into consideration when calculating $|\chi^{(3)}|$ from the measured experimental data, then graphene's light absorption rate should be the same

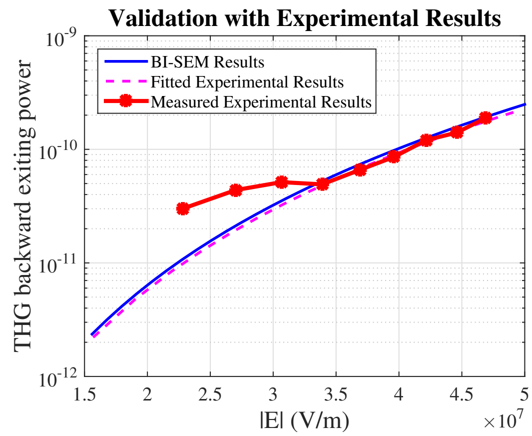

FIGURE 5.1: Comparison between SEBI results and experimental data for a graphene- SiO_2-Si setup.

as that of floating layer. However, the SEBI simulation of the experimental model shows that graphene's light absorption in this three-layer setting is almost twice of that in a floating graphene layer. Therefore, to account for the influence caused by multiple reflections, in our nonlinear simulation $|\chi^{(3)}|$ is take as 1/8 of the value extracted in the experiment, i.e. $|\chi^{(3)}| = 5 \times 10^{-18} m^2/V$.

In Fig. 5.1, the red marked line is the measured experimental data, and the pink dash line is the fitted results reported by the reference [Kumar et al. (2013)]. We can see that with the correction of $|\chi^{(3)}|$, the numerical results match very well with both the measured data and the fitted experimental results in general. Within the low incident power range, the numerical results differ more significantly with the measured experimental data. However, this difference is more likely to be caused by the measuring error due to the low radiation energy. In the meantime, the measured data also deviates from the fitted cubic-polynomial curve significantly in the low incident power section, which in turn corresponds to our analyses.

5.3.2 Graphene's THG enhancement with LSPR

Figure 5.2 gives a schematic drawing of a graphene-based photodetector prototype [Niu et al. (2015)]. From top to bottom this model consists of the following sections:

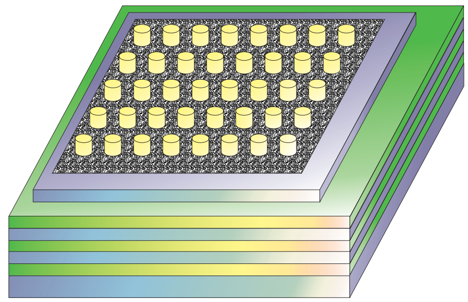

FIGURE 5.2: Sketch of the graphene-based photodetector prototype.

periodic cylindrical gold NPs, monolayer graphene, SiO_2/Si Bragg reflector, and Si substrate. The radius of each cylindrical NP is chosen as 16.93 nm, while the distance between adjacent NPs confers as 40 nm. The reference [Niu et al. (2015)] provides detailed explanation for the structure design as well as graphene's linear performance analyses. Our previous study validates that under this design, a particular strong LSPR can be engineered around graphene layer, which enhances graphene's linear optical absorption by over 30 times.

Because of the strong LSPR, a particularly strong optical field is engineered to concentrate around the interface between graphene and NPs. Aside from the expected enhancement to the THG, this strong field may also induce not negligible optical Kerr effect. As a typical example, numerical studies are provided for the model of Fig. 5.2 with full-wave solver, as well as that from neglecting Kerr effect.

Figure 5.3 provides several typical results for the influence of optical Kerr effect, where the simulation parameters are kept consistent with the systematic simulation in latter part of this section. For regular cases such as the flat floating graphene's THG, the corresponding nonlinear dielectric polarization is really weak. Thus neglecting the optical Kerr effect's contribution does not induce significant error in final result. On the contrary, for the model with strong LSPR, the dielectric polarization around graphene is enhanced by orders. As a result, it is not surprising that a full-wave solver is of significant value in this situation. The numerical results show that the

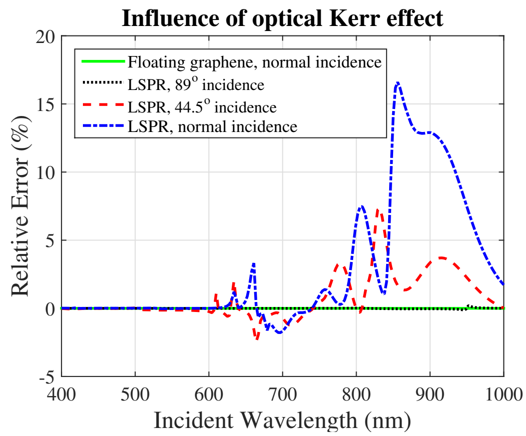

FIGURE 5.3: Influence of optical Kerr effect.

relative error caused by conventional approximation can easily reach to 17%, which largely impairs the robustness of any further theoretical discussions.

Based on the self-consistent solver proposed in Section 5.2, the backward and forward THG emission power rate of graphene is shown in Fig. 5.4-5.5. In our simulation, the incident electric field component magnitude is taken as $|\mathbf{E}^{inc}| = 10^6$ V/m. This is equivalent to an incident Gaussian beam with a peak average intensity of 1.3263×10^5 W/cm^2, which is reasonable in laboratory environments. In addition, different from the numerical results in Fig. 5.1, in all following numerical simulations, graphene's third order susceptibility is taken as an anisotropic rank-4 tensor, with the non-zero entries $\chi^{(3)}_{1111}$, $\chi^{(3)}_{2222}$, $\chi^{(3)}_{3333}$, $\chi^{(3)}_{1133}$, $\chi^{(3)}_{1313}$, $\chi^{(3)}_{1331}$, $\chi^{(3)}_{3131}$, $\chi^{(3)}_{3113}$, $\chi^{(3)}_{1122}$, $\chi^{(3)}_{2211}$, $\chi^{(3)}_{1212}$, $\chi^{(3)}_{1221}$ [Hong et al. (2013)]. Here the value of these components are assigned based on previous four-wave mixing experiment [Hendry et al. (2010); Kumar et al. (2013)]: $\chi^{(3)}_{1122} = \chi^{(3)}_{2211} = \chi^{(3)}_{1212} = \chi^{(3)}_{1221} = 2.3 \times 10^{-16} m^2/V$ and the rest non-zero components equal to $7 \times 10^{-16} m^2/V$. This anisotropic tensor setting is to guarantee the accuracy of the simulation results with an oblique incidence. Moreover, although the flexibility of the proposed method allows the simulation of multiple nonlinear materials within the structure, here only graphene's third order susceptibility is taken into consideration. The first reason for this simulation set-up is that the

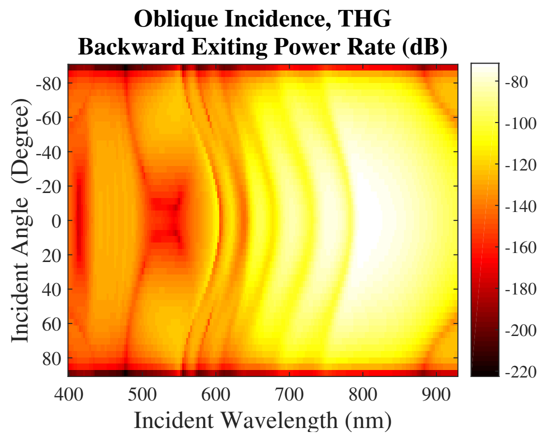

FIGURE 5.4: Graphene's backward THG emission.

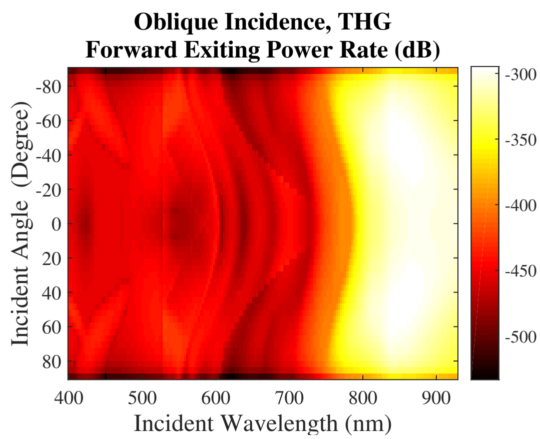

FIGURE 5.5: Graphene's forward THG emission

primary goal is to study the THG of graphene, thus making gold's THG emission marginal. In addition, previous study reports Au's third order susceptibility as $\chi^{(3)} = 7.6 \times 10^{-19} m^2/V^2$ [Sámson et al. (2011)], which is orders smaller than that of graphene. As a direct result, the THG strength of gold is also significantly weaker than graphene.

Due to the strong LSPR and the Bragg reflector in the structure, graphene's radiation TH power rate shows an effective frequency selectivity and a strong correlation between the incident angles under fixed incident wavelengths. Compared with the floating single layer graphene, the backward THG emission is largely enhanced while

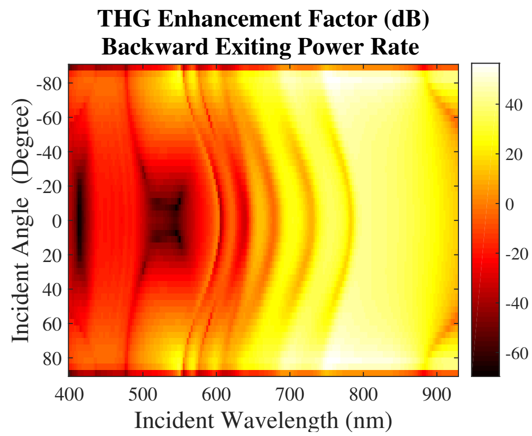

FIGURE 5.6: Graphene's backward THG enhancement factor.

the forward THG emission is reduced by orders of magnitude due to the multi-layer reflector. In most experimental conditions and optoelectronic devices, focusing the emission power in one direction may largely simplify the energy collection, and reduce the lossy influence of the thick-bulk substrate. Fig. 5.4 show that the maximum backward radiation power rate is at -71.4 dB. Moreover, according to our simulation, the forward THG power rate value for the spectra of 300 nm to 457 nm is too small to be calculated precisely with double precision. In other words, the forward THG should be considered as trivial compared the backward emission in that spectra.

A comparison between monolayer graphene's THG under such strong LSPR and that of the floating graphene layer is provided in Fig. 5.6. The enhancement factor is calculated as the ratio between the TH exiting power rates under each structure, and the results are plotted as its log value. Numerical simulation shows that under efficient LSPR engineering, graphene's backward THG radiation is enhanced by over 4.4×10^5 times. This maximum enhancement factor is achieved at 81.6^o and 877 nm incidence.

Electro-opto Kerr effect is another typical phenomenon that the external electric field can perturbate the effective refractive index of the medium. Based on above discussion about the LSPR strategy for THG enhancement, it is also straight forward

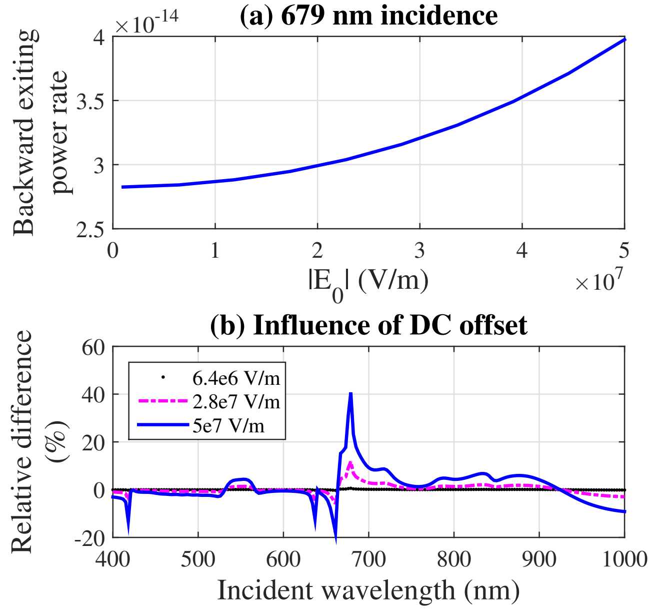

FIGURE 5.7: Graphene's backward THG under DC offset.

to extend the proposed numerical solver for the study of electro-opto Kerr effect's influence. With a static electric field applied to the graphene layer, the corresponding dielectric polarization induces a perturbation in both the material's effective third order susceptibility, and the scattering pattern of the overall nano-structure. Those two factors work together to influence the backward TH emission.

In numerical simulation, a DC external voltage off-set is also applied to the graphene layer additionally to the incident source described in above section. Without loss generality, a systematic numerical simulation is conducted for the induced external electric field (+y direction), whose the magnitude varies from 1×10^6 V/m to 5×10^7 V/m. Notice that the power series expression is not valid for saturated materials, a even larger DC magnitude may risk influencing the robustness of the numerical results, nor is such an ultra-strong DC offset quite realistic in experiments.

Figure 5.7-(a) provides the influence of DC offset to backward TH emission power rate under 679 nm incidence. As expected, when the magnitude of applied static

electric field is relatively small, the impact of the electro-opto process is weak. With the increase of the static field's magnitude, an increasingly strong TH backward emission is observed. In Fig. 5.7-(b), a more complete comparison is provided for three typical DC offset set-up. Here the reference data is taken as the results obtained in Fig. 5.4 with normal incidence. A positive relative difference physically means an enhanced TH backward emission, while a negative value denotes an impaired emission pattern at certain spectra. The results show that at relatively weak static field environment, the applied DC field does not exhibits a observable influence. However, for strong static electric field, a highly frequency sensitive perturbation is observed. Under 679 nm incidence, the backward emission is enhanced by 40 %. With relatively strong electro-opto Kerr effect, the backward TH emission can also be impaired at certain spectra due to the induced change in the structure's scattering characters. It should also be noticed that, although the electro-opto Kerr effect can contribute to THG's intensity and frequency tuning, its impact is only secondary compared with that of LSPR.

Multilayer stack is another form of graphene used within some engineering applications. Under normal incidence of the same light source, bilayer and trilayer graphene's backward THG emission is further simulated in Fig. 5.8. The numerical simulation of bilayer and trilayer graphene is modeled analogy from the monolayer case, i.e., with similar electric properties but different in thickness. Within the incident spectra of 400 nm to 700 nm, the LSPR of the structure is not particularly strong [Niu et al. (2015)]. As a result, the THG efficiency increases with the increase of graphene's thickness, due to the improved utilization of the concentrated optical field around the interface between gold NPs and graphene. However, when entering the strong LSPR region, the optical field is tightly concentrated around the upper interface of graphene. Under this circumstance, increasing the thickness does not contribute to further enhancement of THG. On the contrary, the lossy property of

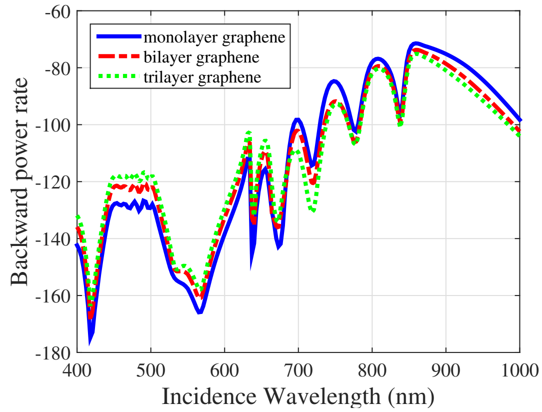

FIGURE 5.8: Few-layer graphene's backward THG emission.

graphene as well as the changed multi-layer reflection pattern in fact weaken the backward THG emission to some degree.

5.4 Conclusions

In this chapter, graphene's THG enhancement with strong LSPRs is theoretically investigated by using the self-consistent solver based on SEBI. The fast convergent SEBI is extended to an iterative THG solver with high accuracy and efficiency. This proposed numerical simulation technique directly starts from the coupled vector wave equations for FF and TH fields. By iteratively updating the secondary source from nonlinear coupling, the influence of optical/ electro-opto Kerr effect can be accurately included in numerical analyses. Under this numerical scheme, the anisotropic property of graphene's third order susceptibility is fully taken into consideration to guarantee the accuracy under an oblique incidence. The numerical method is validated by comparing the numerical results with experimental data. In addition, the THG backward and forward exiting power of a graphene-based photodetector prototype is calcuated. Under strong LSPR, numerical simulation shows that monolayer graphene's THG is enhanced by over 4.4×10^5 times. Simultaneously utilizing the electro-optic Kerr can further boost the TH emission. However, compared with the effect of LSPR, this contribution is only secondary, and is not expected to enhance THG by orders. In the last section, this study is also extended to the investigation of bilayer and trilayer graphene's THG performance under strong LSPR.

6

Periodic Layered Medium Dyadic Green's Function

6.1 Overview

This chapter provides a systematic description of the periodic layered medium dyadic Green's function (PLMGF) under wave function formulation, and the singularity extraction technique under the matrix-friendly formulation. Before continuing to further investigation on the implementation of the PLMGF within certain integral equation context, here the discussion primarily focuses on the systematic definition, matrix-friendly formulation and efficient computation of the PLMGF itself. Based on this foundation, Chapter 7 - 8 combine the SEBI with PLMGF together for multiscale optical simulation. The efficient implementation of the PLMGF within SEBI will be discussed systematically therein.

6.2 Wave Function Formulation of the PLMGF

The periodic layered medium dyadic Green's function describes the electric and magnetic field generated by the periodic array of point electric and magnetic dipole sources in a layered medium background. In general, we can define four dyadic

Green's functions: $\bar{\mathbf{G}}_{P,e}(\mathbf{r},\mathbf{r}')$, $\nabla\times\bar{\mathbf{G}}_{P,e}(\mathbf{r},\mathbf{r}')$, $\bar{\mathbf{G}}_{P,m}(\mathbf{r},\mathbf{r}')$ and $\nabla\times\bar{\mathbf{G}}_{P,m}(\mathbf{r},\mathbf{r}')$, there the subscript P denotes field response created by periodic sources within plane wave background. Among them, $\bar{\mathbf{G}}_{P,e}(\mathbf{r},\mathbf{r}')$, $\nabla\times\bar{\mathbf{G}}_{P,e}(\mathbf{r},\mathbf{r}')$ are the electric field and magnetic field response created by an electric dipole array, respectively. $\bar{\mathbf{G}}_{P,m}(\mathbf{r},\mathbf{r}')$ and $\nabla\times\bar{\mathbf{G}}_{P,m}(\mathbf{r},\mathbf{r}')$ corresponds to those generated by a magnetic dipole array.

The periodic Green's function can be derived as a direct result of the Floquet theorem and the periodicity of the sources. Before introducing the detailed expression for the PLMGF, we start from that of the non-periodic layered medium Green's function (LMGF). In the past decades, various formulations have been derived for the LMGF. Without loss of generality, the wave function formulation is adopted for the study and discussions throughout this work.

In general, the non-periodic LMGF consists of three components: (1) the direct term, which is the response directly contributed by the source without any reflection or transmission perturbation. (2) TE wave related secondary term, which is the response contributed by the TE wave components' reflection and transmission. (3) TM wave related secondary term, which is the response contributed by the TM wave components' reflection and transmission. The above can be expressed as

$$\bar{\mathbf{G}}_e(\mathbf{r},\mathbf{r}') = \bar{\mathbf{G}}_e^{pri}(\mathbf{r},\mathbf{r}') + \bar{\mathbf{G}}_e^{TE}(\mathbf{r},\mathbf{r}') + \frac{1}{k_{nm}^2}\bar{\mathbf{G}}_e^{TM}(\mathbf{r},\mathbf{r}') \tag{6.1}$$

where the subscript m and n are the layer indices of the source point and the observation point, respectively; $k_{nm}^2 = \omega^2\epsilon_n\mu_m$.

The secondary tensor components of $\bar{\mathbf{G}}_e(\mathbf{r},\mathbf{r}')$ can be expressed as

$$\bar{\mathbf{G}}_e^{pri}(\mathbf{r},\mathbf{r}') = (\bar{\mathbf{I}} + \frac{\nabla\nabla}{k_m^2})g(\mathbf{r},\mathbf{r}') \tag{6.2}$$

$$\bar{\mathbf{G}}_e^{TE}(\mathbf{r},\mathbf{r}') = (\nabla\times\hat{\mathbf{z}})(\nabla'\times\hat{\mathbf{z}})g^{TE}(\mathbf{r},\mathbf{r}') \tag{6.3}$$

$$\bar{\mathbf{G}}_e^{TM}(\mathbf{r},\mathbf{r}') = (\nabla\times\nabla\times\hat{\mathbf{z}})(\nabla'\times\nabla'\times\hat{\mathbf{z}})g^{TM}(\mathbf{r},\mathbf{r}'). \tag{6.4}$$

In the above expressions, we define $g(\mathbf{r},\mathbf{r}')$, $g^{TE}(\mathbf{r},\mathbf{r}')$ and $g^{TM}(\mathbf{r},\mathbf{r}')$ as

$$g(\mathbf{r},\mathbf{r}') = \frac{e^{ik_m|\mathbf{r}-\mathbf{r}'|}}{4\pi|\mathbf{r}-\mathbf{r}'|}, \tag{6.5}$$

$$g^{\alpha}(\mathbf{r},\mathbf{r}') = \frac{i}{2}\mathscr{F}^{-1}\{\frac{F^{\alpha}(k_s,z,z')}{k_{mz}k_s^2}\}, \quad \alpha = TE, TM \tag{6.6}$$

where $F^{\alpha}(k_s,z,z')$ is the propagation factor; $\mathbf{k}_s = \hat{\mathbf{x}}k_x + \hat{\mathbf{y}}k_y$; $k_{mz} = \sqrt{k_m^2 - k_\rho^2}$.

The $\bar{\mathbf{G}}_m(\mathbf{r},\mathbf{r}')$ can be obtained directly through the duality principle as

$$\bar{\mathbf{G}}_m(\mathbf{r},\mathbf{r}') = \bar{\mathbf{G}}_m^{pri}(\mathbf{r},\mathbf{r}') + \bar{\mathbf{G}}_m^{TM}(\mathbf{r},\mathbf{r}') + \frac{1}{k_{mn}^2}\bar{\mathbf{G}}_m^{TE}(\mathbf{r},\mathbf{r}') \tag{6.7}$$

where

$$\bar{\mathbf{G}}_m^{pri}(\mathbf{r},\mathbf{r}') = \bar{\mathbf{G}}_e^{pri}(\mathbf{r},\mathbf{r}'), \tag{6.8}$$

$$\bar{\mathbf{G}}_m^{TM}(\mathbf{r},\mathbf{r}') = (\nabla\times\hat{\mathbf{z}})(\nabla'\times\hat{\mathbf{z}})g^{TM}(\mathbf{r},\mathbf{r}'), \tag{6.9}$$

$$\bar{\mathbf{G}}_m^{TE}(\mathbf{r},\mathbf{r}') = (\nabla\times\nabla\times\hat{\mathbf{z}})(\nabla'\times\nabla'\times\hat{\mathbf{z}})g^{TE}(\mathbf{r},\mathbf{r}'). \tag{6.10}$$

The expression of the propagation factor $F^{\alpha}(k_s,z,z')$ can be summarized in three categories: source and observer are in the same layer ($m = n$); source is in the layer above the observer's layer ($m > n$); source is in the layer below the observer's layer ($m < n$). Figure 6.1 provides a sketch of the layered index definition for a general layered medium. Accordingly, the propagation factor's expressions for all three situations are given below [Chen et al. (2011b)].

$Case\ A : m = n$

$$F(z,z') = F_1(z,z') + f_{v2}(z)I_2(m)f_{r2}(z') + f_{v3}(z)I_3(m)f_{r3}(z') \tag{6.11}$$

where

$$F_1(z,z') = e^{-jk_{mz}|z-z'|} \tag{6.12}$$

$$f_{v2}(z) = e^{-jk_{mz}(d_{m+1}-z)} \tag{6.13}$$

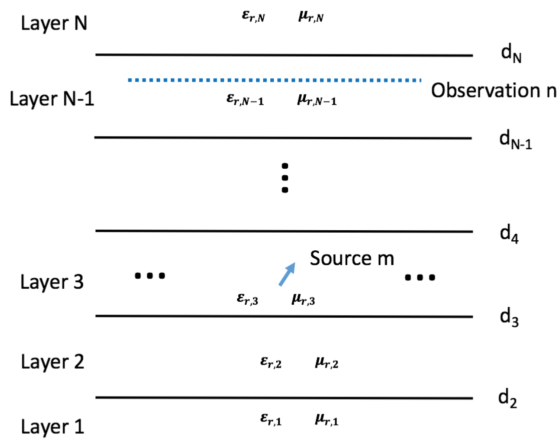

FIGURE 6.1: A sketch of the layered index definition for a general layered medium.

$$f_{v2}(z') = e^{-jk_{mz}(d_{m+1}-z')} + \tilde{R}_{m,m-1}e^{-jk_{mz}(d_{m+1}-2d_m+z')} \tag{6.14}$$

$$I_2(m) = \tilde{M}_m\tilde{R}_{m,m+1} \tag{6.15}$$

$$f_{v3}(z) = e^{-jk_{mz}(z-d_m)} \tag{6.16}$$

$$f_{r3}(z') = e^{-jk_{mz}(z'-d_m)} + \tilde{R}_{m,m+1}e^{-jk_{mz}(2d_{m+1}-d_m-z')} \tag{6.17}$$

$$I_3(m) = \tilde{M}_m\tilde{R}_{m,m-1}. \tag{6.18}$$

Case B $: m > n$

$$F(z,z') = f_v(z)\cdot I(m,n)\cdot f_r(z') \tag{6.19}$$

where

$$f_v(z) = e^{-jk_{nz}(d_{n+1}-z)} + \tilde{R}_{n,n-1}e^{-jk_{nz}(z+d_{n+1}-2d_n)} \tag{6.20}$$

$$f_r(z) = e^{-jk_{mz}(z'-d_m)} + \tilde{R}_{m,m+1}e^{-jk_{mz}(2d_{m+1}-d_m-z')} \tag{6.21}$$

$$I(m,n) = \tilde{M}_m\cdot\tilde{T}_{mn} \tag{6.22}$$

$$\tilde{R}_{i,i-1} = \frac{R_{i,i-1}+\tilde{R}_{i-1,i-2}e^{-jk_{i-1,z}(2d_i-2d_{i-1})}}{1+R_{i,i-1}\tilde{R}_{i-1,i-2}e^{-jk_{i-1,z}(2d_i-2d_{i-1})}} \tag{6.23}$$

$$\tilde{T}_{mn} = \prod_{j=n+1}^{m-1}[e^{-jk_{jz}(d_{j+1}-d_j)}S_{j+1,j}]S_{n+1,n} \tag{6.24}$$

$$S_{j+1,j} = \frac{T_{j+1,j}}{1 - R_{j,j+1}\tilde{R}_{j,j-1}e^{-jk_{jz}(2d_{j+1}-2d_j)}}. \tag{6.25}$$

Case $C : m < n$

$$F(z,z') = f_v(z) \cdot I(m,n) \cdot f_r(z') \tag{6.26}$$

where

$$f_v(z) = e^{-jk_{nz}(z-d_n)} + \tilde{R}_{n,n+1}e^{-jk_{nz}(2d_{n+1}-d_n-z)} \tag{6.27}$$

$$f_r(z') = e^{-jk_{mz}(d_{m+1}-z')} + \tilde{R}_{m,m-1}e^{-jk_{mz}(d_{m+1}-2d_m+z')} \tag{6.28}$$

$$I(m,n) = \tilde{M}_m \cdot \tilde{T}_{mn} \tag{6.29}$$

$$\tilde{R}_{i,i+1} = \frac{R_{i,i+1} + \tilde{R}_{i+1,i+2}e^{-jk_{i+1,z}(2d_{i+2}-2d_{i+1})}}{1 + R_{i,i+1}\tilde{R}_{i+1,i+2}e^{-jk_{i+1,z}(2d_{i+2}-2d_{i+1})}} \tag{6.30}$$

$$\tilde{T}_{mn} = \prod_{j=m+1}^{n-1} [e^{-jk_{jz}(d_{j+1}-d_j)}S_{j-1,j}]S_{n-1,n} \tag{6.31}$$

$$S_{j-1,j} = \frac{T_{j-1,j}}{1 - R_{j,j-1}\tilde{R}_{j,j+1}e^{-jk_{jz}(2d_{j+1}-2d_j)}}. \tag{6.32}$$

In all three cases, we have

$$\tilde{M}_m = [1 - \tilde{R}_{m,m-1}\tilde{R}_{m,m+1}e^{-2jk_{mz}(d_{m+1}-d_m)}]^{-1} \tag{6.33}$$

$$R_{ij} = \frac{p_j k_{iz} - p_i k_{jz}}{p_j k_{iz} + p_i k_{jz}} \tag{6.34}$$

$$p = \begin{cases} \mu, & TE \\ \epsilon, & TM \end{cases}. \tag{6.35}$$

Substituting Eq. (6.11) - (6.32) into Eq. (6.1) and (6.7), the four LMGF's, i.e., $\bar{\mathbf{G}}_{P,e}(\mathbf{r},\mathbf{r}')$, $\nabla \times \bar{\mathbf{G}}_{P,e}(\mathbf{r},\mathbf{r}')$, $\bar{\mathbf{G}}_{P,m}(\mathbf{r},\mathbf{r}')$ and $\nabla \times \bar{\mathbf{G}}_{P,m}(\mathbf{r},\mathbf{r}')$, can be calculated for each source - observation point pair. Noticing that the inverse Fourier transform or the Sommerfeld integral needs to be evaluated through this process, the overall computational cost is usually not trivial.

Based on the foundation of the non-periodic LMGF, the periodic Green's functions' formulations can be obtained through the Floquet theorem as

$$\bar{\mathbf{G}}_{P,\alpha}(\mathbf{r},\mathbf{r}') = \sum_{p=-\infty}^{+\infty}\sum_{q=-\infty}^{+\infty} \bar{\mathbf{G}}_{\alpha}(\mathbf{r},\mathbf{r}'_{pq})e^{jk_x^i p\cdot L_x}e^{jk_y^i q\cdot L_y}, \quad \alpha = e, m, \tag{6.36}$$

$$\nabla\times\bar{\mathbf{G}}_{P,\alpha}(\mathbf{r},\mathbf{r}') = \sum_{p=-\infty}^{+\infty}\sum_{q=-\infty}^{+\infty} \nabla\times\bar{\mathbf{G}}_{\alpha}(\mathbf{r},\mathbf{r}'_{pq})e^{jk_x^i p\cdot L_x}e^{jk_y^i q\cdot L_y}, \quad \alpha = e, m. \tag{6.37}$$

where L_x and L_y are the periods in x, y directions, respectively; $\mathbf{r}'_{pq} = \mathbf{r}' + (pL_x, qL_y, 0)^T$.

The key to obtain the numerical value of Eq. (6.36) - (6.37) for each source - observer pair includes the computation of the following series sum:

$$g_P(\mathbf{r},\mathbf{r}') = \sum_p\sum_q g(\mathbf{r},\mathbf{r}'_{pq})e^{jk_x^i\cdot pL_x}e^{jk_y^i\cdot qL_y}, \tag{6.38}$$

$$g_{P,\alpha}^{\beta} = \sum_p\sum_q g_{\alpha}^{\beta}(\mathbf{r},\mathbf{r}'_{pq})e^{jk_x^i\cdot pL_x}e^{jk_y^i\cdot qL_y}, \quad \alpha = e, m; \beta = TE, TM. \tag{6.39}$$

The brute-force realization of Eq. (6.38) - (6.39) includes three major steps: First, substitute Eq. (6.38) - (6.39) into Eq. (6.36) - (6.37) and derive the the expressions with the spatial derivatives taken. Then, prepare the spatial domain component of $\bar{\mathbf{G}}_{\alpha}(\mathbf{r},\mathbf{r}'_{pq})$ and $\nabla\times\bar{\mathbf{G}}_{\alpha}(\mathbf{r},\mathbf{r}'_{pq})$ at each shifted source point. Finally, calculate the series sum with the phase information included. However, noticing the repeated computation of the inverse Fourier transform in this process, even preparing the sampling set requires an extended computation time. In addition, the series still converge slowly in many circumstances, which further boots the time cost.

The Poisson summation formula, fortunately, relates the above spatial domain components based realization with that sampling in spectral domain. In general, for appropriate function f, the Poisson summation formula states

$$\sum_{n=-\infty}^{+\infty} f(n) = \sum_{k=-\infty}^{+\infty}\tilde{f}(k), \tag{6.40}$$

where $\tilde{f}$ is the Fourier transform of f.

Applying the Poisson summation formula to Eq. (6.38) - (6.39) , it arrives at spectral domain implementation of $\bar{\mathbf{G}}_\alpha(\mathbf{r}, \mathbf{r}'_{pq})$ and $\nabla \times \bar{\mathbf{G}}_\alpha(\mathbf{r}, \mathbf{r}'_{pq})$:

$$\bar{\mathbf{G}}_{P,\alpha}(\mathbf{r}, \mathbf{r}') = \frac{1}{L_x L_y} \sum_{p=-\infty}^{+\infty} \sum_{q=-\infty}^{+\infty} \tilde{\bar{\mathbf{G}}}_\alpha(k_{xp}, k_{yq}; z, z') e^{-jk_{xp}\cdot(x-x')} e^{-jk_{yq}\cdot(y-y')}, \quad \alpha = e, m \tag{6.41}$$

$$\begin{aligned} \nabla \times \bar{\mathbf{G}}_{P,\alpha}(\mathbf{r}, \mathbf{r}') = \frac{1}{L_x L_y} \nabla \times \sum_{p=-\infty}^{+\infty} \sum_{q=-\infty}^{+\infty} \tilde{\bar{\mathbf{G}}}_\alpha(k_{xp}, k_{yq}; z, z') \\ \cdot e^{-jk_{xp}\cdot(x-x')} e^{-jk_{yq}\cdot(y-y')}, \quad \alpha = e, m. \end{aligned} \tag{6.42}$$

where $k_{xp} = k_x^i + \frac{2\pi p}{L_x}$ and $k_{yq} = k_y^i + \frac{2\pi q}{L_y}$, and $\tilde{\bar{\mathbf{G}}}_\alpha(k_{xp}, k_{yq}; z, z')$ is the Fourier transformation of $\bar{\mathbf{G}}_\alpha(\mathbf{r}, \mathbf{r}'_{pq})$ with respect to the variable r_ρ.

Each series component of Eq. (6.41) - (6.42) can be prepared analytically without the need to calculate Fourier transform or Sommerfeld integral. As a result, the computation time can be reduced dramatically. When the source point and the observation point are not on the same $x - y$ plane, Eq. (6.41) - (6.42) converge exponentially. With the calculation of only a few periods, the PLMGF's can be obtained with high accuracy. When both the source and the observer point are on the same $x-y$ plane, especially on the same layered medium interface, the expressions of Eq. (6.41) - (6.42) become highly singular. The corresponding solution for this concern will be discussed in Section 6.3 in detail.

In order to validate the PMLGF, the first numerical example is designed as an array of tilted electric dipoles placed in a three-layer medium. The material parameters of each layer is (from top to bottom): (1) $\epsilon_r = 1, \mu_r = 1.5$; (2) $\epsilon_r = 2, \mu_r = 1$; (3) $\epsilon_r = 3, \mu_r = 1.5$. The layered medium interfaces are at $z = 0$ nm and $z = -30$ nm. In the principal cell, an electric dipole is placed at $(35, 35, -10)$ nm with the polarization of ($\theta = 30^\circ$, $\phi = 20^\circ$), and frequency of 7.5×10^{14} Hz. The $x-$ and

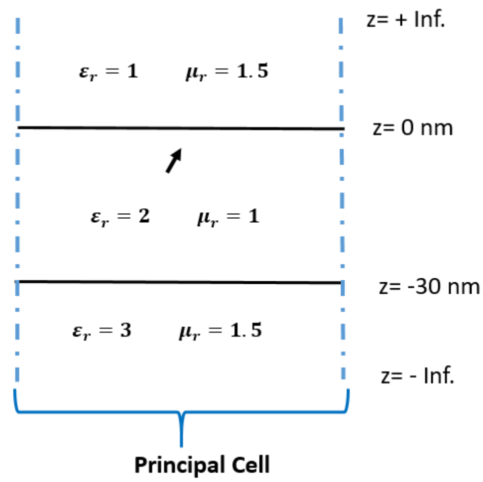

FIGURE 6.2: Illustration of the principal cell of the periodic dipole embedded in layered medium.

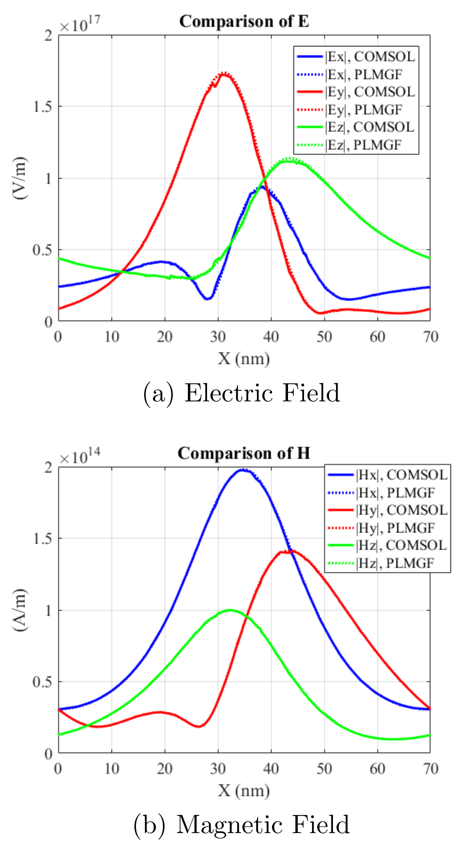

(a) Electric Field

(b) Magnetic Field

FIGURE 6.3: Validation of the PLMGF.

$y-$periodicities are 70 nm and 70 nm, respectively.

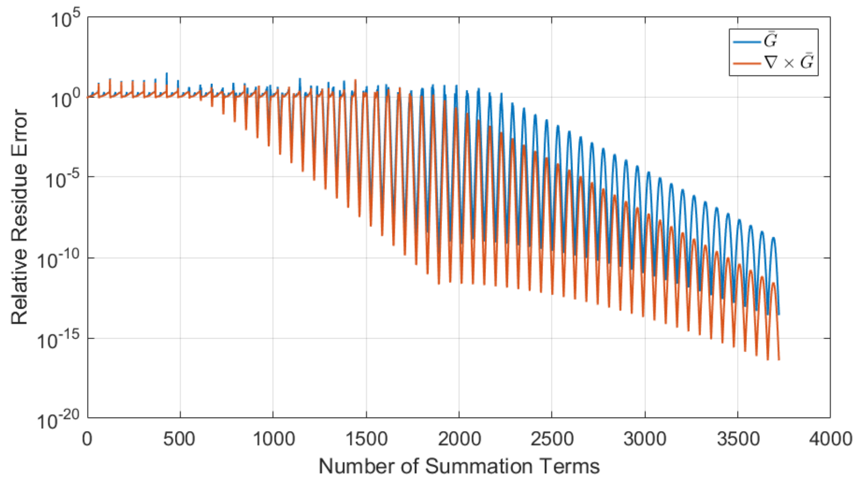

FIGURE 6.4: Convergence of spectral domain implementation, source and observation points are not on the same layered medium interface.

The electric and magnetic fields at the observation line $(0, 50, -20)$ nm $\sim$ $(70, 50, -20)$ nm are obtained through both the pure PLMGF package and the commercial software COMSOL, which utilizes the finite element method. The results of PLMGF are validated with the reference data in Fig. 6.3.

In addition to the robustness and accuracy, the computational efficiency is another essential criteria for any proposed numerical methods. Following the spectral domain implementation method, no inverse Fourier transform or Sommerfeld integral is required in the PLMGF's calculation. The convergence rate with respect to the number of summation terms is shown in Fig. 6.4. Exponential convergence can be guaranteed in most situation, only expect the case where both source and observation points lie on the same layered medium interface. The singularity extraction technique for this hyper-singular $z = z' = d_m$ situation will be further discussed in the following sections.

6.3 Matrix-Friendly Formulation of the PLMGF

The systematic formulation in Section 6.2 offers a feasible and robust implementation of the PLMGF in general. Except when both the source and observation points happen to be on the same layered medium interface, the spectral domain series converges exponentially. However, the effective computation of the PLMGF when both the source and observers are on the same interface, i.e, $z = z' = d_m$, is still meaningful in some situations. Noticing the hyper singularities in spectral domain direct implementation, further theoretical study needs to be proposed for this goal.

The singularity extraction for the PLMGF consists of two step. First, the wave function formulation PLMGF needs to be reformulated into matrix-friendly formulation. During this process, the spatial derivatives can be transfered from the Green's functions to the testing and basis functions, thus reduced the PLMGF's singularity by up to two orders. Next, the asymptotic terms of the spectral domain summation kernels are subtracted out of the series summation. Instead, the spatial domain counterparts are added back with much faster convergence rate.

Without loss of generality, in this section we only derive the matrix-friendly formulation of $\bar{\mathbf{G}}_{P,e}(\mathbf{r},\mathbf{r}')$ and $\nabla\times\bar{\mathbf{G}}_{P,e}(\mathbf{r},\mathbf{r}')$. That of the $\bar{\mathbf{G}}_{P,m}(\mathbf{r},\mathbf{r}')$ and $\nabla\times\bar{\mathbf{G}}_{P,m}(\mathbf{r},\mathbf{r}')$ can be easily obtained by applying the duality principle to their electric source counterpart.

The matrix-friendly formulation of the primary terms of the PLMGF:

$$\begin{aligned}
&< \mathbf{f}_j(\mathbf{r}), -j\omega\mu(\mathbf{r}')\bar{\mathbf{G}}^{pri}_{P,e}(\mathbf{r},\mathbf{r}'), \mathbf{f}_i(\mathbf{r}') > \\
=& -j\omega\mu(\mathbf{r}') < \mathbf{f}_j(\mathbf{r}), (\bar{\mathbf{I}} + \frac{\nabla\nabla}{k_m^2}) g_P(\mathbf{r},\mathbf{r}'), \mathbf{f}_i(\mathbf{r}') > \\
=& -j\omega\mu(\mathbf{r}') < \mathbf{f}_j(\mathbf{r}), g_P(\mathbf{r},\mathbf{r}'), \mathbf{f}_i(\mathbf{r}') > \\
&+ \frac{j}{\omega\epsilon_m} < \nabla\cdot\mathbf{f}_j(\mathbf{r}), g_P(\mathbf{r},\mathbf{r}'), \nabla'\cdot\mathbf{f}_i(\mathbf{r}') >
\end{aligned} \tag{6.43}$$

$$
\begin{aligned}
&< \mathbf{f}_j(\mathbf{r}), \mu^{-1}(\mathbf{r})\mu(\mathbf{r}')\nabla \times \bar{\mathbf{G}}^{pri}_{P,e}(\mathbf{r},\mathbf{r}'), \mathbf{f}_i(\mathbf{r}') > \\
=&\mu^{-1}(\mathbf{r})\mu(\mathbf{r}') < \mathbf{f}_j(\mathbf{r}), \nabla g_P(\mathbf{r},\mathbf{r}') \times \bar{\mathbf{I}}, \mathbf{f}_i(\mathbf{r}') >
\end{aligned}
\tag{6.44}
$$

The matrix-friendly formulation of the secondary terms of the PLMGF:

$$
\begin{aligned}
&< \mathbf{f}_j(\mathbf{r}), -j\omega\mu(\mathbf{r}')\bar{\mathbf{G}}^{sec}_{P,e}(\mathbf{r},\mathbf{r}'), \mathbf{f}_i(\mathbf{r}') > \\
=& - j\omega\mu(\mathbf{r}')[< \mathbf{f}_{Sj}(\mathbf{r}), g^{TE}_{P,s}, \mathbf{f}_{Si}(\mathbf{r}') > \\
&- < \nabla \cdot \mathbf{f}_j(\mathbf{r}), g^{TE}_P, \nabla' \cdot \mathbf{f}_i(\mathbf{r}') > \\
&- < \mathbf{f}_j(\mathbf{r}), \partial_z g^{TE}_P, \nabla' \cdot \mathbf{f}_i(\mathbf{r}') > \\
&- < \nabla \cdot \mathbf{f}_j(\mathbf{r}), \partial_{z'} g^{TE}_P, \hat{\mathbf{z}} \cdot \mathbf{f}_i(\mathbf{r}') > \\
&- < \mathbf{f}_j(\mathbf{r}) \cdot \hat{\mathbf{z}}, \partial_z\partial_{z'} g^{TE}_P, \hat{\mathbf{z}} \cdot \mathbf{f}_i(\mathbf{r}') >] \\
&- j\frac{\omega\mu(\mathbf{r}')}{k^2_{nm}}[< \nabla \cdot \mathbf{f}_j(\mathbf{r}), \partial_z\partial_{z'} g^{TM}_P, \nabla' \cdot \mathbf{f}_i(\mathbf{r}') > \\
&- k^2_n < \mathbf{f}_j(\mathbf{r}) \cdot \hat{\mathbf{z}}, \partial_{z'} g^{TM}_P, \nabla' \cdot \mathbf{f}_i(\mathbf{r}') > \\
&- k^2_m < \nabla \cdot \mathbf{f}_j(\mathbf{r}), \partial_z g^{TM}_P, \hat{\mathbf{z}} \cdot \mathbf{f}_i(\mathbf{r}') > \\
&+ k^2_n k^2_m < \hat{\mathbf{z}} \cdot \mathbf{f}_j(\mathbf{r}), g^{TM}_P, \hat{\mathbf{z}} \cdot \mathbf{f}_i(\mathbf{r}') >]
\end{aligned}
\tag{6.45}
$$

$$
\begin{aligned}
&< \mathbf{f}_j(\mathbf{r}), \mu^{-1}(\mathbf{r})\mu(\mathbf{r}')\nabla \times \bar{\mathbf{G}}^{sec}_{P,e}(\mathbf{r},\mathbf{r}'), \mathbf{f}_i(\mathbf{r}') > \\
=&\mu^{-1}(\mathbf{r})\mu(\mathbf{r}')[- < \nabla \cdot \mathbf{f}_j(\mathbf{r}), \partial z \nabla' \times \hat{z} g^{TE}_P, \mathbf{f}_i(\mathbf{r}') > \\
&+ \int_c dl \mathbf{f}_j(\mathbf{r}) \cdot \hat{\mathbf{n}} < \partial z \nabla' \times \hat{\mathbf{z}} g^{TE}_P, \mathbf{f}_i(\mathbf{r}') > \\
&+ < \hat{\mathbf{z}} \cdot \mathbf{f}_j(\mathbf{r}), k^2_n \nabla' \times \hat{z} g^{TE}_P, \mathbf{f}_i(\mathbf{r}') >] \\
&+ \frac{\mu^{-1}(\mathbf{r})\mu(\mathbf{r}')}{k^2_{nm}}[- < \mathbf{f}_j(\mathbf{r}), k^2_n \nabla \times \hat{\mathbf{z}} \partial z' g^{TM}_P, \nabla' \cdot \mathbf{f}_i(\mathbf{r}') > \\
&+ < \mathbf{f}_j(\mathbf{r}), \int_{c'} dl' k^2_n \nabla \times \hat{\mathbf{z}} \partial z' g^{TM}_P \mathbf{f}_i(\mathbf{r}') \cdot \hat{\mathbf{n}}' > \\
&+ < \mathbf{f}_j(\mathbf{r}), k^2_n k^2_m \nabla \times \hat{z} g^{TM}_P, \hat{\mathbf{z}} \cdot \mathbf{f}_i(\mathbf{r}') >]
\end{aligned}
\tag{6.46}
$$

where

$$g_{P,s}^{\alpha} = \frac{1}{A_x A_y} \sum_p \sum_q \tilde{g}_{P,s}^{\alpha}(k_{xp}, k_{yq}) e^{-j\mathbf{k}_\rho \cdot \rho} \tag{6.47}$$

$$g_{P}^{\alpha} = \frac{1}{A_x A_y} \sum_p \sum_q \tilde{g}_{P}^{\alpha}(k_{xp}, k_{yq}) e^{-j\mathbf{k}_\rho \cdot \rho} \tag{6.48}$$

with $\alpha = TE, TM$, and throughout this context the $\tilde{g}_P$ $(\tilde{g}_{P,s})$ notation denotes the spectral domain counterpart of g_P $(g_{P,s})$.

Through above process, the singularity of the double summation kernel is reduced by up to two orders, which serves as an effective platform for further acceleration and singularity extraction.

6.4 Singularity Extraction under Matrix-Friendly Formulation

The principle of singularity extraction can be generally described as

$$\sum_p \sum_q \tilde{f} = \sum_p \sum_q (\tilde{f} - \tilde{f}^{sub}) + \sum_p \sum_q f^{add}, \tag{6.49}$$

where $\tilde{f}^{sub}$ is a good asymptotic term of $\tilde{f}$, and $\sum_p \sum_q f^{add}$ exhibits significant improvement in convergence rate. The subtracted series and the add-back series are related under Poisson's summation theorem. Although direct applying this strategy to the PLMGF can be very challenging, deriving the subtracted and add-back terms are significantly more feasible under matrix-friendly formulation.

The asymptotic term of each of the double summation kernel can be obtained by introducing an attenuation constant u, such that $k_{mz} = \sqrt{(k_m^2 + u^2) - (k_{xp}^2 + k_{yq}^2 + u^2)}$ [Shubair and Chow (1993)]. Consequently, the subtraction term are obtained via the following rule:

$$k_{mz} \to -jk_{pq}^{u}, \qquad \Gamma_{n,m} \to R_{n,m}, \tag{6.50}$$

where $k_{pq}^u = \sqrt{k_{xp}^2 + k_{yq}^2 + u^2}$.

The integral kernel of the term $< \mathbf{f_{Sj}}(\mathbf{r}), g_{s,pq}^{TE}, \mathbf{f_{Si}}(\mathbf{r'}) >$ at $z = z' = d_m$ is taken as a typical example here. In this case, singularity in the secondary field terms can be extracted as

$$\begin{aligned} &\frac{1}{A_x A_y}\sum_p \sum_q -\frac{j}{2}\frac{F^{TE}(k_{xp}, k_{yq}, z, z')}{k_{mz}} e^{-j\mathbf{k}_\rho \cdot \rho} \\ =&\frac{1}{A_x A_y}\sum_p \sum_q [-\frac{j}{2}\frac{F^{TE}(k_{xp}, k_{yq}, z, z')}{k_{mz}} - \tilde{\mathcal{S}}] \cdot e^{-j\mathbf{k}_\rho \cdot \rho} \\ &+ \sum_p \sum_q \mathcal{A} \cdot e^{-j\mathbf{k}_\rho \cdot \rho} \end{aligned} \tag{6.51}$$

where

$$\begin{aligned} \tilde{\mathcal{S}} =&\frac{1}{2k_{pq}^u}[e^{-k_{pq}^u \cdot (2d_{m+1} - z - z')} M_m R_{m,m+1} \\ &+ e^{-k_{pq}^u \cdot (2d_{m+1} - 2d_m - z + z')} M_m R_{m,m+1} R_{m,m-1} \\ &+ e^{-k_{pq}^u \cdot (z + z' - 2d_m)} M_m R_{m,m-1} \\ &+ e^{-k_{pq}^u \cdot (2d_{m+1} - 2d_m + z - z')} M_m R_{m,m-1} R_{m,m+1}] \end{aligned} \tag{6.52}$$

$$\begin{aligned} \mathcal{A} =&\frac{e^{-uR_1}}{4\pi R_1} \cdot M_m R_{m,m+1} + \frac{e^{-uR_2}}{4\pi R_2} \cdot M_m R_{m,m+1} R_{m,m-1} \\ &+ \frac{e^{-uR_3}}{4\pi R_3} \cdot M_m R_{m,m-1} + \frac{e^{-uR_4}}{4\pi R_4} \cdot M_m R_{m,m-1} R_{m,m+1} \end{aligned} \tag{6.53}$$

with

$$R_1 = \sqrt{\rho_{pq}^2 + (2d_{m+1} - z - z')^2}, \tag{6.54}$$

$$R_2 = \sqrt{\rho_{pq}^2 + (2d_{m+1} - 2d_m - z + z')^2}, \tag{6.55}$$

$$R_3 = \sqrt{\rho_{pq}^2 + (z + z' - 2d_m)^2}, \tag{6.56}$$

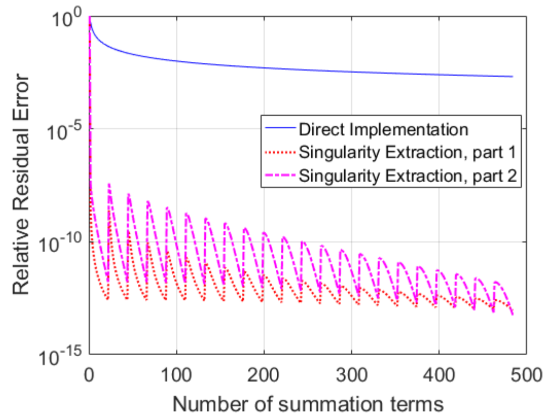

FIGURE 6.5: Convergence rates of conventional implementation and with singularity extractions. Both the source and observation points are on the same layered medium interface ($z = z' = -10$ nm).

$$R_4 = \sqrt{\rho_{pq}^2 + (2d_{m+1} - 2d_m + z - z')^2}. \tag{6.57}$$

Thus, the singularity is extracted from the original ill-convergent double summation at $z = z' = d_m$ and the convergence rate is improved in general.

Consider the same model shown in Fig. 6.2, but placing both the dipole source and observation points on the same layered medium interface $z = z' = d_m$. The convergence rates of the direct spectral domain implementation and that of the singularity extraction technique are compared in Fig. 6.5. The proposed singularity extraction method demonstrates tremendous advantages and performs as an effective solution. Compared with the direct implementation approach, the computational cost can be decreased by orders in any practical applications.

7

A Hybrid Solver for Nano Scatterers Embedded in Layered Medium: the SEBI Combined with PLMGF

The spectral element - boundary integral (SEBI) method is among the most promising methods for electromagnetic scattering analyses Lee et al. (2006); Niu et al. (2014). Inherited from the philosophy of the finite element - boundary integral (FEBI) method, its computational framework incorporates the exact radiation boundary condition with only a minor increase of the number of knowns, while its strong flexibility keeps the SEBI a competitive solution for a wide category of problems Luo et al. (2013); Niu et al. (2015, 2016). One of the major drawbacks of the conventional FEBI is its slow convergence. In many cases, a minimum 20 points per wavelength (PPW) sampling density is required for an acceptable accuracy. As an alternative, the SEBI framework implements the mixed-order Gauss-Lobatto-Legendre (GLL) sampling strategy, so that fast convergence can be achieved throughout the computation domain. Intensive investigations have been reported for the application of SEBI in microwave and optics focusing on the electromagnetic scattering from objects embedding in homogeneous or non-periodic environment Lee et al. (2009); Niu et al.

(2016); Ren et al. (2017). In spite of its efficiency and robustness, electrically small periodic nano structures fabricated in an electrically large planar layered medium, however, consists of the most common scenario in optical designs. In this work, we focus on the solutions for the periodic objects within layered medium background. For this category of problems, the conventional finite element boundary integral method requires discretization of the whole multi-scale model, resulting in a unnecessarily large number of unknowns. The surface integral equation (SIE) and volume integral equation (VIE) are also applicable approaches for the layered medium background problems. However, the SIE can only deal with homogeneous scatterers, while the VIE usually arrives at a typically large and dense linear equation system Chen et al. (2012); Ren et al. (2016).

In this chapter, we extend the SEBI framework to the study of multiscale periodic heterogeneous scatterers in planar layered medium background. Under the SEBI framework, the interior computation domain is formulated with the weak-form vector wave equation, while the radiation boundary is implemented with a set of surface integral equations. To describe the general periodic scatterers embedded in a layered medium, the SIE needs to be formulated with dyadic Green's functions. In addition, the periodic layered medium Green's function (PLMGF) must be carefully formulated to deliver a satisfying convergence rate together with a friendly implementation interface. With the combined SEBI-PLMGF method, the computation domain completely excludes the layered medium background, and an exponential convergence is expected for the solver.

7.1 Periodic Boundary Integral Spectral Element Method for Layered Background

Inherited from the conventional FEBI method, the SEBI-PLMGF method truncates the open boundary surface of the computation domain with a set of SIEs, while the

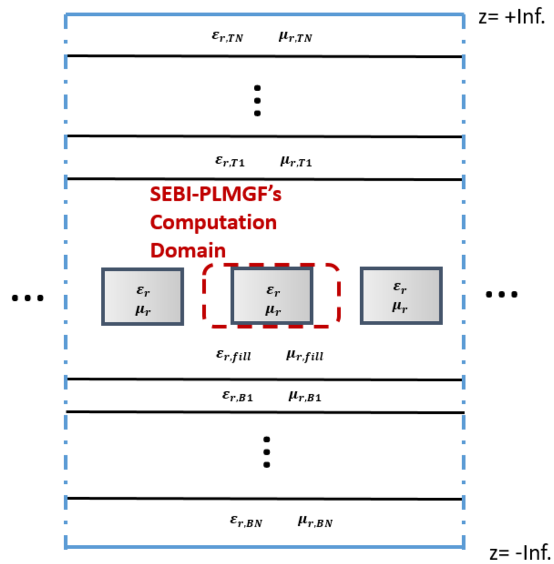

FIGURE 7.1: Illustration of the reduced computation domain under the SEBI-PLMGF framework.

interior computational domain is interpolated with a special category of local basis functions. Figure 7.1 provides an illustration of the reduced computation domain under the SEBI-PLMGF framework. In order to effectively model the multiscale nano-optical scattering problem, the SIEs are formulated with the periodic layered medium dyadic Green's function, thus, the unknowns for the wave equation describing the background formation can be compressed into a set of equivalent surface integral equations. The region without scatterers therefore can be truncated from the final computation domain. Moreover, the Floquet theorem is further enforced as a set of periodic boundary conditions at the final linear equation system level, hence, the computation domain only cover one principal cell of the whole periodic structure.

In this section, we first derive the overall framework of the SEBI. The implementation and formulation of the PLMGF will be discussed systematically in Section 7.2. The final linear equation system together with the enforcement of the periodic boundary condition is then discussed in Section 7.3.

Under the SEBI framework, the electric field in the interior computation domain is governed by the vector Helmholtz equation. Following the Galerkin's method, the weak-form wave equation can be obtained as [Niu et al. (2014)]

$$\begin{aligned}\int_V -(\nabla \times \mathbf{\Phi_i})^T \cdot \mu_r^{-1} \cdot (\nabla \times \mathbf{E}) dV + k_0^2 \int_V \mathbf{\Phi_i}^T \cdot \epsilon_r \cdot \mathbf{E} dV \\ + jk_0 \int_S \mathbf{\Phi_i}^T \cdot (\hat{\mathbf{n}} \times \tilde{\mathbf{H}}) dS = \int_V \mathbf{\Phi_i}^T \cdot \mathbf{S_e} dV\end{aligned} \tag{7.1}$$

where $\mathbf{\Phi_i}$ denotes the testing function; $\hat{\mathbf{n}}$ is the normal unit vector towards the exterior computation domain; $\mathbf{S_e}$ is the excitation source inside the computation domain.

For the electromagnetic scattering problem with dual periodicity in the $\hat{\mathbf{a}}_1$ and $\hat{\mathbf{a}}_2$ directions, the radiation boundary consists of two separate surfaces. Without loss of generality, we assume the scatterer is periodic in x and y directions. Therefore, the radiation boundary consists of the top and bottom surfaces of the computation domain, both parallel to the XOY plane with no mutual coupling. For each of these surfaces, a set of electric field integral equation (EFIE) and magnetic field integral equation (MFIE) are combined with Eq. (7.1) to describe the wave propagation in the exterior domain:

$$\hat{\mathbf{n}} \times [\mathbf{E}(\mathbf{r}) - \mathbf{E}^{inc}] = \hat{\mathbf{n}} \times [\mathcal{L}_E(\mathbf{r}, \mathbf{J}) + \mathcal{K}_E(\mathbf{r}, \mathbf{M})] \tag{7.2}$$

$$\hat{\mathbf{n}} \times [\mathbf{H}(\mathbf{r}) - \mathbf{H}^{inc}] = \hat{\mathbf{n}} \times [\mathcal{L}_H(\mathbf{r}, \mathbf{M}) + \mathcal{K}_H(\mathbf{r}, \mathbf{J})] \tag{7.3}$$

where $\mathbf{J}$ denotes the electric current source and $\mathbf{M}$ denotes the magnetic current source. Throughout this paper, $\mathbf{r}$ denotes the observation point and $\mathbf{r}'$ denotes the source point.

There are generally four types of integral operators associated with the SIE: $\mathcal{L}_E$, $\mathcal{K}_E$, $\mathcal{L}_H$, $\mathcal{K}_H$.

$$\mathcal{L}_E(\mathbf{r}, \mathbf{X}) = -j\omega \int d\mathbf{r}' \bar{\mathbf{G}}_{P,e}(\mathbf{r}, \mathbf{r}')\mu(\mathbf{r}')\mathbf{X}(\mathbf{r}') \tag{7.4}$$

$$\mathcal{K}_E(\mathbf{r}, \mathbf{X}) = -\epsilon^{-1}(\mathbf{r}) \int d\mathbf{r}' \nabla \times \bar{\mathbf{G}}_{P,m}(\mathbf{r}, \mathbf{r}')\epsilon(\mathbf{r}')\mathbf{X}(\mathbf{r}') \tag{7.5}$$

$$\mathcal{L}_H(\mathbf{r}, \mathbf{X}) = -j\omega \int d\mathbf{r}' \bar{\mathbf{G}}_{P,m}(\mathbf{r}, \mathbf{r}')\epsilon(\mathbf{r}')\mathbf{X}(\mathbf{r}') \tag{7.6}$$

$$\mathcal{K}_H(\mathbf{r}, \mathbf{X}) = \mu^{-1}(\mathbf{r}) \int d\mathbf{r}' \nabla \times \bar{\mathbf{G}}_{P,e}(\mathbf{r}, \mathbf{r}')\mu(\mathbf{r}')\mathbf{X}(\mathbf{r}') \tag{7.7}$$

where $\bar{\mathbf{G}}_{P,m}$ and $\bar{\mathbf{G}}_{P,e}$ denotes the periodic magnetic-type and electric-type layered medium Green's function, respectively. The periodic Green's functions are distinguished from the regular Green's functions with the subscript P.

Inserting Eq. (7.3), the MFIE, into the surface integral term of Eq. (7.1),

$$\begin{aligned}\int_V -(\nabla \times \mathbf{\Phi_i})^T \cdot \mu_r^{-1} \cdot (\nabla \times \mathbf{E}) dV + k_0^2 \int_V \mathbf{\Phi_i}^T \cdot \epsilon_r \cdot \mathbf{E} dV \\ -jk_0 \int_S (\hat{\mathbf{n}} \times \mathbf{\Phi_i})^T \cdot [\eta_0 \mathcal{L}_H(\mathbf{r}, \mathbf{M}) + \mathcal{K}_H(\mathbf{r}, \tilde{\mathbf{J}})] dS \\ = jk_0 \int_S (\hat{\mathbf{n}} \times \mathbf{\Phi_i})^T \cdot \tilde{\mathbf{H}}^{inc} dS + \int_V \Phi_i^T \cdot \mathbf{S_e} dV\end{aligned} \tag{7.8}$$

where η_0 is the wave impedance in free space.

Equation (7.2) (the EFIE) is directly applied with Galerkin's method to arrive at its weak form:

$$\begin{aligned}jk_0 \int_S (\hat{\mathbf{n}} \times \mathbf{\Phi_i})^T \cdot \mathbf{E}^{inc} dS = -jk_0 \int_S (\hat{\mathbf{n}} \times \mathbf{\Phi_i})^T \cdot \\ [-\mathbf{E}(\mathbf{r}) + \frac{1}{\eta_0} \mathcal{L}_E(\mathbf{r}, \tilde{\mathbf{J}}) + \mathcal{K}_E(\mathbf{r}, \mathbf{M})] dS.\end{aligned} \tag{7.9}$$

Combining Eq. (7.8) - (7.9) with proper discretization strategy, the electromagnetic scattering problem for periodic scatterers embedded in layered background can be solved without interior resonance concern [Shanker et al. (2000); Collins et al. (1992)]. The final matrix-form linear equation system will be revisited in detail in Section 7.3 after the systematic discussion of the PLMGF and the periodic boundary conditions' implementation.

7.2 Formulation of the Periodic Layered Medium Green's Function under SEBI Framework

7.2.1 Overview

The necessity of introducing the PLMGF originates from the SIE-based radiation boundary condition. The PLMGF here can be intuitively considered as the impulse response of a set of periodic electric/ magnetic point sources embedded in the layered background medium. For arbitrary electric and magnetic current sources, the governing equation of the field response can be conveniently expressed with the dyadic magnetic-type ($\bar{\mathbf{G}}_{P,m}$) and electric-type ($\bar{\mathbf{G}}_{P,e}$) periodic Green's functions. In the remaining discussions, the subscript m and n denotes the layer index of the source point and observation point, respectively; p, q are the indices of the double summation; k_m is the wave number in the m-th layer.

The electric-type and magnetic-type PLMGF can be equivalently expressed with their spectral domain components or spatial domain components:

$$\begin{aligned}\bar{\mathbf{G}}_P(\mathbf{r},\mathbf{r}') &= \sum_{p=-\infty}^{+\infty}\sum_{q=-\infty}^{+\infty}\bar{\mathbf{G}}_{pq}(\mathbf{r},\mathbf{r'}_{pq})e^{jk_x^i pL_x}e^{jk_y^i qL_y}\\ &=\frac{1}{L_xL_y}\sum_{p=-\infty}^{+\infty}\sum_{q=-\infty}^{+\infty}\tilde{\bar{\mathbf{G}}}_{pq}(k_{xp},k_{yq};z,z')\cdot\\ &\quad e^{-jk_{xp}(x-x')}e^{-jk_{yq}(y-y')}\end{aligned} \tag{7.10}$$

where L_x and L_y are the periods in x, y directions; $\mathbf{r'}_{pq} = \mathbf{r'} + (pL_x, qL_y, 0)^T$. The above two equalities are related with the Poisson summation theorem. In the following discussion, we only focuses on the matrix representation of $\bar{\mathbf{G}}_{P,e}$ and $\nabla \times \bar{\mathbf{G}}_{P,e}$ in Eq. (7.4), (7.7) . The terms associated with $\bar{\mathbf{G}}_{P,m}$ and $\nabla \times \bar{\mathbf{G}}_{P,m}$ can be easily obtained through the duality principle [Chen et al. (2012); Chew et al. (2006)].

In general, for one-dimensional piecewise constant materials, the non-periodic layered medium Green's function can be determined analytically in the spectral domain, and the spatial domain counterpart needs to be obtained through calculating the Sommerfeld integrals, which is usually a costly process. For periodic layered medium Green's function, although closed formulation usually cannot be obtain in either domain, the Poisson's summation theorem bridges the implementation roadmap in the spectral domain and the spatial domain. The double summation in spatial domain can be equivalently transformed into that in spectral domain.

It might be intuitive that computing the spectral domain summation is considerably superior to realizing the spatial domain formulation, where every single term in the series represents a shifted non-periodic dyadic layered medium Green's function. Each term's preparation requires a Fourier transform of its closed-form spectral domain counterpart. However, from the implementation point of view, the PLMGF is highly singular within the context of weak-form SIEs. Singularity issues are always present under pure spectral or spatial domain formulation. Conversely, the spectral domain and spatial domain representation exhibits distinct analytical properties. Switching between these two domains is essential to convert the generalized function into integrable express, and thus extract the singularities.

The same concern also holds for the primary terms and the secondary terms of the PLMGF for their distinct analytical properties. For this reason, we always split the Green's function related SEBI terms into primary and secondary components, and formulate them separately. The singularity issues therefore can be extracted from the series summation and avoid massive unnecessary computation.

7.2.2 Matrix Representation of the PLMGF's Primary Terms

The primary term of the dyadic Green's function is defined as the point source's direct contribution in the source without any reflections from other layers. Therefore, the PLMGF's primary terms are the same as the dyadic Green's function for a homogeneous medium, and is non-zeros only when the observer and the source are within the same medium layer.

Primary term of $\bar{\mathbf{G}}_{P,e}$

The primary term of $\bar{\mathbf{G}}_{P,e}$ in Eq. 7.4 is

$$\bar{\mathbf{G}}_{P,e}(\mathbf{r},\mathbf{r}') = \sum_p \sum_q (\bar{\mathbf{I}} + \frac{\nabla\nabla}{k_m^2}) g(\mathbf{r},\mathbf{r}'_{pq}) \cdot e^{jk_x^i pL_x} e^{jk_y^i qL_y} \tag{7.11}$$

where g denotes the scalar Green's function

$$g(\mathbf{r},\mathbf{r}') = \frac{e^{-jk_m|\mathbf{r}-\mathbf{r}'|}}{4\pi|\mathbf{r}-\mathbf{r}'|}. \tag{7.12}$$

The hyper-singularity in the above expression originates from the $\nabla\nabla$ operator. Fortunately, within the context of SEBI, the spatial derivative can be shifted to the testing and basis functions. The primary components of the $\bar{\mathbf{G}}_{P,e}$ related terms can be express in matrix representation:

$$\begin{aligned}
& < \hat{\mathbf{n}} \times \mathbf{\Phi_i}(\mathbf{r}), \mathcal{L}_E, \hat{\mathbf{n}} \times \mathbf{\Phi_j}(\mathbf{r}') > \\
= & < \hat{\mathbf{n}} \times \mathbf{\Phi_i}(\mathbf{r}), \bar{\mathbf{G}}_{P,e}(\mathbf{r},\mathbf{r}'), \hat{\mathbf{n}} \times \mathbf{\Phi_j}(\mathbf{r}') > \\
= & < \hat{\mathbf{n}} \times \mathbf{\Phi_i}, \sum_p \sum_q g(\mathbf{r},\mathbf{r}'_{pq}) \cdot e^{jk_x^i pL_x} e^{jk_y^i qL_y}, \hat{\mathbf{n}} \times \mathbf{\Phi_j} > \\
& - \frac{1}{k_m^2} < \nabla \cdot (\hat{\mathbf{n}} \times \mathbf{\Phi_i}), \sum_p \sum_q g(\mathbf{r},\mathbf{r}'_{pq}) \cdot e^{jk_x^i pL_x} e^{jk_y^i qL_y}, \nabla' \cdot (\hat{\mathbf{n}} \times \mathbf{\Phi_j}) > .
\end{aligned} \tag{7.13}$$

The integral kernel in Eq. (7.13) converge linearly under spatial domain realization. As an alternative, applying the Poisson's summation theorem, it can be equivalently expressed as

$$\begin{aligned}
&\sum_p \sum_q g(\mathbf{r}, \mathbf{r'}_{pq}) \cdot e^{jk_x^i pL_x} e^{jk_y^i qL_y} \\
=&\frac{1}{L_x L_y} \sum_p \sum_q \frac{-j}{2k_{mz}} e^{-jk_{mz}|z-z'|} \cdot e^{-jk_{xp}(x-x')} e^{-jk_{yq}(y-y')},
\end{aligned} \tag{7.14}$$

which exhibits exponential convergence when $z \neq z'$, and retains linear convergence when $z = z'$.

Primary term of $\nabla \times \bar{\mathbf{G}}_{P,e}$

The primary term of $\nabla \times \bar{\mathbf{G}}_{P,e}$ in Eq. (7.7) is

$$\begin{aligned}
\nabla \times \bar{\mathbf{G}}_{P,e} &= \sum_p \sum_q \nabla \times \bar{\mathbf{G}}_e(\mathbf{r}, \mathbf{r'}_{pq}) \cdot e^{jk_x^i pL_x} e^{jk_y^i qL_y} \\
=&\sum_{p=-\infty}^{+\infty} \sum_{q=-\infty}^{+\infty} \begin{bmatrix} 0 & -\partial_z & \partial_y \\ \partial_z & 0 & -\partial_x \\ -\partial_y & \partial_x & 0 \end{bmatrix} g(\mathbf{r}, \mathbf{r'}_{pq}) \cdot e^{jk_x^i pL_x} e^{jk_y^i qL_y}. \\
=&\sum_p \sum_q \begin{bmatrix} 0 & -(z-z') & y-y' \\ z-z' & 0 & -(x-x') \\ -(y-y') & x-x' & 0 \end{bmatrix} \\
&\frac{1}{R_{pq}} \cdot (-jk_m - \frac{1}{R_{pq}}) \cdot \frac{e^{-jk_m R_{pq}}}{4\pi R_{pq}} \cdot e^{jk_x^i pL_x} e^{jk_y^i qL_y}.
\end{aligned} \tag{7.15}$$

where R_{pq} denotes $|\mathbf{r} - \mathbf{r'}_{pq}|$.

The first attempt to accelerate the convergence of the above is transforming it into a spectral domain series. Through the Poisson's summation theorem, Eq. (7.15) arrives at

$$\begin{aligned}
\nabla \times \bar{\mathbf{G}}_{P,e} = \frac{1}{A_x A_y} \sum_p \sum_q &\begin{bmatrix} 0 & -\partial_z & \partial_y \\ \partial_z & 0 & -\partial_x \\ -\partial_y & \partial_x & 0 \end{bmatrix} \\
&\frac{-j}{2k_{mz}} \cdot e^{-jk_{mz}\cdot|z-z'|} \cdot e^{-jk_{xp}(x-x')} e^{-jk_{yq}(y-y')}, \\
&(z \neq z').
\end{aligned} \tag{7.16}$$

Equation (7.16) exhibits exponential convergence when $z \neq z'$. However, when $z = z'$ the above is a typical scenario where generalized function issue arises: $\partial_z e^{-jk_{mz}\cdot|z-z'|}$ results in a generalized function. As a result, the primary term of $\nabla \times \bar{\mathbf{G}}_{P,e}$ needs to be formulated separately for two situations. When $z \neq z'$, computing through Eq. (7.16) with exponential convergence; when $z = z'$, stay with Eq. (7.15) so that the singularity can be extracted.

Although the above are valid in general, the surface integral kernel is still strongly singular ($1/R^2$-type) when $z = z'$. However, recalling that all the formulation of the PLMGF is prepared under the assumption that the scatterer is periodic in the x and y directions. Within the periodic SEBI framework, the scattering boundary surface is parallel to the XOY plane, i.e. $\hat{\mathbf{n}} = \pm\hat{\mathbf{z}}$ and $z = z'$. The zero value xx, xy, yx, yy tensor components of $\nabla \times \bar{\mathbf{G}}_{P,e}$ thus considerably simplify the final implementation. The primary components of the $\nabla \times \bar{\mathbf{G}}_{P,e}$ related terms can be expressed in matrix representation as

$$\begin{aligned} &< \hat{\mathbf{n}} \times \mathbf{\Phi_i}(\mathbf{r}), \mathcal{K}_H, \hat{\mathbf{n}} \times \mathbf{\Phi_j}(\mathbf{r}') > \\ =& < \hat{\mathbf{n}} \times \mathbf{\Phi_i}(\mathbf{r}), \tilde{\mathcal{K}}_H, \hat{\mathbf{n}} \times \mathbf{\Phi_j}(\mathbf{r}') > \\ &+ \frac{1}{2} < \hat{\mathbf{n}} \times \mathbf{\Phi_i}(\mathbf{r}), \mathbf{\Phi_j}(\mathbf{r}) > \\ =& \frac{1}{2} < \hat{\mathbf{n}} \times \mathbf{\Phi_i}(\mathbf{r}), \mathbf{\Phi_j}(\mathbf{r}) > \end{aligned} \tag{7.17}$$

where $\tilde{\mathcal{K}}_H$ calculates the Cauchy principal integrals with the singular point at $\mathbf{r} = \mathbf{r}'$ removed, and has been evaluated as zero.

7.2.3 Matrix Representation of the PLMGF's Secondary Terms

The secondary term of the PLMGF is defined to account for the transmission and reflection of the layered medium.

Secondary term of $\bar{\mathbf{G}}_{P,e}$

For $\bar{\mathbf{G}}_{P,e}$ in Eq. (7.4), matrix representation of the secondary term is

$$
\begin{aligned}
&< \hat{\mathbf{n}} \times \mathbf{\Phi_i}(\mathbf{r}), \bar{\mathbf{G}}_{P,e}, \hat{\mathbf{n}} \times \mathbf{\Phi_j}(\mathbf{r}') > \\
= &< \hat{\mathbf{n}} \times \mathbf{\Phi_i}(\mathbf{r}), \bar{\mathbf{G}}^{TE}_{P,e}(\mathbf{r}, \mathbf{r}'), \hat{\mathbf{n}} \times \mathbf{\Phi_j}(\mathbf{r}') > \\
&+ \frac{1}{k^2_{nm}} < \hat{\mathbf{n}} \times \mathbf{\Phi_i}(\mathbf{r}), \bar{\mathbf{G}}^{TM}_{P,e}(\mathbf{r}, \mathbf{r}'), \hat{\mathbf{n}} \times \mathbf{\Phi_j}(\mathbf{r}') >
\end{aligned}
\tag{7.18}
$$

where

$$k^2_{nm} = \omega^2 \epsilon_n \mu_m, \tag{7.19}$$

$$
\begin{aligned}
\bar{\mathbf{G}}^{TE}_{P,e}(\mathbf{r}, \mathbf{r}') = &\sum_p \sum_q (\nabla \times \hat{\mathbf{z}})(\nabla' \times \hat{\mathbf{z}}) \cdot \\
&g^{TE}(\mathbf{r}, \mathbf{r'}_{pq}) e^{jk^i_x p L_x} e^{jk^i_y q L_y},
\end{aligned}
\tag{7.20}
$$

$$
\begin{aligned}
\bar{\mathbf{G}}^{TM}_{P,e}(\mathbf{r}, \mathbf{r}') = &\sum_p \sum_q (\nabla \times \nabla \times \hat{\mathbf{z}})(\nabla' \times \nabla' \times \hat{\mathbf{z}}) \cdot \\
&g^{TM}(\mathbf{r}, \mathbf{r'}_{pq}) e^{jk^i_x p L_x} e^{jk^i_y q L_y}.
\end{aligned}
\tag{7.21}
$$

The above spatial domain summation expressions of $\bar{\mathbf{G}}^{TE}_e(\mathbf{r}, \mathbf{r'}_{pq})$ and $\bar{\mathbf{G}}^{TM}_e(\mathbf{r}, \mathbf{r'}_{pq})$ directly originate from the definition of periodic Green's function. They can be equivalently written as

$$
\begin{aligned}
\bar{\mathbf{G}}^{TE}_{P,e}(\mathbf{r}, \mathbf{r}') = &\begin{bmatrix} \partial_y \partial_{y'} & -\partial_y \partial_{x'} & 0 \\ -\partial_x \partial_{y'} & \partial_x \partial_{x'} & 0 \\ 0 & 0 & 0 \end{bmatrix} \cdot \\
&\sum_p \sum_q g^{TE}(\mathbf{r}, \mathbf{r'}_{pq}) e^{jk^i_x p L_x} e^{jk^i_y q L_y},
\end{aligned}
\tag{7.22}
$$

$$
\begin{aligned}
\bar{\mathbf{G}}^{TM}_{P,e}(\mathbf{r}, \mathbf{r}') = &\begin{bmatrix} \partial_x \partial_{x'} \partial_z \partial_{z'} & \partial_x \partial_{y'} \partial_z \partial_{z'} & \partial_x \partial_z k^2_\rho \\ \partial_y \partial_{x'} \partial_z \partial_{z'} & \partial_y \partial_{y'} \partial_z \partial_{z'} & \partial_y \partial_z k^2_\rho \\ \partial_{x'} \partial_{z'} k^2_\rho & \partial_{y'} \partial_{z'} k^2_\rho & k^4_\rho \end{bmatrix} \cdot \\
&\sum_p \sum_q g^{TM}(\mathbf{r}, \mathbf{r'}_{pq}) e^{jk^i_x p L_x} e^{jk^i_y q L_y}.
\end{aligned}
\tag{7.23}
$$

with

$$\begin{aligned} g^{\alpha}(\mathbf{r}, \mathbf{r}'_{pq}) &= \mathcal{F}^{-1}\{\tilde{g}^{\alpha}(k_{xp}, k_{yq}, z, z')\} \\ &= \mathcal{F}^{-1}\{-\frac{j}{2} \cdot \frac{F^{\alpha}(k_\rho; z, z')}{k_{mz}k_\rho^2}\}. \end{aligned} \tag{7.24}$$

Here $\mathcal{F}^{-1}$ denotes the inverse Fourier transform with respect to the k_ρ variable, and $\alpha = TE, TM$.

Different from the PLMGF's primary field terms, the summation kernel and its spatial derivatives of Eq. (7.22) - (7.23) cannot be expressed in closed form. To avoid repeatedly calculating the inverse transformation or Sommerfeld integral, the above can be transformed into spectral domain realization:

$$\begin{aligned} \bar{\mathbf{G}}_{P,e}^{TE}(\mathbf{r}, \mathbf{r}') = &\begin{bmatrix} \partial_y \partial_{y'} & -\partial_y \partial_{x'} & 0 \\ -\partial_x \partial_{y'} & \partial_x \partial_{x'} & 0 \\ 0 & 0 & 0 \end{bmatrix} \cdot \frac{1}{L_x L_y} \cdot \\ &\sum_p \sum_q \tilde{g}^{TE}(k_{xp}, k_{yq}; z, z') e^{-jk_{xp}(x-x')} e^{-jk_{yq}(y-y')}, \end{aligned} \tag{7.25}$$

$$\begin{aligned} \bar{\mathbf{G}}_{P,e}^{TM}(\mathbf{r}, \mathbf{r}') = &\begin{bmatrix} \partial_x \partial_{x'} \partial_z \partial_{z'} & \partial_x \partial_{y'} \partial_z \partial_{z'} & \partial_x \partial_z k_\rho^2 \\ \partial_y \partial_{x'} \partial_z \partial_{z'} & \partial_y \partial_{y'} \partial_z \partial_{z'} & \partial_y \partial_z k_\rho^2 \\ \partial_{x'} \partial_{z'} k_\rho^2 & \partial_{y'} \partial_{z'} k_\rho^2 & k_\rho^4 \end{bmatrix} \cdot \frac{1}{L_x L_y} \cdot \\ &\sum_p \sum_q \tilde{g}^{TM}(k_{xp}, k_{yq}; z, z') e^{-jk_{xp}(x-x')} e^{-jk_{yq}(y-y')}. \end{aligned} \tag{7.26}$$

Substituting Eq. (7.25) - (7.26) into Eq. (7.18), the matrix representation of $\bar{\mathbf{G}}_{P,e}$'s secondary terms can be efficiently prepared.

Secondary term of $\nabla \times \bar{\mathbf{G}}_{P,e}$

For $\nabla \times \bar{\mathbf{G}}_{P,e}$ in Eq. (7.7), matrix representation of the secondary term is

$$\begin{aligned}
&< \hat{\mathbf{n}} \times \mathbf{\Phi_i}(\mathbf{r}), \nabla \times \bar{\mathbf{G}}_{P,e}, \hat{\mathbf{n}} \times \mathbf{\Phi_j}(\mathbf{r}') > \\
= &< \hat{\mathbf{n}} \times \mathbf{\Phi_i}(\mathbf{r}), \nabla \times \bar{\mathbf{G}}^{TE}_{P,e}(\mathbf{r}, \mathbf{r}'), \hat{\mathbf{n}} \times \mathbf{\Phi_j}(\mathbf{r}') > \\
&+ \frac{1}{k_{nm}^2} < \hat{\mathbf{n}} \times \mathbf{\Phi_i}(\mathbf{r}), \nabla \times \bar{\mathbf{G}}^{TM}_{P,e}(\mathbf{r}, \mathbf{r}'), \hat{\mathbf{n}} \times \mathbf{\Phi_j}(\mathbf{r}') >
\end{aligned} \tag{7.27}$$

where

$$\begin{aligned}
\nabla \times \bar{\mathbf{G}}^{TE}_{P,e}(\mathbf{r}, \mathbf{r}') = &\sum_p \sum_q (\nabla \times \nabla \times \hat{\mathbf{z}})(\nabla' \times \hat{\mathbf{z}}) \\
&g^{TE}(\mathbf{r}, \mathbf{r}'_{pq}) e^{jk_x^i p L_x} e^{jk_y^i q L_y}
\end{aligned} \tag{7.28}$$

$$\begin{aligned}
\nabla \times \bar{\mathbf{G}}^{TM}_{P,e}(\mathbf{r}, \mathbf{r}') = &\sum_p \sum_q k_n^2 (\nabla \times \hat{\mathbf{z}})(\nabla' \times \nabla' \times \hat{\mathbf{z}}) \\
&g^{TM}(\mathbf{r}, \mathbf{r}'_{pq}) e^{jk_x^i p L_x} e^{jk_y^i q L_y}.
\end{aligned} \tag{7.29}$$

Similarly to the secondary term of the $\bar{\mathbf{G}}_{P,e}$, all components inside the double summation operator are not in closed form. Fortunately, the above can be equivalently transformed into spectral domain realization:

$$\begin{aligned}
\nabla \times \bar{\mathbf{G}}^{TE}_{P,e}(\mathbf{r}, \mathbf{r}') = &\begin{bmatrix} \partial_x \partial_z \partial_{y'} & -\partial_x \partial_z \partial_{x'} & 0 \\ \partial_y \partial_z \partial_{y'} & -\partial_y \partial_z \partial_{x'} & 0 \\ k_\rho^2 \partial_{y'} & -k_\rho^2 \partial_{x'} & 0 \end{bmatrix} \cdot \\
&\frac{1}{L_x L_y} \cdot \sum_p \sum_q \tilde{g}^{TE}(k_{xp}, k_{yq}; z, z') \cdot \\
&e^{-jk_{xp}(x-x')} e^{-jk_{yq}(y-y')}
\end{aligned} \tag{7.30}$$

$$\nabla \times \bar{\mathbf{G}}_{P,e}^{TM}(\mathbf{r},\mathbf{r}') = \begin{bmatrix} \partial_y \partial_{x'} \partial_{z'} & \partial_y \partial_{y'} \partial_{z'} & \partial_y k_\rho^2 \\ -\partial_x \partial_{x'} \partial_{z'} & -\partial_x \partial_{y'} \partial_{z'} & -\partial_x k_\rho^2 \\ 0 & 0 & 0 \end{bmatrix} \cdot$$
$$\frac{1}{L_x L_y} \cdot \sum_p \sum_q k_n^2 \cdot \tilde{g}^{TM}(k_{xp}, k_{yq}; z, z') \cdot \tag{7.31}$$
$$e^{-jk_{xp}(x-x')} e^{-jk_{yq}(y-y')}.$$

Substituting Eq. (7.30) - (7.31) into Eq. (7.27), the matrix representation of $\nabla \times \bar{\mathbf{G}}_{P,e}$'s secondary terms can also be efficiently prepared.

It should be noticed that the secondary terms of the PLMGF converges exponentially if the source point and the observation point are not exactly on the same layered medium interface. This condition can be comfortably satisfied in most periodic SEBI applications. Even for the case $z = z' = z_m$, where z_m denotes the z-coordinate of the m-th layered medium interface, the singularity still can be efficiently extracted under the matrix friendly formulation of the PLMGF [Chen et al. (2015)].

7.3 Discretization and Bloch Periodic Boundary Condition

Different from the philosophy of realizing the radiation boundary condition in the SEBI framework, the enforcement of the periodic boundary condition is derived under the spectral element method framework for boundary value problems. Before enforcing the Bloch boundary conditions to the lateral surfaces of the computation domain, we first discretize the unknowns in the weak-form wave equations and the SIE's.

One of the major advantages of the SEBI or SEM originates from the GLL interpolation basis function. Compared with the quadratic convergence of the conventional finite element method [Jin (2014)], the SEM exhibits exponential convergence with respect to the increase of the order of interpolation polynomials. Discretizing both the SEM and MoM domain with the GLL basis function, Eq. (7.8) - (7.9) arrive at the linear equation system:

$$\begin{bmatrix} \mathbf{K_{II}} & \mathbf{K_{IS}} & \mathbf{0} \\ \mathbf{K_{SI}} & \mathbf{K_{SS}} + \mathbf{L_H} & \mathbf{K_H} \\ \mathbf{0} & \mathbf{K_E} & \mathbf{L_E} \end{bmatrix} \begin{bmatrix} \mathbf{E_I} \\ \mathbf{E_S} \\ \tilde{\mathbf{H}}_\mathbf{S} \end{bmatrix} = \begin{bmatrix} \mathbf{S_e} \\ \tilde{\mathbf{H}}^{\mathbf{inc}} \\ \mathbf{E^{inc}} \end{bmatrix} \tag{7.32}$$

where $\mathbf{K}$ block matrices are the combination of the mass matrix and the stiffness matrix from the SEM formulation. Their first and second subscripts denote the sub-domain of the testing and basis functions, respectively. The subscript I denotes the interior computation domain; S denotes the radiation boundary surfaces domain. $\mathbf{L_E}, \mathbf{L_H}$, $\mathbf{K_E}$, $\mathbf{K_H}$ represents the block impedance matrices corresponding to the integral operators L_E, L_H, K_E, K_H, respectively. For compact and neat denotations of the global equation system, the single integrals terms of $\int_S(\hat{\mathbf{n}} \times \mathbf{\Phi_i})^T \cdot \mathbf{E}(\mathbf{r})dS$ and $\int_S(\hat{\mathbf{n}} \times \mathbf{\Phi_i})^T \cdot \tilde{\mathbf{H}}(\mathbf{r})dS$ in the EFIE and MFIE are assembled into the $\mathbf{L_E}, \mathbf{L_H}$, $\mathbf{K_E}$, $\mathbf{K_H}$ block matrices with the proper mapping. Through the above linear sparse equation system, the exponential convergence is expected for both the SEM domain and the MoM boundary surfaces.

Following the same principle of Bloch periodic boundary condition enforcement proposed in Chaper 2, Eq. (2.26) - (2.36), redundant degree of freedoms can be removed from the equation system.

7.4 Validation and Numerical Examples

In this section, we show three typical numerical examples to validate the proposed solver and demonstrate its computational performance. First, the compact split field implementation of the PLMGF is validated. In the next example, we introduce a sub-wavelength nano scale example to validate the SEBI-PLMGF solver. Then, the fast convergence advantage of the SEBI-PLMGF is illustrated for three typical scenarios. Finally, the proposed solver is extended to electrically large multiscale extreme ultraviolet (EUV) lithography simulation, which is extremely challenging for conventional methods.

7.4.1 Case 1: Periodic Dipole Array in Layered Medium

As a validation of the compact split-field implementation of the PLMGF, the first numerical example is design to compare the numerical results and the computational performances of the compact split-field implementation and the direct spectral domain implementation.

Figure 7.2 provides a sketch of the layered medium model. From top to bottom, the material parameters of each layer is: (1) $\epsilon_r = 1 - 0.01j, \mu_r = 2.5$; (2) $\epsilon_r = 2 - 0.01j, \mu_r = 2.5$; (3) $\epsilon_r = 3 - 0.01j, \mu_r = 2.5$; (4) $\epsilon_r = 4 - 0.01j, \mu_r = 1.0$; (5) $\epsilon_r = 5 - 0.01j, \mu_r = 1.5$; (6) $\epsilon_r = 6 - 0.01j, \mu_r = 1.5$; (7) $\epsilon_r = 7 - 0.01j, \mu_r = 1.0$. The layered medium interfaces are at $z = 0$ nm and $z = -30$ nm. In the principal cell, the dipole source is placed at $(35, 35, -10)$ nm with the polarization of ($\theta = 30°$, $\phi = 20°$); the $x-$ and $y-$periodicities are 70 nm and 70 nm, respectively. Both electric and magnetic dipole sources of 400 nm wavelength are considered.

The field results are compared in Fig. 7.3 - 7.4. The numerical data obtained from different approaches converge very well to each other. However, it is necessary to emphasize that, to obtain the 100×100 points of PLMGF sampling data on the $X - Y$ plane, the direct spectral domain implementation consumes 1.5 hours. On the contrary, the compact split-field method only costs less than 5 seconds.

7.4.2 Case 2: Multi-Layer Nano Structure

After validating the PLMGF, the second case is designed to validate the proposed SEBI-PLMGF solver. Figure 7.5 shows the geometric structure of the problem. The lengths of the principal cell in the x and y directions are 100 nm and 100 nm,

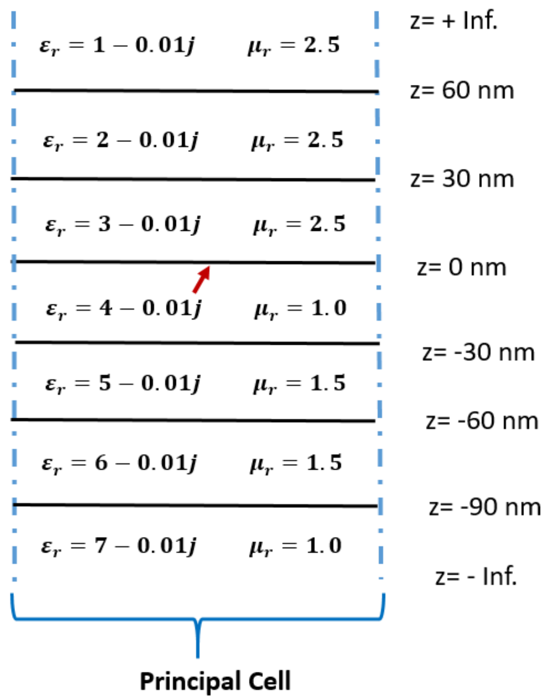

FIGURE 7.2: Geometrical structure of a typical multi-layer nano structure.

respectively. The nano particle above the layered medium is of the size 50 nm ×50 nm ×50 nm, and the whole structure is under TM_y with incident angle $\theta = 30^\circ$, $\phi = 20^\circ$ and wavelength of 400 nm.

The SEBI-PLMGF solver and the conventional SEBI-homogeneous Green's function solver are both used to simulate the same structure in Fig. 7.5. With the SEBI-PLMGF solver, the computation domain only contains the nano particle section. On the contrary, the SEBI-homogeneous Green's function solver needs to include the whole structure inside the computation domain, which considerably increases the number of unknowns.

Observing on the plane $z = 672.5$ nm, the electric field distribution is shown in Fig. 7.6. Furthermore, the electric fields along the middle lines parallel to x axis and y axis are obtained from both solvers. From Fig. 7.7, a satisfying match between two sets of results can be observed. Performing on an Intel 4-th generation i7

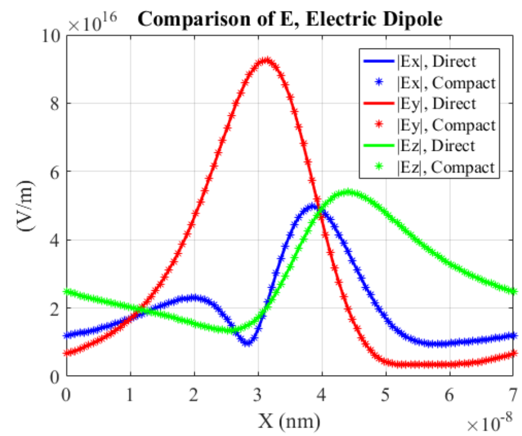

(a) Electric field comparison

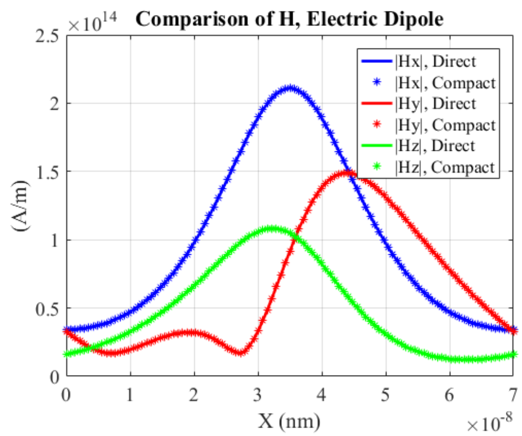

(b) Magnetic field comparison

FIGURE 7.3: Comparison between the compact split-field implementation of the PLMGF and the spectral domain direct implementation: (a) electric field generated by the electric dipole (b) magnetic field generated by the electric dipole.

CPU, the SEBI-PLMGF approach takes 27s and 1.2GB memory to solve the 13,872 unknowns, while the SEBI-homogeneous Green's function approach takes 59s and 4.5GB memory to solve the 72,800 unknowns. The processing work of meshing and discretization is not included in the time cost.

7.4.3 Case 3: p-Refinement Study

The major advantages of the proposed SEBI-PLMGF method includes two aspects. First, the layered medium background can be excluded from the computation do-

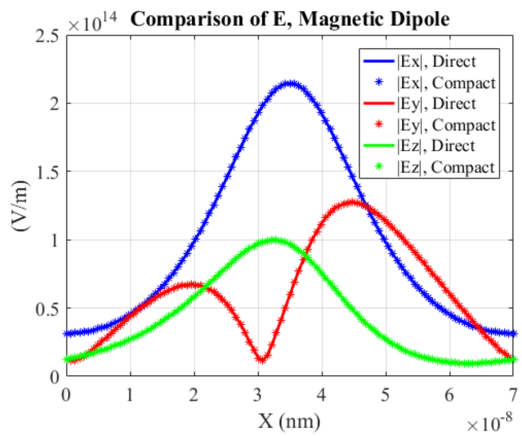

(a) Electric field comparison.

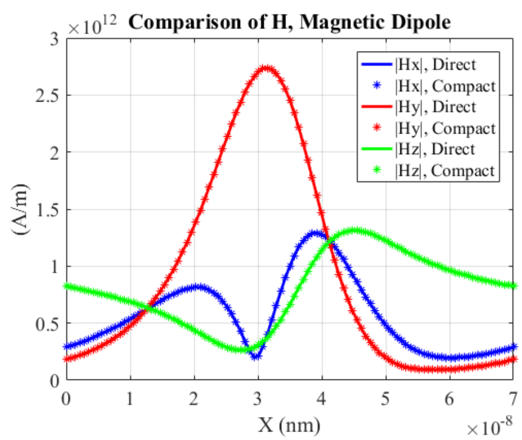

(b) Magnetic field comparison.

FIGURE 7.4: Comparison between the compact split-field implementation of the PLMGF and the spectral domain direct implementation: (a) electric field generated by the magnetic dipole (b) magnetic field generated by the magnetic dipole.

main. Only the fine structures of the principal cell need to be discretized. Second, the fast convergent GLL basis function is used to discretized both the interior computation domain and the boundary surfaces. In this section, several numerical examples are shown for the convergence performance of the SEBI-PLMGF.

As a commonly encountered issue in the conventional numerical methods, such as the finite element method, the finite-difference time-domain method, and the method of moments, the field singularities caused by the scatters' sharp corner usually considerably affects the convergence of the numerical results. To address this concern,

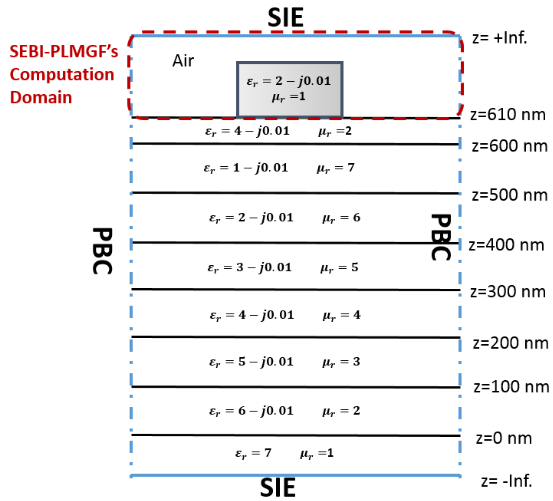

FIGURE 7.5: Geometrical structure of a typical multi-layer nano structure.

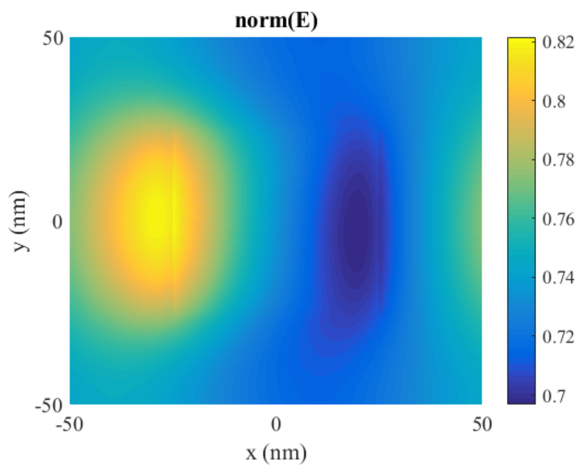

FIGURE 7.6: Electric field distribution observed at $z = 672.5$ nm.

the refinement study is performed on three categories of problems, separately.

The scattering structures that impact the convergence performance of the SEBI-PLMGF solver can be considered as three categories in general: the computation domain has geometries with (a) no field singularities, (b) moderate singularities, and (c) significant field singularities. Figure 7.8 provides a sketch of the first two scenarios, while the previous multi-layer nano structure case, is a good representative for the third situation.

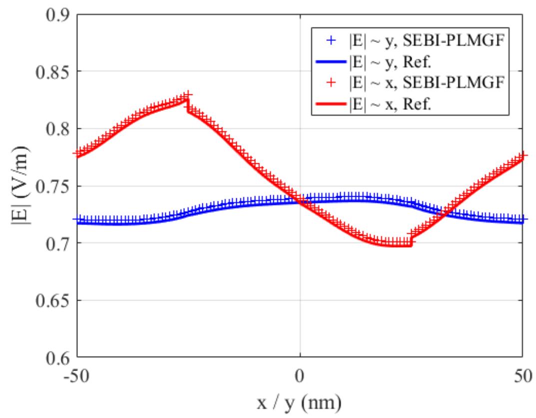

FIGURE 7.7: Validation of the electric field results. The electric field is observed along median lines of the $x-$ and $y-$ dimensions of the principal cell.

The p-refinement studies for all three situations are provided in Fig. 7.9. The A, B and C labels in the legends represent the computation model in Fig. 7.8a, Fig. 7.8b and Fig. 7.5, respectively. As expected, the field singularities exhibit an impact on the convergence performance at various levels. Usually singular fields will cause the convergence to be slower than exponential. The numerical results, however, converge on an exponential scale in all cases.

It should also be noted that the numerical accuracy is not purely determined by the GLL basis functions' order. Numerous factors, such as the mesh quality and the final linear equation system's condition number, also have an non-negligible contribution for a well-behaved outcome.

7.4.4 Case 4: 3-Dimensional Extreme Ultraviolet (EUV) Lithography

With the above validation and performance discussion, we extend the proposed solver to a more realistic example. The EUV lithography is among the most typical demands for large scale numerical analysis of scatterers embedded in stratified structures. The overall structure is usually electrically large as each principal cells extents to dozens of wavelength in each direction. On the other hand, the actual size of the lithography pattern only occupies a small fraction of the whole structure. This cat-

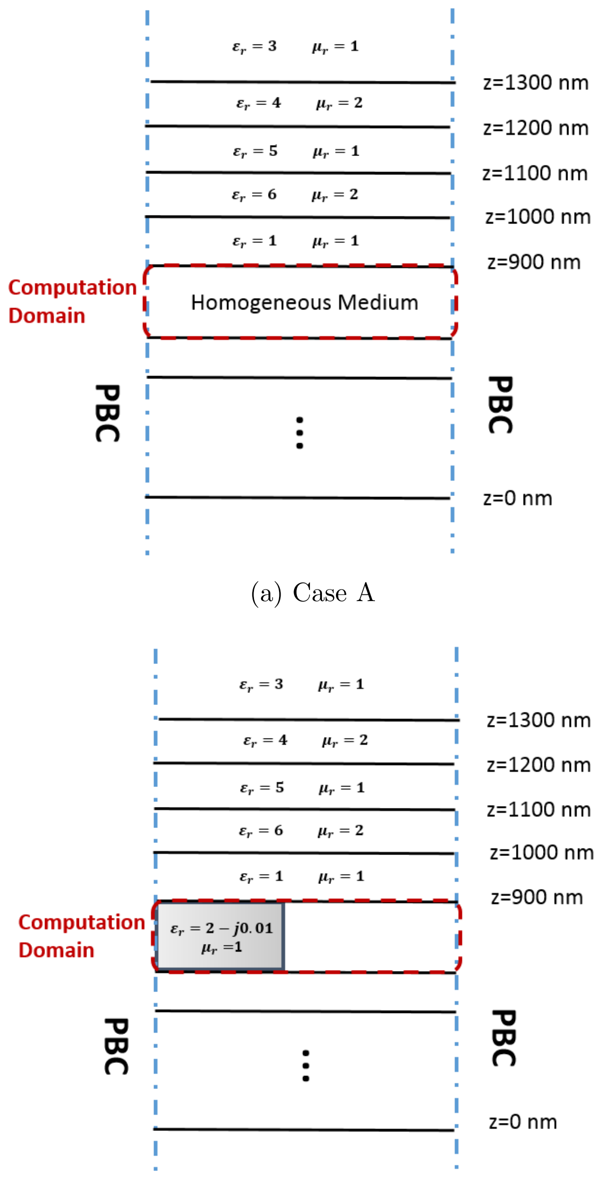

(a) Case A

(b) Case B

FIGURE 7.8: Typical structures impact the convergence performance. (a) The computation domain only contains scatterers with no field singularity corner. (b) The computation domain includes geometries for moderate field singularity. The layered medium structures below the computation domain are identical to that in Fig. 7.5.

egory of large and multiscale problems are challenging for conventional numerical solvers to reach a satisfying accuracy with reasonable resources costs.

Here a EUV lithography model of typical principal cell size is design for an illus-

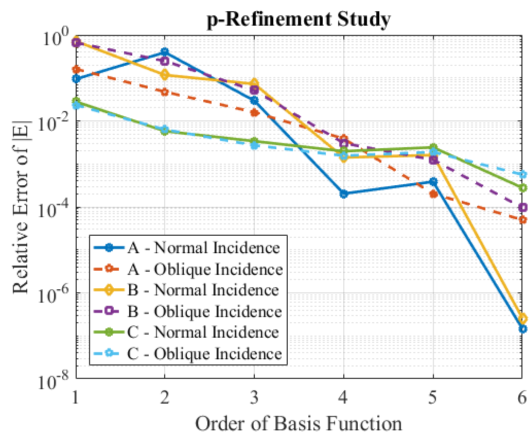

FIGURE 7.9: p-Refinement study for three typical scenarios.

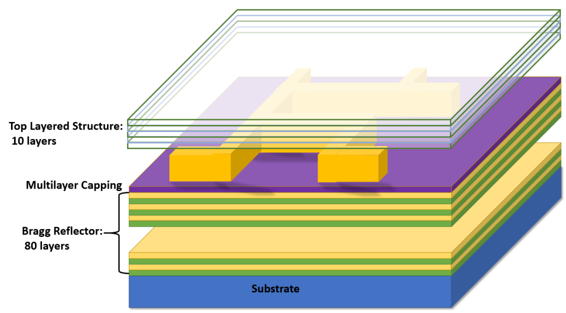

FIGURE 7.10: EUV lithography model.

tration. Figure 7.10 provides a systematic sketch of the lithography model. From top going downward, the materials and geometries are given as follows:

1. Vacuum layer (infinitely thick)

2. Top dielectric lens (5 bilayers, upper layer 3 nm-thick with $\epsilon_r = 0.998$; lower layer 2 nm-thick with $\epsilon_r = 0.854$)

3. Lithography filling background (thickness: 10 nm, $\epsilon_r = 0.958$)

4. Absorber capping (thickness: 12 nm, $\epsilon_r = 0.7497 - j0.0296$)

5. Lithography pattern (thickness: 27 nm, $\epsilon_r = 0.856 - j0.0807$)

6. Multilayer capping (thickness: 2.5 nm, $\epsilon_r = 0.75 - j0.0296$)

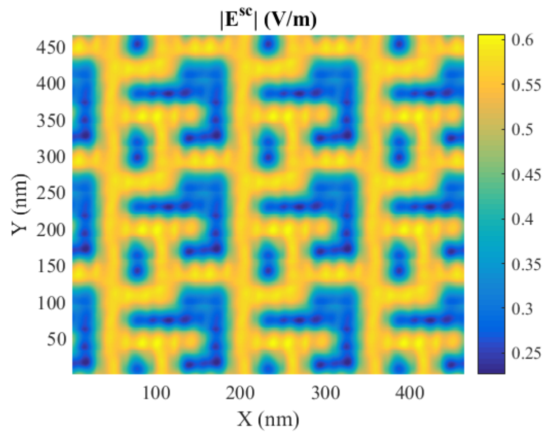

FIGURE 7.11: Electric field distribution observed one wavelength above the EUV lithography pattern.

7. Bragg reflector (40 silicon-molybdenum bilayers: Si layer thickness, 4.17 nm with $\epsilon_r = 0.998 - j0.00363$; Mo layer thickness, 2.78 nm with $\epsilon_r = 0.854 - j0.0119$)

8. Substrate (silicon, infinitely thick)

The x-y dimensions of each principal cell are 135 nm $\times$135 nm and the z dimension of the whole structure reaches to 336.5 nm. The structure is illuminated by $\lambda = 13.5$ nm TE_y plane wave from the top of the vacuum layer. With the conventional finite element method, the minimum computation domain is of the size $10\lambda \times 10\lambda \times 25\lambda$. Solving such an electrically large problem can be considerably challenging. However, within the SEBI-PLMGF framework, the computation domain only needs to cover the lithography pattern region of the principal cell, while both the layered structures in both top and bottom section are covered by the surface integral equations on the radiation boundaries.

Observing at one wavelength above the nano particle pattern, the scattered electric field distribution is shown in Fig. 7.11. The computation uses 265s with 12GB memory to solve the 52,638 unknowns.

Embedding in the same layered medium, a second large scale EUV lithography

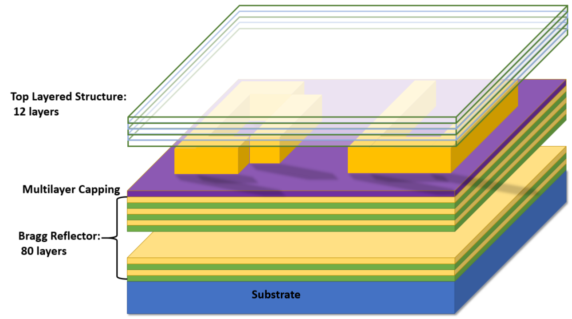

FIGURE 7.12: EUV lithography model.

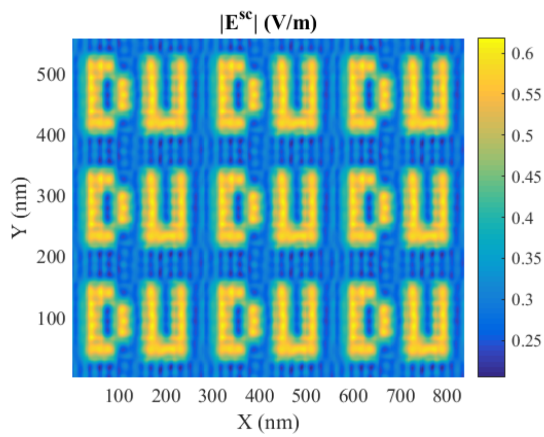

FIGURE 7.13: Electric field distribution observed one wavelength above the EUV lithography pattern.

pattern "DU" is simulated. Figure 7.12 provides the sketch of this EUV model. The x-y dimensions of each principal cell are 243 nm $\times$162 nm and the z dimension of the whole structure reaches to 336.5 nm. The structure is illuminated by λ = 13.5 nm TE_y plane wave from the top of the vacuum layer. With the conventional finite element method, the minimum computation domain is of the size $18\lambda \times 12\lambda \times 25\lambda$.

Observing at one wavelength above the nano particle pattern, the scattered electric field distribution is shown in Fig. 7.11. The computation uses 15 min with 20 GB memory to solve the 65,790 unknowns for a converged result. Compared with *Case 2*, the increased computational resources demand is caused by the lower sparsity ratio of the final equation system. The relatively large-scale boundary integral surface results in a dense MoM block matrices with high dimension. The conventional FEBI method, however, is expected to require over 20 million unknowns for the same problem. Solving the massive equation system with the even larger MoM block matrices require orders of magnitude additional resources.

7.5 Conclusion

A mixed-order spectral element - boundary integral method for periodic scatterers embedded in a layered medium is systematically developed in this chapter. Within the proposed SEBI-PLMGF framework, the minimum computation domain only contains the principal cell of the periodic scatterer. The layered medium background is described by a set of surface integral equations with the periodic layered medium dyadic Green's functions, while the periodic boundaries are truncated with the Floquet theorem. The GLL polynomials based spectral edge basis functions are used to discretize the whole computation domain. The matrix representation of the dyadic PLMGF is also systematically discussed. The primary and secondary terms of the PLMGF exhibits distinct analytical properties. By formulating them separately, the strong singularity of the PLMGF can be considerably relieved. The theoretical foundation for combining the Floquet theorem with the SEM is also revisited in the paper. Several numerical examples are presented to validate the formulation. The proposed framework is expected to be an efficient solution for the electromagnetic analysis in a broad class of applications, such as lithography, solar cell, metamaterial, and optoelectronic designs.

8

Domain Decomposition and Integrated Periodic/ Non-Periodic Modeling

8.1 Overview

By combining the dyadic layered medium Green's function together with the fast convergent SEBI method, the consumption of computational resources has already been reduced dramatically for multiscale nano optical computation. Formulating the boundary surface integral equations with the periodic Green's function, both homogeneous and layered medium background are removed from the computation domain. Further applying the Bloch periodic boundary condition to the lateral boundaries, only field unknowns of the inhomogeneous scatterers inside the principal cell need to be solved in the final equation system.

With the aforementioned improvements, the remaining demand of massive computation costs primarily originates from two perspectives. First, the inhomogeneous scatterer in each period of the structure might still remains electrically large. Second, in some cases, a large portion of the field unknowns remain on the boundary integral surfaces. This situation finally results in large scale dense MoM matrices, and the sparsity ratio of the global equation system thus decreases.

Moreover, noticing the periodic pattern structures commonly present in optical frequency designs, the Bloch periodic boundary condition is enforced in the SEBI solver in previous discussions. With this strategy, the only the unknowns in the principal cell need to be solved in the final equation system. This approximation is usually accurate enough for most quantitative analyses. However, simulating the whole structure as a finite model still can have its unique advantages for the investigation of certain physical properties, such as the nano antenna's far field radiation patterns and the edge effects of surface plasmonic metamaterials.

According to the above concerns, in this chapter another two improvements are proposed to further enhance the multiscale simulation of nano optical computations. First, the domain decomposition method (DDM) is developed for splitting the SEBI computation domain into multiple volume subdomains together with another boundary surface integral subdomain. Through this method, a large scale problem can be divided into multiple smaller problems less demanding in computational resources. Moreover, a scattered field hybrid radiation boundary condition is proposed to fully address the necessity of non-periodic simulations. By first formulating both the wave equation and the SIEs with scattered field unknowns, and then combining the perfectly matched layer (PML) with the surface integral equations (SIEs), the framework enables the SEBI solver switching between periodic and non-periodic modeling with the minimum cost.

8.2 Domain decomposition method in frequency-domain solver

The principle of the DDM is a typical design of the divide and conquer paradigm. Focusing on the source-field relation in each region at a time, the large scale problem is thus divided into multiple smaller problems that can be solved iteratively. Only one sub-problem needs to be focused at one time. Under the SEBI framework, the DDM is primarily applied to split the total degree of freedom (DoF) into several collections, where adjacent collections only couple through the DoF on the subdomain interfaces.

In our simulated configuration, the volume computation domain is divided into N non-overlapping subdomains, and the boundary integral surface domain is defined as the $(N+1)$ subdomain. Each subdomain only interacts with adjacent subdomains through the shared interfaces. The electromagnetic field in one subdomain propagates into the adjacent subdomains through the share interfaces. Thus, all regions couple together and behave as an equivalent description of the original problem. Noticing the volume subdomains are discretized and solved through the philosophy of the SEM, while the boundary integral surface domain is solved through the MoM. So overall, we denote the first N volume subdomain as SEM subdomains, and the $(N + 1)$ surface subdomain as the MoM subdomain. Adjacent subdomains can be discretized with non-conformal mesh for enhanced flexibility.

Theoretically, the electromagnetic fields on the subdomain interfaces satisfy the boundary condition for medium interfaces. However, previous research demonstrates that the direct enforcement of this tangential continuity boundary condition can not guarantee the convergence of the DDM solver. As an alternative, the Robin-type transmission condition has been proposed to describe the coupling between adjacent subdomains [Luo et al. (2013)]. Furthermore, recognizing the fact that in most nano optical modelings, the plane wave is considered as the illumination sources of the nano structure, the solver's convergence can be further improved through applying the Riemann-solver transmission condition on the subdomain interfaces. The Riemann solver models the transmission and reflection of the plane waves normally impinging on planar subdomain interfaces. According to our targeted problems, it serves as an efficient and sufficient solution.

Consider two adjacent subdomains coupled through the shared interfaces, the Riemann solver builds the relation between the electric/ magnetic field on the interface and the field quantities from these two subdomains. On the interface shared by the two subdomains with the index i and j, the Riemann solver shows:

$$
\begin{aligned}
(\hat{\mathbf{n}}_R \times \mathbf{E})(Y^{(i)} + Y^{(j)}) = \hat{\mathbf{n}}_R \times (&Y^{(i)}\mathbf{E}^{(i)} - Y_0 \cdot \hat{\mathbf{n}}_R \times \tilde{\mathbf{H}}^{(i)} \\
&+ Y^{(j)}\mathbf{E}^{(j)} + Y_0 \cdot \hat{\mathbf{n}}_R \times \tilde{\mathbf{H}}^{(j)})
\end{aligned}
\tag{8.1}
$$

$$
\begin{aligned}
(\hat{\mathbf{n}}_R \times \tilde{\mathbf{H}})(Z^{(i)} + Z^{(j)}) = \hat{\mathbf{n}}_R \times (&Z^{(i)}\tilde{\mathbf{H}}^{(i)} + Z_0 \cdot \hat{\mathbf{n}}_R \times \mathbf{E}^{(i)} \\
&+ Z^{(j)}\tilde{\mathbf{H}}^{(j)} - Z_0 \cdot \hat{\mathbf{n}}_R \times \mathbf{E}^{(j)})
\end{aligned}
\tag{8.2}
$$

where the superscripts (i) and (j) over the physical quantities denote the subdomain they refer to. $\hat{\mathbf{n}}_R$ is the unit normal vector pointing from the i-th subdomain to the j-th subdomain. $Z^{(i)} = \sqrt{\frac{\mu(\mathbf{r})}{\epsilon(\mathbf{r})}}$ is the position dependent wave impedance in the i-th subdomain; $Y^{(i)} = \frac{1}{Z^{(i)}}$ is the corresponding wave conductance. Equation 8.1 is referred as the electric field Riemann solver, while Eq. 8.2 is referred as the magnetic field Riemann solver.

Connecting adjacent subdomains through Eq. (8.1) - (8.2), the SEBI can be discretized and solved through the discontinuous Galerkin's method. Each subdomain can be meshed with non-conformal simplex elements.

8.3 Domain decomposition between MoM and SEM subdomain

The domain decomposition of the SEBI framework includes two categories of realizations: (1) Solving the coupled MoM - SEM subdomains. (2) Solving the coupled SEM - SEM subdomains. In this section, an initial investigation is proposed for the MoM - SEM subdomain coupling, where the boundary integral surfaces are divided from the volume computation domain as a single subdomain. The MoM subdomain is described by the the electric field integral equation (EFIE) and couples to the volume SEM subdomain through the magnetic field Riemann solver. Various discussions and enhancements can be further conducted based on this foundation, and we will take them as continuing endeavors.

For the boundary integral surfaces, the weak-form EFIE is given as

$$\begin{aligned} jk_0 \int_{\partial\Omega_i} (\hat{\mathbf{n}} \times \mathbf{\Phi_m})^T \cdot \mathbf{E}^{inc} dS = -jk_0 \int_{\partial\Omega_i} (\hat{\mathbf{n}} \times \mathbf{\Phi_m})^T \cdot \\ [-\mathbf{E}(\mathbf{r}) + \frac{1}{\eta_0} \mathcal{L}_E(\mathbf{r}, \tilde{\mathbf{J}}) + \mathcal{K}_E(\mathbf{r}, \mathbf{M})] dS. \end{aligned} \tag{8.3}$$

The MoM domain couples to the volume domain through the magnetic field Riemann solver. Apply the Galerkin's method to Eq. 8.2, we can arrive at

$$\begin{aligned} jk_0 \int_{\partial\Omega_i} \frac{1}{Z^{(i)} + Z^{(j)}} (\hat{\mathbf{n}}_R \times \mathbf{\Phi}_m)^T \cdot [-Z^{(j)} \cdot \tilde{\mathbf{H}}^{(i)} + Z_0 \cdot \hat{\mathbf{n}}_R \times \mathbf{E}^{(i)} + Z^{(j)} \cdot \tilde{\mathbf{H}}^{(j)} \\ -Z_0 \cdot \hat{\mathbf{n}}_R \times \mathbf{E}^{(j)}] dS = 0. \end{aligned} \tag{8.4}$$

where (i) denotes the MoM subdomain; (j) denotes the coupling adjacent SEM subdomain, and $\hat{\mathbf{n}} = -\hat{\mathbf{n}}_R$.

In the meantime, the coupled SEM subdomain can be solved through the wave equation combined with both the electric field Riemann solver and the magnetic field Riemann solver. The weak-form wave equation in the SEM subdomain is given in Eq. 7.1. Insert the magnetic field Riemann solver into the surface integral term of the weak-form wave equation, it arrives at:

$$\begin{aligned} \int_{\Omega_i} [(\nabla \times \mathbf{\Phi_m})^T \cdot \mu_r^{-1} \cdot (\nabla \times \mathbf{E}^{(i)}) - k_0^2 \cdot (\mathbf{\Phi_m})^T \cdot \epsilon_r \cdot \mathbf{E}^{(i)}] dV \\ +jk_0 \int_{\partial\Omega_i} \frac{(\hat{\mathbf{n}} \times \mathbf{\Phi}_m)^T}{Z^{(i)} + Z^{(j)}} \cdot [Z^{(i)} \cdot \tilde{\mathbf{H}}^{(i)} + Z_0 \cdot \hat{\mathbf{n}} \times \mathbf{E}^{(i)} + Z^{(j)} \cdot \tilde{\mathbf{H}}^{(j)} \\ -Z_0 \cdot \hat{\mathbf{n}} \times \mathbf{E}^{(j)}] dS = S_m^{(i)}. \end{aligned} \tag{8.5}$$

Applying the Galerkin's method to the electric field Riemann solver, we can obtain the other equation for the SEM subdomain:

$$
\begin{aligned}
jk_0 \int_{\partial\Omega_i} \frac{1}{Y^{(i)}+Y^{(j)}} (\hat{\mathbf{n}} \times \mathbf{\Phi}_m)^T \cdot [-Y^{(j)} \cdot \mathbf{E}^{(i)} - Y_0 \cdot \hat{\mathbf{n}} \times \tilde{\mathbf{H}}^{(i)} + Y^{(j)} \cdot \mathbf{E}^{(j)} \\
+Y_0 \cdot \hat{\mathbf{n}} \times \tilde{\mathbf{H}}^{(j)}]dS = 0.
\end{aligned}
\tag{8.6}
$$

where $\hat{\mathbf{n}} = \hat{\mathbf{n}}_R$.

Discretizing the unknown field quantities in both current subdomain and the adjacent coupling subdomain with the GLL basis functions:

$$
\mathbf{E}^{(i)} = \sum_{n_i} e^{(i)}_{n_i} \cdot \mathbf{\Phi}^{(i)}_{n_i} \tag{8.7}
$$

$$
\mathbf{E}^{(j)} = \sum_{n_j} e^{(j)}_{n_j} \cdot \mathbf{\Phi}^{(j)}_{n_j} \tag{8.8}
$$

$$
\tilde{\mathbf{H}}^{(i)} = \sum_{n_i} \tilde{h}^{(i)}_{n_i} \cdot \mathbf{\Phi}^{(i)}_{n_i} \tag{8.9}
$$

$$
\tilde{\mathbf{H}}^{(j)} = \sum_{n_j} \tilde{h}^{(j)}_{n_j} \cdot \mathbf{\Phi}^{(j)}_{n_j}, \tag{8.10}
$$

Eq. (8.4) - (8.5) reach to their linear equation system for the domain decomposition problem.

The global matrix system for SEBI-DDM can be obtained as

$$
\begin{bmatrix}
\mathbf{K_{II}} & \mathbf{K_{IS}} & \mathbf{0} & \mathbf{0} & \mathbf{0} \\
\mathbf{K_{SI}} & \mathbf{K_{SS}} + \mathbf{R^{Z}_{E,11}} & \mathbf{R^{Z}_{H,11}} & \mathbf{R^{Z}_{E,12}} & \mathbf{R^{Z}_{H,12}} \\
\mathbf{0} & \mathbf{R^{Y}_{E,11}} & \mathbf{R^{Y}_{H,11}} & \mathbf{R^{Y}_{E,12}} & \mathbf{R^{Y}_{H,12}} \\
\mathbf{0} & \mathbf{0} & \mathbf{0} & \mathbf{K^{E}_{E,22}} + \mathbf{MR_{E,22}} & \mathbf{L^{E}_{H,22}} \\
\mathbf{0} & \mathbf{R^{Z}_{E,21}} & \mathbf{R^{Z}_{H,21}} & \mathbf{R^{Z}_{E,22}} & \mathbf{R^{Z}_{H,22}}
\end{bmatrix}
\cdot
\begin{bmatrix}
\mathbf{E_I} \\ \mathbf{E_{S1}} \\ \tilde{\mathbf{H}}_{\mathbf{S1}} \\ \mathbf{E_{S2}} \\ \tilde{\mathbf{H}}_{\mathbf{S2}}
\end{bmatrix}
=
\begin{bmatrix}
\mathbf{S_e} \\ \mathbf{0} \\ \mathbf{0} \\ \mathbf{E^{inc}} \\ \mathbf{0}
\end{bmatrix}
\tag{8.11}
$$

where the first digit of the two-digit subscript denotes the location of the testing function; the second digit denotes the location of the basis function. The subscript 1 denotes the testing for basis function is on the Riemann boundary of the wave function subdomain; subscript 2 denotes it is on the Riemann boundary of the MoM subdomain.

Definitions of the block matrices in Eq. (8.11) are given below.

The block matrices $\mathbf{L^E}_{E,mn_i}$, $\mathbf{K^E}_{H,mn_i}$ and $\mathbf{MR}_{E,mn_i}$ are defined from the MoM equations. The definition of each block matrix is shown below.

$$\mathbf{L^E}_{E,mn_i}: \quad +jk_0 \int_{\partial\Omega_i} (\hat{\mathbf{n}} \times \mathbf{\Phi}_m)^T \cdot \frac{1}{\eta_0} \cdot \frac{Z_0}{Z^{(i)} + Z^{(j)}} \cdot \mathcal{L}_E(\mathbf{r}, \hat{\mathbf{n}} \times \hat{\mathbf{n}} \times \mathbf{\Phi}_{n_i}^{(i)}) dS \quad (8.12)$$

which corresponds to the term $\mathbf{L^E_{E,22}}$, i.e., the block matrix of $+jk_0 \int_{\partial\Omega_i} (\hat{\mathbf{n}} \times \mathbf{\Phi}_m)^T \cdot \frac{1}{\eta_0} \cdot \frac{Z_0}{Z^{(i)}+Z^{(j)}} \cdot \mathcal{L}_E(\mathbf{r}, \hat{\mathbf{n}} \times \hat{\mathbf{n}} \times \mathbf{E}^{(i)}) dS$.

$$\mathbf{K^E}_{H,mn_i}: \quad +jk_0 \int_{\partial\Omega_i} (\hat{\mathbf{n}} \times \mathbf{\Phi}_m)^T \cdot \frac{Y_0}{Y^{(i)} + Y^{(j)}} \cdot \mathcal{K}_E(\mathbf{r}, \hat{\mathbf{n}} \times \hat{\mathbf{n}} \times \mathbf{\Phi}_{n_i}^{(i)}) dS \quad (8.13)$$

which corresponds to the term $\mathbf{K^E_{H,22}}$, i.e., the block matrix of $+jk_0 \int_{\partial\Omega_i} (\hat{\mathbf{n}} \times \mathbf{\Phi}_m)^T \cdot \frac{Y_0}{Y^{(i)}+Y^{(j)}} \cdot \mathcal{K}_E(\mathbf{r}, \hat{\mathbf{n}} \times \hat{\mathbf{n}} \times \tilde{\mathbf{H}}^{(i)}) dS$.

and

$$\mathbf{MR}_{E,mn_i} = +jk_0 \int_{\partial\Omega_i} (\hat{\mathbf{n}} \times \mathbf{\Phi}_m)^T \cdot \mathbf{\Phi}_{n_i}^{(i)} dS, \quad (8.14)$$

which corresponds to the term $+jk_0 \int_{\partial\Omega_i} (\hat{\mathbf{n}} \times \mathbf{\Phi}_m)^T \cdot \mathbf{E}^{(i)} dS$.

The block matrices $\mathbf{R}^Z_{H,mn_i}$, $\mathbf{R}^Z_{E,mn_i}$, $\mathbf{R}^Z_{H,mn_j}$ and $\mathbf{R}^Z_{E,mn_j}$ are defined from the weak form magnetic field Riemann solver. The definition of each block matrix is given below.

$$\mathbf{R}^Z_{H,mn_i} = jk_0 \int_{\partial\Omega_i} \frac{Z^{(i)}}{Z^{(i)} + Z^{(j)}} \cdot [(\hat{\mathbf{n}} \times \mathbf{\Phi}_m)^T \cdot \mathbf{\Phi}_{n_i}^{(i)}] dS, \quad (8.15)$$

which corresponds to the term $jk_0 \int_{\partial\Omega_i} \frac{Z^{(i)}}{Z^{(i)}+Z^{(j)}} \cdot [(\hat{\mathbf{n}} \times \mathbf{\Phi}_m)^T \cdot \tilde{\mathbf{H}}^{(i)}] dS$.

$$\mathbf{R}^Z_{E,mn_i} = jk_0 \int_{\partial\Omega_i} \frac{Z_0}{Z^{(i)} + Z^{(j)}} \cdot [(\hat{\mathbf{n}} \times \mathbf{\Phi}_m)^T \cdot (\hat{\mathbf{n}} \times \mathbf{\Phi}^{(i)}_{n_i})] dS, \tag{8.16}$$

which corresponds to the term $jk_0 \int_{\partial\Omega_i} \frac{Z_0}{Z^{(i)}+Z^{(j)}} \cdot [(\hat{\mathbf{n}} \times \mathbf{\Phi}_m)^T \cdot (\hat{\mathbf{n}} \times \mathbf{E}^{(i)})] dS$.

$$\mathbf{R}^Z_{H,mn_j} = jk_0 \int_{\partial\Omega_i} \frac{Z^{(j)}}{Z^{(i)} + Z^{(j)}} \cdot [(\hat{\mathbf{n}} \times \mathbf{\Phi}_m)^T \cdot \mathbf{\Phi}^{(j)}_{n_j}] dS, \tag{8.17}$$

which corresponds to the term $jk_0 \int_{\partial\Omega_i} \frac{Z^{(j)}}{Z^{(i)}+Z^{(j)}} \cdot [(\hat{\mathbf{n}} \times \mathbf{\Phi}_m)^T \cdot \tilde{\mathbf{H}}^{(j)}] dS$.

$$\mathbf{R}^Z_{E,mn_j} = jk_0 \int_{\partial\Omega_i} -\frac{Z_0}{Z^{(i)} + Z^{(j)}} \cdot [(\hat{\mathbf{n}} \times \mathbf{\Phi}_m)^T \cdot (\hat{\mathbf{n}} \times \mathbf{\Phi}^{(j)}_{n_j})] dS, \tag{8.18}$$

which corresponds to the term $jk_0 \int_{\partial\Omega_i} -\frac{Z_0}{Z^{(i)}+Z^{(j)}} \cdot [(\hat{\mathbf{n}} \times \mathbf{\Phi}_m)^T \cdot (\hat{\mathbf{n}} \times \mathbf{E}^{(j)})] dS$.

The block matrices $\mathbf{R}^Y_{E,mn_i}$, $\mathbf{R}^Y_{H,mn_i}$, $\mathbf{R}^Y_{E,mn_j}$ and $\mathbf{R}^Y_{H,mn_j}$ are defined from the weak form electric field Riemann sovler. The definition of each block matrix is given below.

$$\mathbf{R}^Y_{E,mn_i} = jk_0 \int_{\partial\Omega_i} -\frac{Y^{(j)}}{Y^{(i)} + Y^{(j)}} [(\hat{\mathbf{n}} \times \mathbf{\Phi}_m)^T \cdot \mathbf{\Phi}^{(i)}_{n_i}] dS, \tag{8.19}$$

which corresponds to the term $jk_0 \int_{\partial\Omega_i} -\frac{Y^{(j)}}{Y^{(i)}+Y^{(j)}} [(\hat{\mathbf{n}} \times \mathbf{\Phi}_m)^T \cdot \mathbf{E}^{(i)}] dS$.

$$\mathbf{R}^Y_{H,mn_i} = jk_0 \int_{\partial\Omega_i} -\frac{Y_0}{Y^{(i)} + Y^{(j)}} [(\hat{\mathbf{n}} \times \mathbf{\Phi}_m)^T \cdot (\hat{\mathbf{n}} \times \mathbf{\Phi}^{(i)}_{n_i})] dS, \tag{8.20}$$

which corresponds to the term $jk_0 \int_{\partial\Omega_i} -\frac{Y_0}{Y^{(i)}+Y^{(j)}} [(\hat{\mathbf{n}} \times \mathbf{\Phi}_m)^T \cdot (\hat{\mathbf{n}} \times \tilde{\mathbf{H}}^{(i)})] dS$.

$$\mathbf{R}^Y_{E,mn_j} = jk_0 \int_{\partial\Omega_i} \frac{Y^{(j)}}{Y^{(i)} + Y^{(j)}} [(\hat{\mathbf{n}} \times \mathbf{\Phi}_m)^T \cdot \mathbf{\Phi}^{(j)}_{n_j}] dS, \tag{8.21}$$

which corresponds to the term $jk_0 \int_{\partial\Omega_i} \frac{Y^{(j)}}{Y^{(i)}+Y^{(j)}} [(\hat{\mathbf{n}} \times \mathbf{\Phi}_m)^T \cdot \mathbf{E}^{(j)}] dS$.

$$\mathbf{R}^{Y}_{H,mn_j} = jk_0 \int_{\partial\Omega_i} \frac{Y_0}{Y^{(i)} + Y^{(j)}} [(\hat{\mathbf{n}} \times \mathbf{\Phi}_m)^T \cdot (\hat{\mathbf{n}} \times \mathbf{\Phi}^{(j)}_{n_j})] dS, \tag{8.22}$$

which corresponds to the term $jk_0 \int_{\partial\Omega_i} \frac{Y_0}{Y^{(i)}+Y^{(j)}} [(\hat{\mathbf{n}} \times \mathbf{\Phi}_m)^T \cdot (\hat{\mathbf{n}} \times \tilde{\mathbf{H}}^{(j)})] dS$.

It is critical to keep in mind that, in Eq. (8.15) - (8.18), the unit normal vector can refer to either the normal vector of the volume subdomain region $\hat{\mathbf{n}}$ or that of the Riemann interface of the surface subdomain $\hat{\mathbf{n}}_R$.

Furthermore, the Cauchy principal integral needs to be applied to the primary terms in $\mathcal{K}$ operators. For the typical two scenarios, the following formulation can be used to extract the singularities:

$$< \hat{\mathbf{n}} \times \mathbf{\Phi}_i, \mathcal{K}_H, \hat{\mathbf{n}} \times \mathbf{\Phi}_j >=< \hat{\mathbf{n}} \times \mathbf{\Phi}_i, \tilde{\mathcal{K}}_H, \hat{\mathbf{n}} \times \mathbf{\Phi}_j > + \frac{1}{2} < \hat{\mathbf{n}} \times \mathbf{\Phi}_i, \mathbf{\Phi}_j > \tag{8.23}$$

and

$$< \hat{\mathbf{n}} \times \mathbf{\Phi}_i, \mathcal{K}_H, \hat{\mathbf{n}} \times \hat{\mathbf{n}} \times \mathbf{\Phi}_j >=< \hat{\mathbf{n}} \times \mathbf{\Phi}_i, \tilde{\mathcal{K}}_H, \hat{\mathbf{n}} \times \hat{\mathbf{n}} \times \mathbf{\Phi}_j > + \frac{1}{2} < \hat{\mathbf{n}} \times \mathbf{\Phi}_i, \hat{\mathbf{n}} \times \mathbf{\Phi}_j > . \tag{8.24}$$

The unknown in Eq. (8.11) can be obtained through any direct solver. However, to acknowledge the target of solving large scale optical problems with reduced computational resources, Eq.(8.11) can be reformulated as a set of coupled linear equation systems with smaller dimensions. Each derived equation system describes one subdomain, such that the overall problem can be solved iteratively.

For instance, the matrix-form equation of the SEM-MoM subdomain can be obtained as

$$\begin{bmatrix} \mathbf{K_{II}} & \mathbf{K_{IS}} & \mathbf{0} \\ \mathbf{K_{SI}} & \mathbf{K_{SS}} + \mathbf{R^{Z}_{E,11}} & \mathbf{R^{Z}_{H,11}} \\ \mathbf{0} & \mathbf{R^{Y}_{E,11}} & \mathbf{R^{Y}_{H,11}} \end{bmatrix} \cdot \begin{bmatrix} \mathbf{E_I} \\ \mathbf{E_{S1}} \\ \mathbf{\tilde{H}_{S1}} \end{bmatrix} = \begin{bmatrix} \mathbf{S_e} \\ -\mathbf{R^{Z}_{E,12}} \cdot \mathbf{E_{S2}} - \mathbf{R^{Z}_{H,12}} \cdot \mathbf{\tilde{H}_{S2}} \\ -\mathbf{R^{Y}_{E,12}} \cdot \mathbf{E_{S2}} - \mathbf{R^{Y}_{H,12}} \cdot \mathbf{\tilde{H}_{S2}} \end{bmatrix}. \tag{8.25}$$

Additionally, the matrix-form equation of the MoM-SEM subdomain is derived

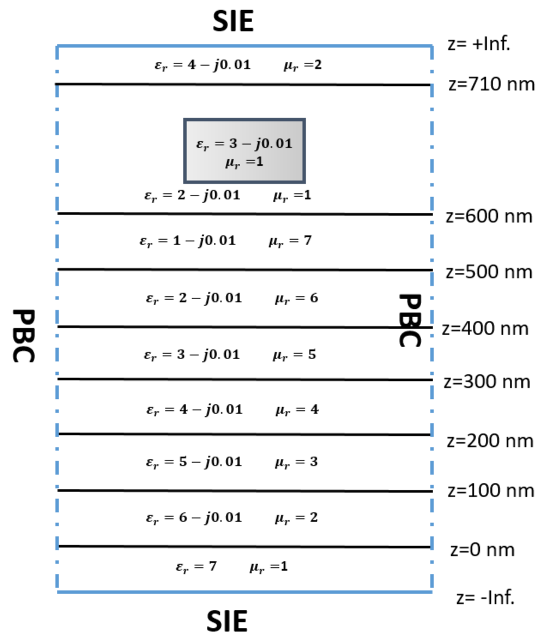

FIGURE 8.1: Geometrical structure of a typical multi-layer nano structure, for SEM-MoM DDM simulation.

as

$$\begin{bmatrix} \mathbf{K^E_{E,22}} + \mathbf{MR_{E,22}} & \mathbf{L^E_{H,22}} \\ \mathbf{R^Z_{E,22}} & \mathbf{R^Z_{H,22}} \end{bmatrix} \cdot \begin{bmatrix} \mathbf{E_{S2}} \\ \mathbf{\tilde{H}_{S2}} \end{bmatrix} = \begin{bmatrix} \mathbf{E^{inc}} \\ -\mathbf{R^Z_{E,21}} \cdot \mathbf{E_{S1}} - \mathbf{R^Z_{H,21}} \cdot \mathbf{\tilde{H}_{S1}} \end{bmatrix}. \tag{8.26}$$

Solving system of Eq. (8.25) - (8.26) iteratively, the unknowns in each subdomain can be obtained at converged results.

Through the above process, one can focus on solving a reduced size problem at one time. A more significant performance enhancement originates from the fact that the MoM related $\mathcal{L}$ and $\mathcal{K}$ block matrices are dense matrices. By decomposing the boundary integral surfaces as individual subdomains, we can solve the relatively small MoM region separately. The sparsity ratio in other subdomains thus will not be influenced by the surface integral equations.

As a typical numerical example, the MoM-SEM domain decomposition is applied to solve a multilayer model sketched in Fig. 8.1. The periodic structure is illuminated by a 350 nm TM_z plane wave.

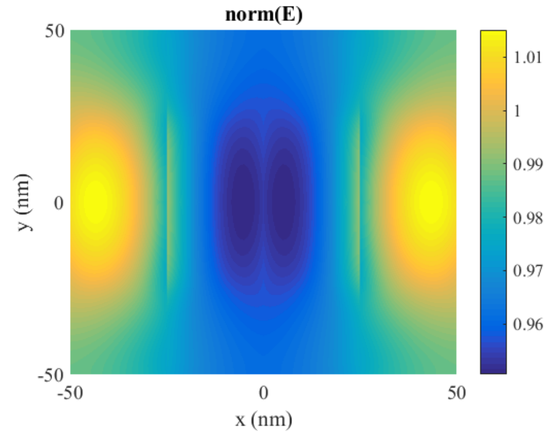

(a) Electric field pattern

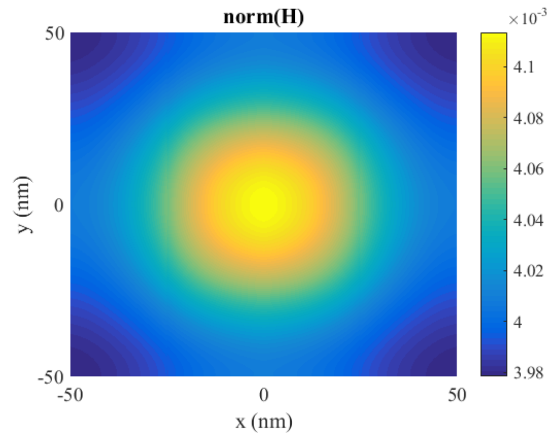

(b) Magnetic field pattern

FIGURE 8.2: Field distribution obtained from the SEM-MoM decomposition method.

Observing at the $z = 622.5$ nm plane, the numerical results obtained through the SEM-MoM domain decomposition method is shown in Fig. 8.2.

8.4 Domain decomposition between SEM and SEM subdomain

The Riemann solvers in Eq. (8.1) - (8.2) also describe the coupling between adjacent SEM subdomains. Typically, the unknowns in each subdomain can be solved via the combination of weak-form wave equation and the electric field and magnetic field Riemann solvers.

As a more general formulation for the DDM within the SEBI framework, here we consider the case where the boundary integral surface conformally combined with the wave equation domain, while the volume computation domain is decomposed into multiple subdomains. Compared with the pure SEM-SEM coupling, this situation requires more delicate implementation due to the existence of the boundary surface integral equations.

For each subdomain includes both boundary integral surface and domain decomposition interfaces, the governing equation can be obtained as

$$\begin{aligned}
&\int_V -(\nabla \times \mathbf{\Phi_m})^T \cdot \mu_r^{-1} \cdot (\nabla \times \mathbf{E}) dV + k_0^2 \int_V \mathbf{\Phi_m}^T \cdot \epsilon_r \cdot \mathbf{E} dV \\
&-jk_0 \int_{S_{BI}} (\hat{\mathbf{n}} \times \mathbf{\Phi_m})^T \cdot [\eta_0 \mathcal{L}_H(\mathbf{r}, \mathbf{M}) + \mathcal{K}_H(\mathbf{r}, \tilde{\mathbf{J}})] dS \\
&+jk_0 \int_{\partial\Omega_i} \frac{(\hat{\mathbf{n}_R} \times \mathbf{\Phi}_m)^T}{Z^{(i)} + Z^{(j)}} \cdot [Z^{(i)} \cdot \tilde{\mathbf{H}}^{(i)} + Z_0 \cdot \hat{\mathbf{n}_R} \times \mathbf{E}^{(i)} + Z^{(j)} \cdot \tilde{\mathbf{H}}^{(j)} - Z_0 \cdot \hat{\mathbf{n}_R} \times \mathbf{E}^{(j)}] dS \\
&= jk_0 \int_{S_{BI}} (\hat{\mathbf{n}} \times \mathbf{\Phi_m})^T \cdot \tilde{\mathbf{H}}^{inc} dS + \int_V \Phi_m^T \cdot \mathbf{S_e} dV
\end{aligned} \tag{8.27}$$

together with

$$\begin{aligned}
jk_0 \int_{S_{BI}} (\hat{\mathbf{n}} \times \mathbf{\Phi_m})^T \cdot \mathbf{E}^{inc} dS = -jk_0 \int_{S_{BI}} (\hat{\mathbf{n}} \times \mathbf{\Phi_m})^T \cdot \\
[-\mathbf{E}(\mathbf{r}) + \frac{1}{\eta_0} \mathcal{L}_E(\mathbf{r}, \tilde{\mathbf{J}}) + \mathcal{K}_E(\mathbf{r}, \mathbf{M})] dS.
\end{aligned} \tag{8.28}$$

and

$$\begin{aligned}
jk_0 \int_{\partial\Omega_i} \frac{1}{Y^{(i)} + Y^{(j)}} (\hat{\mathbf{n}_R} \times \mathbf{\Phi}_m)^T \cdot [-Y^{(j)} \cdot \mathbf{E}^{(i)} - Y_0 \cdot \hat{\mathbf{n}_R} \times \tilde{\mathbf{H}}^{(i)} + Y^{(j)} \cdot \mathbf{E}^{(j)} \\
+ Y_0 \cdot \hat{\mathbf{n}_R} \times \tilde{\mathbf{H}}^{(j)}] dS = 0.
\end{aligned} \tag{8.29}$$

where $\hat{\mathbf{n}}_R$ is the unit normal vector toward the corresponding mutual coupling subdomain; $\hat{\mathbf{n}}$ denotes the unit normal vector toward the exterior background region. The integral domain S_{BI} denotes the boundary integral surface, and $\partial\Omega_i$ denotes Riemann solver interfaces.

The above formulation can be more clearly illustrated through a two-subdomain scenario. Without loss of generality, we assume the upper volume subdomain includes the top boundary integral surface, and the lower volume subdomain includes the bottom boundary integral surface. Equation (8.27) - (8.29) thus can be discretized and assembled into a linear equation system:

$$\begin{bmatrix} \mathbf{M_1} & \mathbf{0} & \mathbf{0} & \mathbf{0} & \mathbf{0} & \mathbf{0} \\ \mathbf{K_{S_1I}} & \mathbf{K_{S_1S_1}} + \mathbf{R^Z_{E,11}} & \mathbf{R^Z_{H,11}} & \mathbf{0} & \mathbf{R^Z_{E,12}} & \mathbf{R^Z_{H,12}} \\ \mathbf{0} & \mathbf{R^Y_{E,11}} & \mathbf{R^Y_{H,11}} & \mathbf{0} & \mathbf{R^Y_{E,12}} & \mathbf{R^Y_{H,12}} \\ \mathbf{0} & \mathbf{0} & \mathbf{0} & \mathbf{M_2} & \mathbf{0} & \mathbf{0} \\ \mathbf{0} & \mathbf{R^Z_{E,21}} & \mathbf{R^Z_{H,21}} & \mathbf{K_{S_2I}} & \mathbf{K_{S_2S_2}} + \mathbf{R^Z_{E,22}} & \mathbf{R^Z_{H,22}} \\ \mathbf{0} & \mathbf{R^Y_{E,21}} & \mathbf{R^Y_{H,21}} & \mathbf{0} & \mathbf{R^Y_{E,22}} & \mathbf{R^Y_{H,22}} \end{bmatrix} \cdot \begin{bmatrix} \mathbf{X_1} \\ \mathbf{E_{S1}} \\ \tilde{\mathbf{H}}_{\mathbf{S1}} \\ \mathbf{X_2} \\ \mathbf{E_{S2}} \\ \tilde{\mathbf{H}}_{\mathbf{S2}} \end{bmatrix} = \begin{bmatrix} \mathbf{b_1} \\ \mathbf{0} \\ \mathbf{0} \\ \mathbf{b_2} \\ \mathbf{0} \\ \mathbf{0} \end{bmatrix} \tag{8.30}$$

where the subscript 1 denotes the index of the subdomains, and

$$\mathbf{M_i} = \begin{bmatrix} \mathbf{K_{II}} & \mathbf{K_{IS_{BI}}} & \mathbf{0} \\ \mathbf{K_{S_{BI}I}} & \mathbf{K_{S_{BI}S_{BI}}} + \mathbf{L_H} & \mathbf{K_H} \\ \mathbf{0} & \mathbf{K_E} & \mathbf{L_E} \end{bmatrix}, i = 1, 2; \tag{8.31}$$

$$\mathbf{X_i} = \begin{bmatrix} \mathbf{E_I} \\ \mathbf{E_{S_{BI}}} \\ \tilde{\mathbf{H}}_{\mathbf{S_{BI}}} \end{bmatrix}, i = 1, 2; \tag{8.32}$$

$$\mathbf{b_i} = \begin{bmatrix} \mathbf{S_e} \\ \tilde{\mathbf{H}}^{\mathbf{inc}}_{\mathbf{i}} \\ \mathbf{E}^{\mathbf{inc}}_{\mathbf{i}} \end{bmatrix}, i = 1, 2. \tag{8.33}$$

The above numerical framework can easily be extended as a general solution for large scale nano optical modelings. Through the decoupling on the Riemann boundary surfaces, Eq. (8.30) can be solved iteratively, so that the unknowns in each subdomain can be obtained with a moderate memory consumption.

For instance, for the volume subdomains with intersection between the boundary integral surfaces, the block matrix equation of the SEM-SEM coupling can be obtained as

$$\begin{bmatrix} \mathbf{M_1} & \mathbf{0} & \mathbf{0} \\ \mathbf{K_{S_1 I}} & \mathbf{K_{S_1 S_1}} + \mathbf{R^Z_{E,11}} & \mathbf{R^Z_{H,11}} \\ \mathbf{0} & \mathbf{R^Y_{E,11}} & \mathbf{R^Y_{H,11}} \end{bmatrix} \cdot \begin{bmatrix} \mathbf{X_1} \\ \mathbf{E_{S1}} \\ \tilde{\mathbf{H}}_{\mathbf{S1}} \end{bmatrix} = \begin{bmatrix} \mathbf{b_1} \\ -\mathbf{R^Z_{E,12}} \cdot \mathbf{E_{S2}} - \mathbf{R^Z_{H,12}} \cdot \tilde{\mathbf{H}}_{\mathbf{S2}} \\ -\mathbf{R^Y_{E,12}} \cdot \mathbf{E_{S2}} - \mathbf{R^Y_{H,12}} \cdot \tilde{\mathbf{H}}_{\mathbf{S2}} \end{bmatrix}. \tag{8.34}$$

In addition, the volume subdomain with no intersection between boundary integral surfaces can be formulated as

$$\begin{bmatrix} \mathbf{K_{II}} & \mathbf{K_{IS}} & \mathbf{0} \\ \mathbf{K_{SI}} & \mathbf{K_{SS}} + \mathbf{R^Z_{E,11}} & \mathbf{R^Z_{H,11}} \\ \mathbf{0} & \mathbf{R^Y_{E,11}} & \mathbf{R^Y_{H,11}} \end{bmatrix} \cdot \begin{bmatrix} \mathbf{E_I} \\ \mathbf{E_{S1}} \\ \tilde{\mathbf{H}}_{\mathbf{S1}} \end{bmatrix} = \begin{bmatrix} \mathbf{S_e} \\ -\mathbf{R^Z_{E,12}} \cdot \mathbf{E_{S2}} - \mathbf{R^Z_{H,12}} \cdot \tilde{\mathbf{H}}_{\mathbf{S2}} \\ -\mathbf{R^Y_{E,12}} \cdot \mathbf{E_{S2}} - \mathbf{R^Y_{H,12}} \cdot \tilde{\mathbf{H}}_{\mathbf{S2}} \end{bmatrix}. \tag{8.35}$$

Solving system of Eq. (8.34) - (8.35) iteratively, the unknowns in each subdomain can be obtained at converged results.

A typical numerical example is designed to illustrate and validate the proposed domain decomposition method in Fig. 8.3. To fully address of the capability of the discontinuous Galerkin's method enabled by the DDM, non-conformal mesh is applied to each subdomain as illustrated by Fig. 8.4.

The electric and magnetic field patterns observed at the $z = 647.5$ nm plane is shown in Fig. 8.5. The numerical results obtained through the discontinuous Galerkin domain decomposition SEBI method agrees well with the results obtained from the conformal SEBI-PLMGF method.

8.5 Integrated Periodic/ Non-Periodic Simulation

Through the investigations and discussions from Chapter 2 to the domain decomposition method proposed in the previous section, a multiscale SEBI solver has been proposed systematically for the nano optical computation. Considering the periodically patterned structures are frequently encountered in practical nano scale designs, the Bloch periodic boundary condition has been implemented to the SEBI framework for the reduced number of DoFs. The LMGF with double periodicity is further

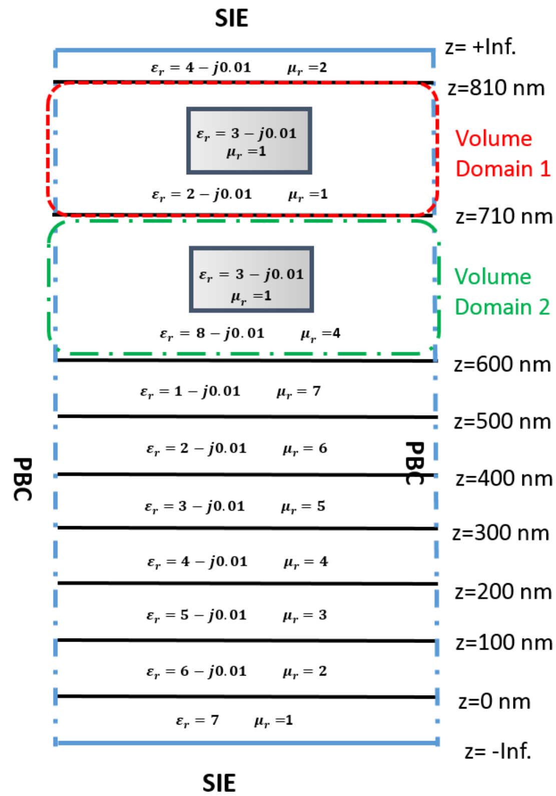

FIGURE 8.3: Geometrical structure of a typical multi-layer nano structure, for SEM-SEM DDM simulation.

studied within this context. Though the periodic SEBI solver delivers an satisfying accuracy for most applications of nano optical computations, however, it is still desirable to conduct the full size simulation without periodic approximation for the quantitative analyses of certain physical phenomena. For example, the nano structure with finite periods need to be simulated as a finite size model for the analysis of far field radiation pattern or the edge effects.

Conversely, the development and maintenance cost of developing a complete non-periodic solver is extremely high. For instance, the formulation and singularity extraction technique of the dyadic LMGF have to be re-investigated and implemented. The increased area of boundary integral surface may also considerably decreases the solver's performance. For the consideration of either the computational performance

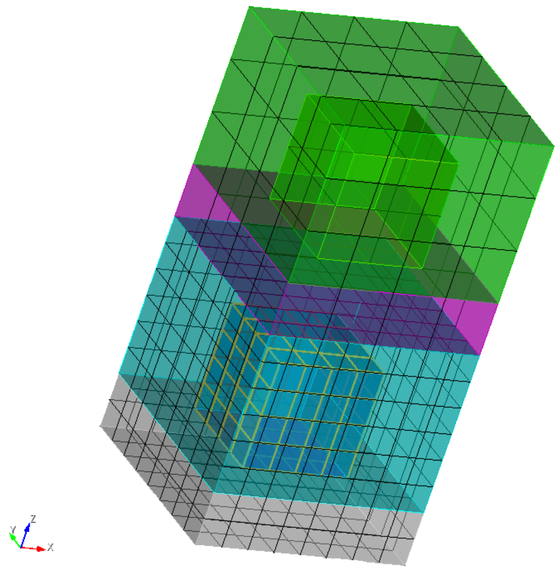

Figure 8.4: Illustration of non-conformal mesh with the discontinuous Galerkin's method, for the volume subdomains of the model sketch in Fig. 8.3.

or the practical resources cost, efficient integration of the periodic/ non-periodic simulation becomes a progress on demand.

In this section, we theoretically investigate a scattered field hybrid radiation boundary condition to integrate the periodic/ non-periodic simulations with minimum cost. To guarantee the robustness of the numerical solver, both the wave equation and the SIEs are first formulated with scattered field unknowns. Next, the PML and SIE are combined together as a full radiation boundary condition for non-periodic simulation. Under this framework, the SIEs still only cover the top and bottom boundary integral surfaces with the periodic Green's function. In addition, the Bloch periodic boundary condition is always enforced on the lateral surfaces. However, different from the previous SEBI framework, both the wave equation and the SIEs are formulated as the equations of scattered field unknowns. For non-periodic simulations, the all-direction radiation boundary condition can be realized by assembling the vertical PML to lateral surfaces.

The proposed method exhibits several significant advantages compared with con-

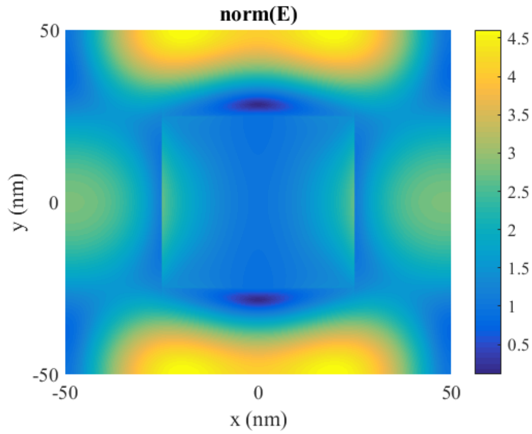

(a) Electric field pattern

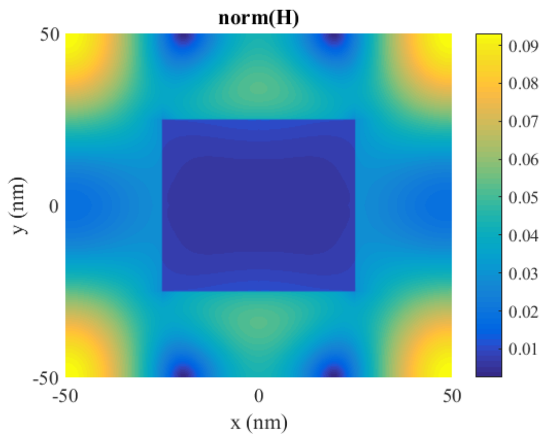

(b) Magnetic field pattern

FIGURE 8.5: Field distribution observed at the $z = 647.5$ nm plane.

ventional non-periodic SEBI or SEM with the PML. First, the periodic and non-periodic solvers are compactly integrated together. The maintenance cost is thus reduced by orders. Second, the conventional non-periodic SEBI includes a closed boundary integral surface surrounding the whole computation domain. This not only results in large scale dense block matrices in the equation system, but also heavily emphasize on the singularity extraction of the LMGF. In addition, the SEM with full PML cannot guarantee the accuracy under large oblique angle incidence. By using the SIEs as exact radiation boundary condition for top and bottom boundary surfaces, the proposed PML-SIE radiation boundary condition is expected with

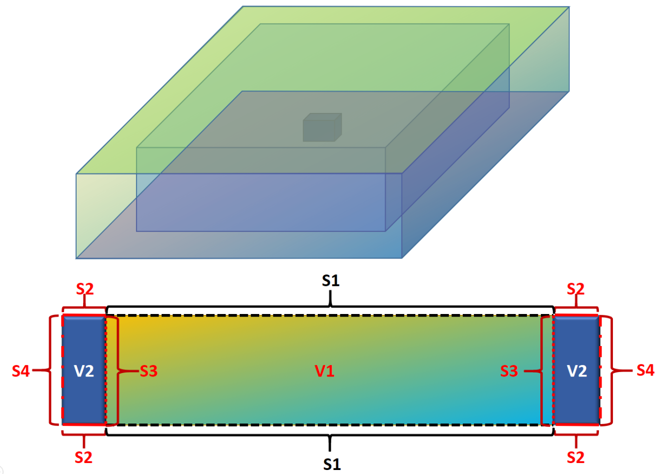

FIGURE 8.6: Sketch of the Integrated Periodic/ Non-Periodic Solver's Computation domain.

noticeable advantages for modeling scatterers with extensive horizontal dimensions.

Figure 8.6 shows the systematic sketch of the numerical framework. For non-periodic simulations, the physical domain V_1 is laterally surrounded by the scattered field domain V_2, which describes the interaction between the PML and the scattered fields. The surface boundaries S_1 and S_2 denotes the boundary integral surfaces of the physical domain and the scattered field domain, respectively. S_3 denotes the interface between the physical domain and the scattered field domain, while the Bloch periodic boundary condition is always applied to S_4.

Although the electromagnetic process inside the whole computation domain is governed by the vector wave equations, the physics interpretations differ considerably for the physical domain and the PML domain. For consistency and simplicity, all the physical domain, the PML domain, and the surface integral domain are formulated with scattered field wave equations. The universal weak-form vector wave equation can be obtained as

$$
\begin{aligned}
-\int_V (\nabla \times \mathbf{\Phi}_i)^T \cdot (\mu_r^{-1} \nabla \times \mathbf{E}^{sc}) dV + k_0^2 \int_V \mathbf{\Phi}_i^T \cdot \epsilon_r \cdot \mathbf{E}^{sc} dV \\
-jk_0 \int_S (\hat{\mathbf{n}} \times \mathbf{\Phi}_i)^T \cdot \tilde{\mathbf{H}}^{sc} dS = \int_{V_1} \mathbf{\Phi}_i^T \cdot \mathbf{S}_e dV + \\
\int_{V_1} \mathbf{\Phi}_i^T \cdot [\nabla \times (\mu_r^{-1} \nabla \times \mathbf{E}^{inc})] dV - k_0^2 \int_{V_1} \mathbf{\Phi}_i^T \cdot \epsilon_r \cdot \mathbf{E}^{inc} dV
\end{aligned}
\tag{8.36}
$$

where $V = V_1 + V_2$ denotes the whole computation domain; $S = S_1 + S_2 + S_4$ denotes the whole exterior boundaries of the computation domain.

To realize the hybrid absorbing boundary conditions, we first start from combining the boundary integral equations with the universal weak-form wave equation. Formulating the surface integral equations with the scattered fields, the scattered field EFIE and the scattered field MFIE can be obtained as

$$
\hat{\mathbf{n}} \times \mathbf{E}^{sc}(\mathbf{r}) = \hat{\mathbf{n}} \times [\frac{1}{\eta_0} \cdot \mathcal{L}_E(\mathbf{r}, \tilde{\mathbf{J}}^{sc}) + \mathcal{K}_E(\mathbf{r}, \mathbf{M}^{sc})] \tag{8.37}
$$

$$
\hat{\mathbf{n}} \times \tilde{\mathbf{H}}^{sc}(\mathbf{r}) = \hat{\mathbf{n}} \times [\eta_0 \cdot \mathcal{L}_H(\mathbf{r}, \mathbf{M}^{sc}) + \mathcal{K}_H(\mathbf{r}, \tilde{\mathbf{J}}^{sc})]. \tag{8.38}
$$

Insert Eq. (8.38) into Eq. (8.36), it arrives at

$$
\begin{aligned}
\int_V -(\nabla \times \mathbf{\Phi}_i)^T \cdot \mu_r^{-1} \cdot (\nabla \times \mathbf{E}^{sc}) dV + k_0^2 \int_V \mathbf{\Phi}_i^T \cdot \epsilon_r \cdot \mathbf{E}^{sc} dV \\
-jk_0 \int_{S_1+S_2} (\hat{\mathbf{n}} \times \mathbf{\Phi}_i)^T \cdot [\eta_0 \cdot \mathcal{L}_H(\mathbf{r}, \mathbf{M}^{sc}) + \mathcal{K}_H(\mathbf{r}, \tilde{\mathbf{J}}^{sc})] dS \\
-jk_0 \int_{S_4} (\hat{\mathbf{n}} \times \mathbf{\Phi}_i)^T \cdot \tilde{\mathbf{H}}^{sc} dS = -k_0^2 \int_{V1} \mathbf{\Phi}_i^T \cdot \epsilon_r \cdot \mathbf{E}^{inc} dV \\
+ \int_{V_1} \mathbf{\Phi}_i^T \cdot [\nabla \times (\mu_r^{-1} \nabla \times \mathbf{E}^{inc})] dV + \int_{V1} \mathbf{\Phi}_i^T \cdot \mathbf{S}_e dV
\end{aligned}
\tag{8.39}
$$

In addition, apply the Galerkin's method to Eq. (8.37), we have

$$
jk_0 \int_{S_1+S_2} (\hat{\mathbf{n}} \times \mathbf{\Phi}_i)^T \cdot [-\mathbf{E}^{sc}(\mathbf{r}) + \frac{1}{\eta_0} \cdot \mathcal{L}_E(\mathbf{r}, \tilde{\mathbf{J}}^{sc}) + \mathcal{K}_E(\mathbf{r}, \mathbf{M}^{sc})] dS = 0. \tag{8.40}
$$

Equations (8.39) - (8.40) combine the PML for the lateral boundary sides with the SIE's for the top and bottom boundaries. At this point, it should be realized that status of the PML's exterior boundaries alters fundamentally in the scheme of PML-SEBI. Although the surface integrals over $\mathbf{r}$ in Eq. (8.39) - (8.40) only cover the top and bottom radiation surfaces, the integral operators $\mathcal{L}_E$, $\mathcal{L}_H$, $\mathcal{K}_E$ and $\mathcal{K}_H$ still require a closed surface surrounding the computation domain. Improper boundary conditions on the surfaces exterior to the lateral PML domain may jeopardize the correctness of the SIE formulation and generate numerical errors from spurious modes. To guarantee the solver's robustness, the Bloch periodic boundary condition is applied to the lateral surfaces exterior to the PML domain. For the field unknowns of the periodic boundaries of the volume domains, we have

$$\mathbf{E}^{sc}(\mathbf{r}+\mathbf{a}) = \mathbf{E}^{sc}(\mathbf{r})e^{-j\mathbf{k}\cdot\mathbf{a}}, \tag{8.41}$$

and

$$\tilde{\mathbf{H}}^{sc}(\mathbf{r}+\mathbf{a}) = \tilde{\mathbf{H}}^{sc}(\mathbf{r})e^{-j\mathbf{k}\cdot\mathbf{a}}. \tag{8.42}$$

Through the above process, the restriction of homogeneous background can be largely relieved. Even with different homogeneous Green's functions for each boundary surface, the top and bottom backgrounds can be modeled as different materials. By discretizing the whole computation with mixed order GLL basis functions, a generalized layered structure, such as curved layers, are permitted in the physical and PML domains. The block-Thomas method is integrated for further performance enhancement.

The first case is designed for the validation of the PML-SEBI scheme. Consider a silica cube with side length 50 nm and $\epsilon_r = 2.4265$ placed in free space. The physical domain is illuminated by planar wave with wavelength $\lambda = 400$ nm. A set of 0.75λ thick PML covers the lateral boundaries of the physical domain. The observation line is placed on the top of the silica cube.

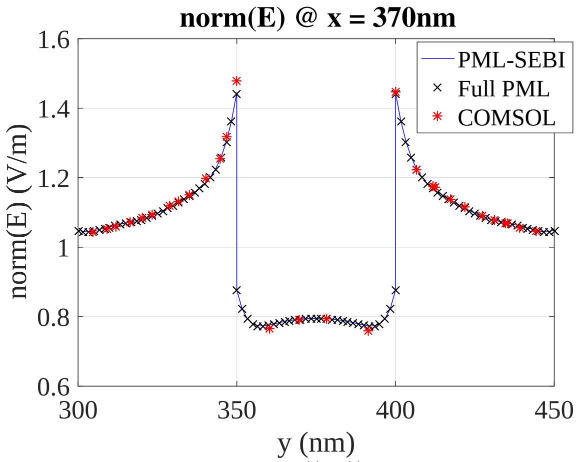

FIGURE 8.7: Case 1: Cubic scatterer. $||\mathbf{E}||$ by PML-SEBI, Full PML-SEM and COMSOL.

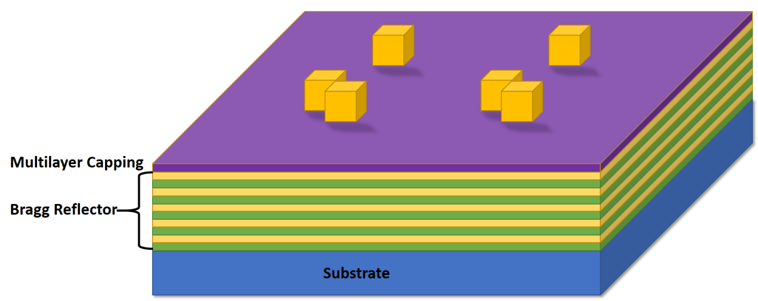

FIGURE 8.8: Case 2: EUV lithography model. Sketch of the simulation model.

Figure 8.7 provides the results from the proposed PML-SEBI solver, the full PML-SEM solver, and the commercial software COMSOL. To achieve a comparable accuracy, the memory and computation time cost of the PML-SEBI are 2.3 GB and 94 s, while those for the full PML-SEM are 15 GB and 890 s.

In the second numerical example, a typical EUV model is considered as a benchmark case. Figure 8.8 shows a sketch of the lithography model. From top to bottom the structure consists of a set of irregular absorbing gratings ($\epsilon_r = 0.8556 - 0.08075j$), a 3 nm multilayer capping ($\epsilon_r = 0.7497 - 0.0296j$), a Si/Mo Bragg reflector ($\epsilon_{r,Si} = 0.998 - 0.0036j, \epsilon_{r,Mo} = 0.8537 - 0.0119j$), and an infinitely thick Si substrate. The Bragg reflector includes 5 Si/Mo (2.78+4.17 nm) bilayers.

Table 8.1: Computational Resources Cost Comparison between the PML-SEBI and Full PML Frameworks for Non-periodic Simulations

Numerical Method	DoF	Time	Memory	Relative Error
Case 1				
PML-SEBI	23,750	94 s	2.3 GB	0.4%
SEM - full PML	94,325	890 s	15 GB	0.5%
Case 2				
PML-SEBI	373,248	120 min	72 GB	1.2%
SEM - full PML	425,736	149 min	83 GB	4.4%

As one of the advantages, the layered medium background can be addressed by truncating the top and bottom boundary integral surfaces with different Green's functions in the SEBI method. The physical domain is thus shrunk to be a slim space, electrically large in x and y dimensions, but thin in z-dimension. For the model shown in Fig. 8.8, the physical domain is of the size 7λ, 7λ, 4.3λ in x, y and z dimensions, respectively.

Table 8.1 shows the numerical performance comparison between the PML-SEBI method and the SEM - full PML approach for non-periodic simulation. The proposed SEBI with SIE-PML radiation boundary condition exhibits considerable improvement compared with the conventional full-PML scheme. The SEM - full PML exhibits relatively large numerical error when modeling scatterers large in horizontal dimensions while thin in the third direction. Its difficulty mainly originates from PML's decreased absorption of waves with large oblique incident angle.

8.6 Conclusions

In this chapter, the SEBI with domain decomposition is investigated for multiscale nano optical computation, and a scattered field hybrid radiation boundary condition is proposed for integrated periodic/ non-periodic simulation. By dividing the boundary integral surfaces from the volume computation domain, the small-scale dense MoM equation systems can be solved as one individual subdomain. As a result, the sparsity of the SEM subdomains can be maintained. By further dividing the volume domain into multiple SEM subdomains, electrically large modeling can be divided into multiple less challenging sub-problems with improved feasibility. Coupling adjacent subdomains with the Riemann solver transmission boundary condition,the solutions of all regions can be obtained through either direct solver or iterative solver.

The scattered field PML-SIE radiation boundary conditions compactly integrates the periodic and non-periodic SEBI solvers together. It not only minimizes the development and maintenance cost, but also exhibits improved accuracy and efficiency compared with conventional SEBI for finite scatterers or SEM with full PML. The performance enhancement is even more significant with the active computation domain large is horizontal dimensions while thin in the vertical dimension.

9

Conclusions and Future Work

9.1 Conclusions

A frequency domain multiscale SEBI method is proposed systematically for linear and nonlinear nano optical computation. Benefiting from the fast convergent SEM used for interior domain discretization and the surface integral equations served as the exact radiation boundary conditions, the SEBI solver provides excellent efficiency and flexibility. Through the enforcement of the Bloch periodic boundary condition and combining the periodic Green's functions, the computation domain for periodic structures are reduced to the principal cell only. Simultaneously, two-dimensional and three-dimensional simulations can be exactly performed with only one set of numerical solver.

Irregular and sub-wavelength scattering structures have been accurately analyzed. Significant advantages are validated through the comparison with mainstream industrial numerical tools. Nonlinear full-wave SEBI solver is developed self-consistently for higher harmonic generation problems. Nonlinear optical coupling processes ignored by most previous studies are thus can be quantitative analyzed.

The PLMGF is systematically formulated. Starting from the wave function formulation, the spectral domain representation is first discussed as a general implementation. To address the hyper singularity when both the source and the observations points are on the same layered medium interface, the PLMGF is first re-formulated into matrix-friendly formulation. The singularities are then successfully extracted with strong feasibility.

By further combining the PLMGF of the SEBI, the hybrid SEBI-PLMGF solver is validated to be an efficient solution for the common but challenging problems, where fine nano patterns are embedded in large scale layered medium. Within the context of SEBI, the primary and secondary terms of the PLMGF exhibits distinct analytical properties. By formulating them separately, the strong singularity of the PLMGF can be considerably relieved.

Moreover, the SEBI with domain decomposition is investigated for multiscale nano optical computation, and a scattered field PML-SIE radiation boundary condition is proposed for integrated periodic/ non-periodic simulation.

9.2 Original Contributions

Main contributions in this work are summarized as follows.

1. The development of periodic mixed-order SEBI solver for Helmholtz wave equation, particularly focuses on nano scale applications. Structured hexahedral mesh with additional interpolation degree is used to model the irregular curved edge geometries.

2. Extending the SEBI solver for the quantitative analysis of the third harmonic generation. Based on this tool, graphene's third harmonic characteristics under strong surface plasmonic resonances are investigated.

3. Systematic discussion and derivation of the PLMGF in spatial and spectral domain implementation, including both regular wave function formulation and matrix-friendly formulation. A novel and feasible singularity extraction technique is proposed under the matrix-friendly formulation.

4. The development of a multiscale solver combining the SEBI and the PLMGF. It is validated as a robust and powerful solution for inhomogeneous scatteres embedded in large scale layered medium.

5. Theoretical investigations of the domain decomposition with Riemann solver under the SEBI framework.

6. Development of the scattered field PML-SIE radiation boundary condition, which maximally integrates the periodic and non-periodic solver.

7. With the advantages of the developed and proposed numerical algorithms, additional research are accomplished on graphene's light absorption engineering around the visible spectra, and the EUV multilayer defects analysis.

9.3 Future Work

Several promising and important aspects could be investigated in detail based on this work. Some of them have already been on active research and are needed to make the SEBI method more efficient for solving practical problems.

- Spectral integral method acceleration for the MoM - SEM domain decomposition
- Bloch-Thomas direct solver for the SEBI with planar domain decomposition
- Adaptive refinement with hierarchical basis functions
- Periodic boundary condition realization based on the Riemann solvers

- Eigenvalue solver for dispersive and anisotropic periodic structures

Bibliography

Ahmed, I., Khoo, E. H., and Li, E. (2013), "Efficient Modeling and Simulation of Graphene Devices With the LOD-FDTD Method," *IEEE Microwave and Wireless Components Letters*, 23, 306–308.

Amano, T., Iida, S., Hirano, R., Terasawa, T., Watanabe, H., and Inazuki, Y. (2012), "Residual-type mask defect printability for extreme ultraviolet lithography," *Journal of Vacuum Science and Technology B*, 30.

Badger, K. D., Qi, Z. J., Gallagher, E., Seki, K., and McIntyre, G. (2012), "Illuminating EUVL mask defect printability," .

Bao, Q. and Loh, K. P. (2012), "Graphene Photonics, Plasmonics, and Broadband Optoelectronic Devices," *ACS Nano*, 6, 3677–3694, PMID: 22512399.

Bonaccorso, F., Sun, Z., Hasan, T., and Ferrari, A. C. (2010), "Graphene photonics and optoelectronics," *Nature Photonics*, 4, 611 – 622.

Botha, M. and Jin, J.-M. (2004), "On the variational formulation of hybrid finite element-boundary integral techniques for electromagnetic analysis," *Antennas and Propagation, IEEE Transactions on*, 52, 3037–3047.

Bruna, M. and Borini, S. (2009), "Optical constants of graphene layers in the visible range," *Applied Physics Letters*, 94, –.

Chen, C. and Hone, J. (2013), "Graphene nanoelectromechanical systems," *Proceedings of the IEEE*, 101, 1766–1779.

Chen, J., Tobon, L., Chai, M., Mix, J., and Liu, Q. H. (2011a), "Efficient Implicit-Explicit Time Stepping Scheme With Domain Decomposition for Multiscale Modeling of Layered Structures," *IEEE Trans. Components, Packaging and Manufacturing Technology*, 1, 1438–1446.

Chen, K., Song, J., and Kamgaing, T. (2015), "Accurate and Efficient Computation of Layered Medium Doubly Periodic Green's Function in Matrix-Friendly Formulation," *IEEE Transactions on Antennas and Propagation*, 63, 809–813.

Chen, Y. P., Xiong, J. L., and Chew, W. C. (2011b), "A Mixed-Form Thin-Stratified Medium Fast-Multipole Algorithm for Both Low and Mid-Frequency Problems," *IEEE Transactions on Antennas and Propagation*, 59, 2341–2349.

Chen, Y. P., Chew, W. C., and Jiang, L. (2012), "A New Green's Function Formulation for Modeling Homogeneous Objects in Layered Medium," *IEEE Transactions on Antennas and Propagation*, 60, 4766–4776.

Chew, W. C., Xiong, J. L., and Saville, M. A. (2006), "A Matrix-Friendly Formulation of Layered Medium Green's Function," *IEEE Antennas and Wireless Propagation Letters*, 5, 490–494.

Collins, J. D., Jin, J. M., and Volakis, J. L. (1992), "Eliminating interior resonances in finite element-boundary integral methods for scattering," *IEEE Transactions on Antennas and Propagation*, 40, 1583–1585.

Echtermeyer, T. J., Britnell, L., Jasnos, P. K., Lombardo, A., Gorbachev, R. V., Grigorenko, A. N., Geim, A. K., Ferrari, A. C., and Novoselov, K. S. (2011), "Strong plasmonic enhancement of photovoltage in graphene," *Nature Communications*, 2, 458–462.

Evanschitzky, P., Erdmann, A., Besacier, M., and Schiavone, P. (2003), "Simulation of extreme ultraviolet masks with defective multilayers," .

Fang, Z., Liu, Z., Wang, Y., Ajayan, P. M., Nordlander, P., and Halas, N. J. (2012), "Graphene-Antenna Sandwich Photodetector," *Nano Letters*, 12, 3808–3813, PMID: 22703522.

Feigl, T., Yulin, S., Benoit, N., and Kaiser, N. (2006), "EUV Multilayer Optics," *Microelectron. Eng.*, 83, 703–706.

Grigorenko, A. N., Polini, M., and Novoselov, K. (2012), "Graphene plasmonics," *Nature Photonics*, 6, 749–758.

Hendry, E., Hale, P. J., Moger, J., Savchenko, A. K., and Mikhailov, S. A. (2010), "Coherent Nonlinear Optical Response of Graphene," *Phys. Rev. Lett.*, 105, 097401.

Hong, S.-Y., Dadap, J. I., Petrone, N., Yeh, P.-C., Hone, J., and Osgood, R. M. (2013), "Optical Third-Harmonic Generation in Graphene," *Phys. Rev. X*, 3, 021014.

Hu, F. Q. (1995), "A Spectral Boundary Integral Equation Method for the 2D Helmholtz Equation," *Journal of Computational Physics*, 120, 340 – 347.

Jin, J. (2014), *The Finite Element Method in Electromagnetics*, Wiley-IEEE Press, 3rd edn.

Kauranen, M. and Zayats, V. A. (2012), “Nonlinear plasmonics,” *Nature Photonics*, 6, 737–748.

Krautschik, C. G. and Nishiyama, I. (2003), “Printability of opaque and clear phase defects using the finite-difference time-domain (FDTD) method,” .

Kumar, N., Kumar, J., Gerstenkorn, C., Wang, R., Chiu, H.-Y., Smirl, A. L., and Zhao, H. (2013), “Third harmonic generation in graphene and few-layer graphite films,” *Phys. Rev. B*, 87, 121406.

Kwon, H. J., Harris-Jones, J., Cordes, A., Satake, M., Li, Y., Mochi, I., and Goldberg, K. A. (2012), “EUV mask multilayer defects and their printability under different multilayer deposition conditions,” .

Lee, J.-H. and Liu, Q. H. (2005), “An efficient 3-D spectral-element method for Schr ouml;dinger equation in nanodevice simulation,” *Computer-Aided Design of Integrated Circuits and Systems, IEEE Transactions on*, 24, 1848–1858.

Lee, J.-H., Xiao, T., and Liu, Q. (2006), “A 3-D spectral-element method using mixed-order curl conforming vector basis functions for electromagnetic fields,” *Microwave Theory and Techniques, IEEE Transactions on*, 54, 437–444.

Lee, J. H., Chen, J., and Liu, Q. H. (2009), “A 3-D Discontinuous Spectral Element Time-Domain Method for Maxwell's Equations,” *IEEE Transactions on Antennas and Propagation*, 57, 2666–2674.

Li, H., Anugrah, Y., Koester, S. J., and Li, M. (2012a), “Optical absorption in graphene integrated on silicon waveguides,” *Applied Physics Letters*, 101, –.

Li, Y., Peng, D., Satake, M., and Hu, P. (2012b), “A fast approach to model EUV mask 3D and shadowing effects,” .

Lin, H., Pantoja, M. F., Angulo, L. D., Alvarez, J., Martin, R. G., and Garcia, S. G. (2012), “FDTD Modeling of Graphene Devices Using Complex Conjugate Dispersion Material Model,” *IEEE Microwave and Wireless Components Letters*, 22, 612–614.

Liu, Y., Cheng, R., Liao, L., Zhou, H., Bai, J., Liu, G., Liu, L., Huang, Y., and Duan, X. (2011), “Plasmon resonance enhanced multicolour photodetection by graphene,” *Nature Communications*, 2.

Luo, M. (2013), “Spectral Element Method Simulation of Linear and Nonlinear Electromagnetic Field in Semiconductor Nanostructures,” Ph.D. thesis, Duke University.

Luo, M. and Liu, Q. H. (2009), “Spectral element method for band structures of three-dimensional anisotropic photonic crystals,” *Phys. Rev. E*, 80, 056702.

Luo, M. and Liu, Q. H. (2011), "Extraordinary transmission of a thick film with a periodic structure consisting of strongly dispersive materials," *J. Opt. Soc. Am. B*, 28, 629–636.

Luo, M., Liu, Q. H., and Guo, J. (2010), "A spectral element method calculation of extraordinary light transmission through periodic subwavelength slits," *J. Opt. Soc. Am. B*, 27, 560–566.

Luo, M., Lin, Y., and Liu, Q. H. (2013), "Spectral Methods and Domain Decomposition for Nanophotonic Applications," *Proceedings of the IEEE*, 101, 473–483.

Meurant, G. (1992), "A Review on the Inverse of Symmetric Tridiagonal and Block Tridiagonal Matrices," *SIAM Journal on Matrix Analysis and Applications*, 13, 707–728.

Mikhailov, S. A. (2011), "Theory of the giant plasmon-enhanced second-harmonic generation in graphene and semiconductor two-dimensional electron systems," *Phys. Rev. B*, 84, 045432.

Mikhailov, S. A. (2014), "Quantum theory of third-harmonic generation in graphene," *Phys. Rev. B*, 90, 241301.

Nair, R. R., Blake, P., Grigorenko, A. N., Novoselov, K. S., Booth, T. J., Stauber, T., Peres, N. M. R., and Geim, A. K. (2008), "Fine Structure Constant Defines Visual Transparency of Graphene," *Science*, 320, 1308.

Nicolet, A., Guenneau, S., Geuzaine, C., and Zolla, F. (2004), "Modelling of electromagnetic waves in periodic media with finite elements," *Journal of Computational and Applied Mathematics*, 168, 321 – 329, Selected Papers from the Second International Conference on Advanced Computational Methods in Engineering (ACOMEN 2002).

Nikolaenko, A. E., Papasimakis, N., Atmatzakis, E., Luo, Z., Shen, Z. X., De Angelis, F., Boden, S. A., Di Fabrizio, E., and Zheludev, N. I. (2012), "Nonlinear graphene metamaterial," *Applied Physics Letters*, 100, –.

Niu, J., Luo, M., Fang, Y., and Liu, Q. H. (2014), "Boundary integral spectral element method analyses of extreme ultraviolet multilayer defects," *J. Opt. Soc. Am. A*, 31, 2203–2209.

Niu, J., Luo, M., Zhu, J., and Liu, Q. H. (2015), "Enhanced plasmonic light absorption engineering of graphene: simulation by boundary-integral spectral element method," *Opt. Express*, 23, 4539–4551.

Niu, J., Luo, M., and Liu, Q. H. (2016), "Enhancement of graphene's third-harmonic generation with localized surface plasmon resonance under optical/electro-optic Kerr effects," *J. Opt. Soc. Am. B*, 33, 615–621.

Peng, D., Li, Y., Satake, M., Hu, P., Chen, J., Hsu, S. C., Lai, R., Lin, C. S., and Tuo, L. C. C. (2012), "AIMS D2DB simulation for DUV and EUV mask inspection," .

Peres, N. M. R. and Bludov, Y. V. (2013), "Enhancing the absorption of graphene in the terahertz range," *EPL (Europhysics Letters)*, 101, 58002.

Pomplun, J., Burger, S., Schmidt, F., Zschiedrich, L., Scholze, F., Laubis, C., and Dersch, U. (2006), "Rigorous FEM simulation of EUV masks: influence of shape and material parameters," .

Pomplun, J., Burger, S., Zschiedrich, L., and Schmidt, F. (2007a), "Adaptive finite element method for simulation of optical nano structures," *physica status solidi (b)*, 244, 3419–3434.

Pomplun, J., Burger, S., Schmidt, F., Scholze, F., Laubis, C., and Dersch, U. (2007b), "Finite element analysis of EUV lithography," .

Ren, Y., Liu, Q. H., and Chen, Y. P. (2016), "A Hybrid FEM/MoM Method for 3-D Electromagnetic Scattering in Layered Medium," *IEEE Transactions on Antennas and Propagation*, 64, 3487–3495.

Ren, Y., Huang, W. F., Niu, J., and Liu, Q. H. (2017), "A Hybrid Solver Based on Domain Decomposition Method for the Composite Scattering in Layered Medium," *IEEE Antennas and Wireless Propagation Letters*, 16, 420–423.

Saitoh, K. and Koshiba, M. (2001), "Full-Vectorial Finite Element Beam Propagation Method with Perfectly Matched Layers for Anisotropic Optical Waveguides," *J. Lightwave Technol.*, 19, 405.

Sámson, Z. L., Horak, P., MacDonald, K. F., and Zheludev, N. I. (2011), "Femtosecond surface plasmon pulse propagation," *Opt. Lett.*, 36, 250–252.

Schiavone, P., Granet, G., and Robic, J. (2001), "Rigorous electromagnetic simulation of {EUV} masks: influence of the absorber properties," *Microelectronic Engineering*, 5758, 497 – 503, Micro- and Nano-Engineering 2000.

Shanker, B., Ergin, A. A., Aygun, K., and Michielssen, E. (2000), "Analysis of transient electromagnetic scattering from closed surfaces using a combined field integral equation," *IEEE Transactions on Antennas and Propagation*, 48, 1064–1074.

Shubair, R. M. and Chow, Y. L. (1993), "Efficient computation of the periodic Green's function in layered dielectric media," *IEEE Transactions on Microwave Theory and Techniques*, 41, 498–502.

Simsek, E., Liu, J., and Liu, Q. H. (2006), "A Spectral Integral Method and Hybrid SIM/FEM for Layered Media," *IEEE Transactions on Microwave Theory and Techniques*, 54, 3878–3884.

Smaali, R., Besacier, M., and Schiavone, P. (2006), "Three-dimensional rigorous simulation of EUV defective masks using modal method by Fourier expansion," .

Thongrattanasiri, S., Koppens, F. H. L., and García de Abajo, F. J. (2012), "Complete Optical Absorption in Periodically Patterned Graphene," *Phys. Rev. Lett.*, 108, 047401.

Urbanski, L., Isoyan, A., Stein, A., Rocca, J. J., Menoni, C. S., and Marconi, M. C. (2012), "Defect-tolerant extreme ultraviolet nanoscale printing," *Opt. Lett.*, 37, 3633–3635.

Vakil, A. and Engheta, N. (2011), "Transformation Optics Using Graphene," *Science*, 332, 1291–1294.

Vasko, F. T. (2010), "Saturation of interband absorption in graphene," *Phys. Rev. B*, 82, 245422.

Vincenti, M. A., de Ceglia, D., Grande, M., D'Orazio, A., and Scalora, M. (2014), "Third-harmonic generation in one-dimensional photonic crystal with graphene-based defect," *Phys. Rev. B*, 89, 165139.

Vouvakis, M. N., Lee, S.-C., Zhao, K., and Lee, J.-F. (2004), "A symmetric FEM-IE formulation with a single-level IE-QR algorithm for solving electromagnetic radiation and scattering problems," *IEEE Transactions on Antennas and Propagation*, 52, 3060–3070.

Wang, F., Zhang, Y., Tian, C., Girit, C., Zettl, A., Crommie, M., and Shen, Y. R. (2008), "Gate-Variable Optical Transitions in Graphene," *Science*, 320, 206–209.

Wu, B. and Kumar, A. (2007), "Extreme ultraviolet lithography: A review," *Journal of Vacuum Science and Technology B*, 25, 1743–1761.

Xia, F., Mueller, T., Lin, Y.-M., Valdes-Garcia, A., and Avouris, P. (2009), "Ultrafast graphene photodetector," *Nature Nanotechnology*, 4, 839 – 843.

Yao, Y., Kats, M. A., Genevet, P., Yu, N., Song, Y., Kong, J., and Capasso, F. (2013), "Broad Electrical Tuning of Graphene-Loaded Plasmonic Antennas," *Nano Letters*, 13, 1257–1264, PMID: 23441688.

Zhu, J., Liu, Q. H., and Lin, T. (2013a), "Manipulating light absorption of graphene using plasmonic nanoparticles," *Nanoscale*, 5, 7785–7789.

Zhu, W., Rukhlenko, I. D., and Premaratne, M. (2013b), "Graphene metamaterial for optical reflection modulation," *Applied Physics Letters*, 102, –.

Biography

Jun Niu was born in Chengdu, Sichuan, China in 1990. He received the B.S. degree from the *Yingcai* Experimental School, the honored program of University of Electronic Science and Technology of China in 2012, and the M.S. degree from Department of Electrical and Computer Engineering of Duke University in 2016, as a joint program of the Ph.D. study. Jun Niu is currently working toward his Ph.D. degree in electrical and computer engineering. He is also acknowledged with the Photonics and Nano Science Certificates by the Duke University.

Since 2012, he has been a Research Assistant with the Department of Electrical and Computer Engineering at Duke University, Durham, NC, USA. His current research interests include electromagnetic theory, fast algorithms in computational electromagnetics, especially its application in nano optics, and optical imaging.

Selected Journal Publications

1. Jun Niu, Yi Ren, Qing Huo Liu, "Spectral Element Boundary Integral Method with Periodic Layered Medium Dyadic Green's Function for Multiscale Nano-Optical Scattering Analysis", *In Submission.*

2. Jun Niu, Ma Luo, Qing Huo Liu, "Enhancement of Graphenes Third Harmonic Generation with Localized Surface Plasmon Resonance under Optical/ Electro-Optic Kerr Effect", *Journal of the Optical Society of America B*, Vol. 33, No. 4, 615-621, 2016.

3. Jun Niu, Ma Luo, Jinfeng Zhu, Qing Huo Liu, "Light Absorption Manipulation of Graphene: Simulation by Boundary Integral Spectral Element Method", *Optics Express*, Vol. 23, No. 4, Feb. 2015.

4. Jun Niu, Ma Luo, Yuan Fang, Qing Huo Liu, "Boundary Integral Spectral Element Method Analyses of Extreme Ultraviolet Multilayer Defects", *Journal of the Optical Society of America A*, Vol. 31, No. 9, Sep. 2014.

5. Yi Ren, Y. Chen, Q. Zhan, Jun Niu, Qing Huo Liu, "A Higher-Order Hybrid SIE/FEM/SEM Method for the Flexible Electromagnetic Simulation in Layered Medium", *IEEE Transactions on Geoscience and Remote Sensing*, Vol.55, No.5, 2563 - 2574, 2017

6. Yi Ren, Weifeng Huang, Jun Niu, Qing Huo Liu, "A Hybrid Solver Based on Domain Decomposition Method for the Composite Scattering in Layered Medium", *IEEE Antennas and Wireless Propagation Letters*, Vol.16, 420 - 423, 2016

7. Yi Ren, Weifeng Huang, Jun Niu, Qing Huo Liu, "Nearly Hypersingular Integrals by Double-Arctan Transformation in Higher Order Geometry Modeling", *IEEE Transactions on Antennas and Propagation*, Vol.64, No.10, 4493 - 4498, 2016

Selected Conference Publications

1. Jun Niu, Yi Ren, Qing H. Liu, "A Hybrid Perfectly Matched Layer - Spectral Element Boundary Integral Method for Periodic/ Non-Periodic Analyses", *2017 IEEE International Symposium on Antennas and Propagation and USNC-URSI Radio Science Meeting*

2. Jun Niu, Yi Ren, Qing H. Liu, "Singularity Extraction for Periodic Layered Medium Greens Function under Matrix-Friendly Formulation", *2017 IEEE International Symposium on Antennas and Propagation and USNC-URSI Radio Science Meeting*

3. Jun Niu, Yi Ren, Qing H. Liu, "Boundary Integral Spectral Element Method with Periodic Layered Medium Greens Function under Matrix-Friendly Formulation", *2017 IEEE International Symposium on Antennas and Propagation and USNC-URSI Radio Science Meeting*

4. Yi Ren, Shi-Wei Zhao, Jing-He Li, Jun Niu, Hong-Sheng Zhang, Wen Huang, "Higher Order Electromagnetic Modeling in Current and Charge Integral Equation Method", *2017 IEEE International Symposium on Antennas and Propagation and USNC-URSI Radio Science Meeting*

5. Jun Niu, Yi Ren, Ma Luo, Qing H. Liu, "Self-Consistent Analyses of Third Harmonic Generation Enhancement with Compact Plasmonics", *2016 IEEE International Symposium on Antennas and Propagation and USNC-URSI Radio Science Meeting*

6. Jun Niu, Ma Luo, Qing H. Liu, "Analyzes of Optical/ Electro-Optic Kerr Effects in Third Harmonic Compact Plasmonics", *2016 IEEE International Symposium on Antennas and Propagation and USNC-URSI Radio Science Meeting*

7. Yi Ren, Jun Niu, Weifeng Huang, Qing H. Liu, "Hybrid Electromagnetic Modeling in Layered Medium", *2016 IEEE International Symposium on Antennas and Propagation and USNC-URSI Radio Science Meeting*

8. Jun Niu, Ma Luo, Qing H. Liu, "Full-Wave Third Harmonic Generation Analyses of Graphene-Based Optoelectronic Devices", *2015 IEEE International Sym-*

posium on Antennas and Propagation and USNC-URSI Radio Science Meeting.

9. Jun Niu, Ma Luo, Jinfeng Zhu, Qing H. Liu, "Enhanced Surface Plasmonic Optical Absorption Engineering of Graphene: Simulation by Boundary-Integral Spectral Element Method", *2015 IEEE International Symposium on Antennas and Propagation and USNC-URSI Radio Science Meeting.*

10. Jun Niu, Ma Luo, Qing H. Liu, "Full-Wave Nonlinear Optical Analyses of Graphene-Based Optoelectronic Devices", *2015 IEEE International Symposium on Antennas and Propagation and USNC-URSI Radio Science Meeting.*

11. Jun Niu, Ma Luo, Qing H. Liu, "Graphenes Enhanced Linear and Nonlinear Behaviors under Localized Surface Plasmon Resonances Analyses with Boundary-Integral Spectral Element Method", *2015 Progress in Electromagnetics Research Symposium.*

12. Jun Niu, Ma Luo, Qing H. Liu, "Boundary-Integral Spectral Element Method for Extreme Ultraviolet Multilayer Defects Analyses", *2014 IEEE International Symposium on Antennas and Propagation and USNC-URSI Radio Science Meeting.*